*Astronomy Reports, Vol. 47, No. 7, 2003, pp. 531–534. Translated from Astronomicheskiĭ Zhurnal, Vol. 80, No. 7, 2003, pp. 579–582.*


# Galaxies and Stars

**B. I. Fesenko**

*Pedagogical Institute, Pskov, Russia*

Received June 17, 2002; in final form, November 27, 2002

**Abstract**—The distribution of galaxies in the vicinity of stars brighter than $V = 7.25^m$ is analyzed. The number density of galaxies is slightly decreased in such regions. This result is statistically significant and cannot be explained as a direct effect of the extended photographic images of these stars. The result is apparently associated with the presence of clouds near the stars, which absorb or scatter light.


## 1. INTRODUCTION

By absorbing and scattering light, the interstellar medium of the Galaxy influences our visibility of distant galaxies much more strongly than that of stars. Underestimation of this effect could lead to incorrect conclusions about the properties of the large-scale distribution of matter in the Universe. Images of galaxies usually have surface brightnesses that do not greatly exceed the background brightness (especially at their edges). Therefore, interstellar dust diminishes our visibility of galaxies in two ways: (1) absorbing the light from the galaxies, which also lowers the contrast of the galaxy image relative to the background, and (2) enhancing the background brightness due to the effect of scattered starlight (even if this is small). Even far from the plane of the Milky Way, the role of this intragalactic factor remains not only appreciable but possibly dominant in studies of the apparent distribution of galaxies.

One argument that we can neglect the intragalactic factor at high Galactic latitudes is the coincidence of the spatial correlation function of galaxies with the expected (and observed) correlation function for galaxies distributed on a sphere. However, we must not forget that distance estimates for large samples of galaxies remain crude and uncertain, preventing us from unqualified acceptance of results obtained for the *spatial* case. In addition, it has not been demonstrated that the form of the *surface* correlation function cannot be explained purely by the properties of the intragalactic factor.

In our previous studies, we have investigated the role of the intragalactic factor at high latitudes using various methods: analyzing correlations between the surface density of the number of galaxies and the surface density of Galactic neutral hydrogen in a given direction, calculating correlation functions for the observed numbers of galaxies assuming that a determining role is played by the interstellar medium, analyzing data for deep samples of galaxies in regions of the sky near the poles, using IR sky surveys (the intragalactic factor is manifest much more weakly in the infrared than in the visible), etc. Our most recent study [1] presents a list of our main publications in this area.

Below, we will consider the relationship between the distributions of stars and galaxies in the sky. As far as we are aware, this is the first time such an analysis has been carried out. The angular diameters of stellar images are very small, and the superposition of stellar images on those of distant galaxies should be negligible if we consider source counts in areas about one square degree in size. This will not be true only for counts carried out near the brightest (and relatively scarce) stars in the Palomar Sky Survey maps, where the images of such stars are strongly overexposed. However, if there is diffuse material near some types of stars, this may scatter the light radiated by these stars (enhancing the background brightness) and/or absorb the light from distant galaxies, so that we expect in this case a *decrease* in the (mean) number of such galaxies observed in the vicinity of these stars. The opposite case is also possible, when the observed number of galaxies *grows* due to the fact that the short-wavelength radiation from the star sweeps out the surrounding gas and dust (this region becomes more transparent).

## 2. MATERIAL AND METHOD USED

We have used galaxy counts carried out at the Lick Observatory [2] for fields $6^\circ \times 6^\circ$ in size whose centers are no further than $32^\circ$ from the northern Galactic pole. The interstellar absorption of light is usually not taken into account in such fields, which is precisely why we have selected them for our study. In each field, which has the form of a rectangle whose sides are

1063-7729/03/4707-0531$24.00 

oriented approximately along the directions of declination and right ascension, we excluded a western strip consisting of six $1^\circ \times 1^\circ$ area elements; since these strips overlapped with the eastern edge of the neighboring area in right ascension, this did not lead to gaps in the counts.

Each of these fields corresponded to an individual photographic plate, which covered the field entirely. The transition to another field corresponds to a transition to another plate, with its own observing conditions, reduction, and galaxy-count determination. In addition, the data on the distribution of galaxies are not completely uniform even within a single plate, and there is a reduction in the number density of galaxies by 10–20% from the center to the edges of the plate. This effect is especially appreciable in angular area elements and also near the western edge of each plate (see above). In spite of the fact that both types of inhomogeneity in the data can be accounted for using statistical methods, there always remains some doubt about the trustworthiness of conclusions concerning the properties of the apparent distribution of galaxies on characteristic scales exceeding 6° derived using such material (it is interesting that the impressive pattern visible in the distribution of the reduced number of galaxies that seems to confirm the cell-like structure of the Universe corresponds to this case). The method used below to analyze the galaxy counts is insensitive to both types of inhomogeneity in the data.

The stars around which we analyzed the distribution of galaxies were selected from the catalog [3]. The limiting brightness was taken to be $V = 7.25^m$.

All the observational material for the galaxy counts and parameters of the stars ($V$ magnitudes, $B-V$ color indices, and equatorial coordinates) were read into a computer for the analysis, converting the coordinates from the catalog [3] to epoch 1950.0 so that they would correspond to the coordinate grid of [2]. We wrote a program enabling us to determine for each star the number of galaxies in a $1^\circ \times 1^\circ$ area around the star and calculate the ratio of this number to the mean number of galaxies in similar areas over the entire field. We assumed that, in the absence of any influence of the star or its immediate vicinity on the number of observed galaxies, this ratio (which we denote $Z$) should be equal to unity within the random errors. We reduced the errors in the numbers of galaxies by introducing a correction for the variation in the number density of galaxies from the center to the edges of each field. We derived this correction statistically by summing the numbers of galaxies in different fields but in the same area elements relative to the plate center. Similar corrections were applied during the source-count analysis in [2], but we have derived them again here using only those fields in which our stars are located.

As a check, similar calculations were carried out for areas selected randomly and not identified earlier with stars (i.e., any of the bright stars located in these fields were there only by chance), with the number of such areas being equal to the number of stars in our sample in the same field.

A computer version of that part of the catalog [3] with right ascensions higher than $11^h56^m$ (more precisely, for HD numbers beginning with 103613) was created, excluding stars with $V > 7.25^m$. If coincident coordinates for different components of the same multiple star system were presented in the catalog, we retained only the coordinates of the system. We had data on numbers of galaxies in 175 fields in a circular region of sky with its center at the northern Galactic pole and a radius of 32°, 161 of which fell in the region covered by the computer version of the star catalog. These 161 fields included 4830 area elements containing 279 407 galaxies, with the mean number of galaxies in an area element being 57.85. Recall that the fields often overlapped, so that the number of area elements was slightly lower than indicated above. The number of stars remaining for the study (see above) was 607. Due to the partial overlap of the fields, some stars simultaneously falling in different fields were analyzed more than once. Therefore, galaxies were counted in 771 area elements, each of them containing a star.

The resulting mean value of $Z$ for this entire sample is

$$\langle Z \rangle = 0.962 \pm 0.0123.$$

Due to the very large number of random fluctuations in the numbers of galaxies in the area elements, some of these elements had very large values of $Z$, appreciably higher than the standard deviation $\langle Z \rangle$. Excluding the two area elements (of the total of 771) for which $Z > 3$ yields

$$\langle Z \rangle = 0.959 \pm 0.0117, \quad (1)$$

while the counts for 100 realizations of 769 *randomly* selected area elements yielded a value of $Y$, analogous to $Z$ (excluding $Y > 3$), of

$$\langle Y \rangle = 1.0029 \pm 0.0013. \quad (2)$$

The expected theoretical value $\langle Y \rangle \neq 1$, since both the numerator and denominator in the fraction $k/l$, where $k$ is the number of galaxies in the given area element and $l$ is the mean arithmetic number of galaxies in the remaining 29 areas of the given field, are subject to fairly strong random fluctuations. As a result, systematic shifts appear during the averaging of

such fractions due to the fluctuations in the denominator. Calculations for this case indicate that this shift should increase the value of $\langle Y \rangle$ by approximately 0.0021. There will be an analogous shift in the value of $\langle Z \rangle$.

Comparing (1) and (2), we conclude that the presence of stars brighter than $7.25^m$ in an area element **on average** decreases the number of observed galaxies by 4%. The standard deviation is about 1%. The fact that the presence of such a star affects the observed number of galaxies in the surrounding area (on the celestial sphere) can now be considered to be firmly established.

We carried out another test of the reality of this effect by comparing the distributions of $Z$ and $Y$ values, with the latter estimated using the results of 100 realizations of the randomly selected areas. The numbers of values with $Z < 1$ and $Z > 1$ were 471 and 300, while the corresponding numbers of $Y$ values in these $Z$ intervals were 433.48 and 337.52. According to the $\chi^2$ criterion, the probability of a discrepancy this large or larger is only 0.0065.

## 3. DISCUSSION

In view of the smallness of the detected effect, the question arises of whether it is deserving of further analysis and discussion in connection with the *apparent distribution of galaxies*. (There is no doubt that the effect is important as an indicator of the properties of the near vicinities of the studied stars.) To answer this question, we must consider at least three circumstances.

*First,* we have estimated the total effect only of the stars in **our** sample. Let us suppose that only 10% of these stars are responsible for the 4% decrease in the mean density of the field galaxies, while the remaining stars do not influence this density. We will refer to the first type of stars as "active" and the remaining stars as "passive." Denoting $x$ to be the $Z$ value for the active stars and adopting $Z = 1$ for the passive stars, we obtain the following equation for $x$:

$$0.1x + 0.9 = 0.96$$

[see (1)], which yields $x = 0.6$. If the overall mean number of galaxies in an area element is 58, the mean number of galaxies in the corresponding area around an active star is about 35; i.e., there are 23 fewer galaxies than the average number. At the same time, the standard deviation of the number of galaxies (for an average number per area of 58) is 14 (if we exclude large-scale fluctuations at distances exceeding 2°). This example shows how the four-percent mean decrease in the number density of galaxies could be manifest.

*Second,* active stars could also be present among stars weaker than $7.5^m$, which we have excluded from our consideration. The larger numbers of such stars could compensate for some decrease in their "activity" compared to brighter stars. As we show below, the degree of "activity" in our sample depends only weakly on the brightness of the star. Therefore, we suppose that the mean "activity" of stars does not undergo a sharp drop in the transition to the more numerous weaker stars. The fact that there are about eight area elements for each star in our sample does not necessarily imply that the effect of active stars should be insignificant, since there could be active stars among the weaker objects located in areas that do not contain a star brighter than $7.25^m$. In addition, more than one weak active star could end up in the same area element by chance.

*Third*, as already noted, the "activity" of a star could be manifest not as a decrease in the number density of galaxies, but instead as an increase in this density. When we estimate the *average* effect of the "activity," these opposing actions will weaken each other, decreasing the net deviation of $\langle Z \rangle$ from unity. We do not yet know how to distinguish these two effects statistically with reasonable certainty.

It is therefore of interest to determine the origin of the decrease in the number density of galaxies around the bright stars.

*Are the diameter and density of the stellar image, which depend on the apparent magnitude of the star, important*? The values of $\langle Z \rangle$ for $V < 5^m$ and $V \geq 5^m$ were $0.973 \pm 0.032$ and $0.957 \pm 0.012$. Thus, there is little evidence for a dependence on the brightness of the star in the observational material considered. In particular, when $V \geq 7.0$, we obtain $\langle Z \rangle = 0.950 \pm 0.026$, in agreement with the general estimate of (1).

*Is the "activity" of the star reflected in its $B{-}V$ color index*? The values of $\langle Z \rangle$ for stars with $B{-}V < 0.2$ and $B{-}V \geq 1.0$ are $0.921 \pm 0.026$ and $0.977 \pm 0.021$. The difference in these values of $\langle Z \rangle$ is $0.056 \pm 0.033$, which is not statistically different from zero.

*Can we trace the "activity" of a star outside its own area element (one square degree)*? For the 4492 area elements abutting onto the central area elements (each of which contains a star in our sample), we obtained the estimate

$$\langle Z \rangle = 0.993 \pm 0.0050, \quad (3)$$

while the analogous calculation for areas surrounding 100 realizations of randomly selected area elements (see above) yielded the value

$$\langle Y \rangle = 1.0018 \pm 0.00050. \quad (4)$$

A comparison of (3) and (4) suggests a small deviation of the mean value of $Z$ from unity in the same direction as in (1) and (2), but this result is not statistically significant.

## 4. CONCLUSIONS

The analysis of counts of galaxies in the vicinity of stars represents one method for studying the dark or light-scattering (low surface brightness) material associated with these stars. Having, as a rule, very low surface brightnesses at their peripheries, galaxies are much more sensitive to fluctuations in the observing conditions than are distant background stars surrounding the star being studied. This was already evident from the results of [2], which analyzed the Galactic-latitude dependence of the number density of weak galaxies associated with a dust layer in the Galactic plane. However, the use of fluctuations in the surface number density of galaxies as an indicator of the presence (or absence) of a dusty medium in the vicinities of stars comes up against serious difficulties. Virtually all galaxies are collected into groups or clusters, making the galactic background surrounding foreground stars very inhomogeneous. As a result, the expected small effects associated with the foreground stars in this area of the sky are overwhelmed by fluctuations in the density of the background galaxies.

Therefore, the approach of counting galaxies surrounding stars can currently be applied only statistically, averaging results for a fairly large sample of stars that are bright (and comparatively nearby the observer). In this case, the effect of faint (and, on average, distant) stars is excluded, since the angular dimensions of their near vicinities are too small.

The 4% decrease in the density of the galactic background surrounding stars with $V \leq 7.25^m$ we have found here must be verified using other observational material. If this result is confirmed (at least qualitatively), the need to carry out counts of much weaker galaxies around high-latitude stars will become clear. The analysis of counts of numerous weak galaxies will enable the suppression of random fluctuations, which represent the main factor hindering studies of individual objects using this approach.

## REFERENCES

1. B. I. Fesenko, Astrofizika **44**, 509 (2001).
2. C. D. Shane and C. A. Wirtanen, Publ. Lick Observ. **22**, 1 (1967).
3. *Catalogue of WBVR Magnitudes of Northern Bright Stars* [in Russian], Ed. by V. G. Kornilov (Izd. Mos. Gos. Univ., Moscow, 1991), Tr. Gos. Astron. Inst. Shternberga **63**.

*Translated by D. Gabuzda*

*Astronomy Reports, Vol. 47, No. 7, 2003, pp. 535–539. Translated from Astronomicheskiĭ Zhurnal, Vol. 80, No. 7, 2003, pp. 583–588.*


# Models of the Dust Envelope of the Unique Object FG Sagittae

**M. B. Bogdanov[1] and O. G. Taranova[2]**

[1] *Chernyshevsky University, ul. Universitetskaya 42, Saratov, 410601 Russia*

[2] *Sternberg Astronomical Institute, Universitetskiĭ pr. 13, Moscow, 119992 Russia*

Received September 20, 2002; in final form, January 10, 2003

**Abstract**—We use $JHKLM$ photometric data obtained in 1998–2001 to model the dust envelope of the unique object FG Sge, which formed around the star after several consecutive cycles of dust condensation beginning in Autumn 1992. Models with a spherically symmetric, extended envelope consisting of a mixture of spherical particles of amorphous carbon and silicon carbide with an MRN size distribution were fitted to match the mean observed spectral energy distributions of FG Sge during brightness maximum and minimum after 1998 for two values of the luminosity and effective temperature of the central star. The stellar-wind parameters and mass-loss rate have been estimated in each case. The observational data for the brightness maximum and minimum cannot be described by models with a fixed luminosity or fixed distance to the star. This is a consequence of the object's unusual behavior, with synchronous flux decreases in all the observed bands. The inability of the model to adequately describe the minimum-brightness state is probably associated with the abrupt disruption of the spherical symmetry of the envelope due to the formation of a small, dense dust cloud in the line of sight. © *2003 MAIK "Nauka/Interperiodica"*.

## 1. INTRODUCTION

The object FG Sge has long attracted the attention of astronomers due to the unusual variations of its spectrophotometric characteristics. Over almost a hundred years, the brightness of the star increased slowly from $m_{pg} = 13\overset{m}{.}6$ in 1894 to $B = 9\overset{m}{.}6$ in 1965, and its spectral class changed from B5Ia in 1955 to A5Ia in 1967 and G2 Ia in the mid-1970s. The bolometric luminosity remained virtually unchanged as the visual brightness increased, tracing out a horizontal track in the spectrum–luminosity diagram. Since the mid-1970s, the brightness of the star has remained approximately constant, with the spectral class being approximately F6.

Simultaneous appreciable changes of the chemical composition of the atmosphere of FG Sge have been observed. In the 1960s, this composition was approximately solar, but lines of rare-earth elements suddenly appeared at the beginning of the 1970s and subsequently grew in strength. According to González *et al.* [1], one probable explanation of these phenomena is the onset of helium burning in a shell source, which coincided with the increase of the star's brightness about 100 years ago. The stellar photosphere expanded, accompanied in the 1970s by a dredge-up of $s$-process elements. It is believed that FG Sge is the central star of the old planetary nebula He1-5, which recently passed through a stage of activity in which it had a considerably higher temperature. At present, this activity is slowly decreasing.

We have been carrying out photometric monitoring of FG Sge in the infrared at the Crimean Observatory of the Sternberg Astronomical Institute since 1985 [2]. These observations show that, until Autumn 1992, the brightness of the star in the near infrared (1.25–3.5 $\mu$m) varied within $0\overset{m}{.}3$, with a cycle of $100–120^d$. In 1985–1989, the spectral energy distribution (SED) of FG Sge at 0.36–2.2 $\mu$m corresponded to that of an F8–G1 supergiant. The estimated mean IR magnitudes in this period were $J = 7\overset{m}{.}10 \pm 0\overset{m}{.}03$, $K = 6\overset{m}{.}56 \pm 0\overset{m}{.}02$, and $L = 6\overset{m}{.}31 \pm 0\overset{m}{.}02$. In addition, our monitoring from 1985 to 1989 enabled us to detect the presence of a relatively hot, optically thin circumstellar dust envelope [2], whose existence was confirmed in [3, 4].

In August 1992, the behavior of the brightness variations of FG Sge underwent dramatic changes, which had never been observed for this star before. The brightness in the visual and near-infrared (1.25–1.65 $\mu$m) began to decrease rapidly. Over several dozen days, the $V$ brightness dropped by $\sim 5^m$, and the $J$ brightness fell by approximately $2\overset{m}{.}5$. At the same time, the flux at $\lambda > 2.2$ $\mu$m began to grow, and the $L$ brightness increased by more than $2^m$ in the second half of September 1992 [5]. Due to the character of these brightness and color variations of FG Sge over a broad spectral range in September 1992, it was possible to unambiguously relate the observed effects with the formation of a dust envelope around the star. Observations of FG Sge obtained after September 1992 have been analyzed in many

1063-7729/03/4707-0535$24.00 

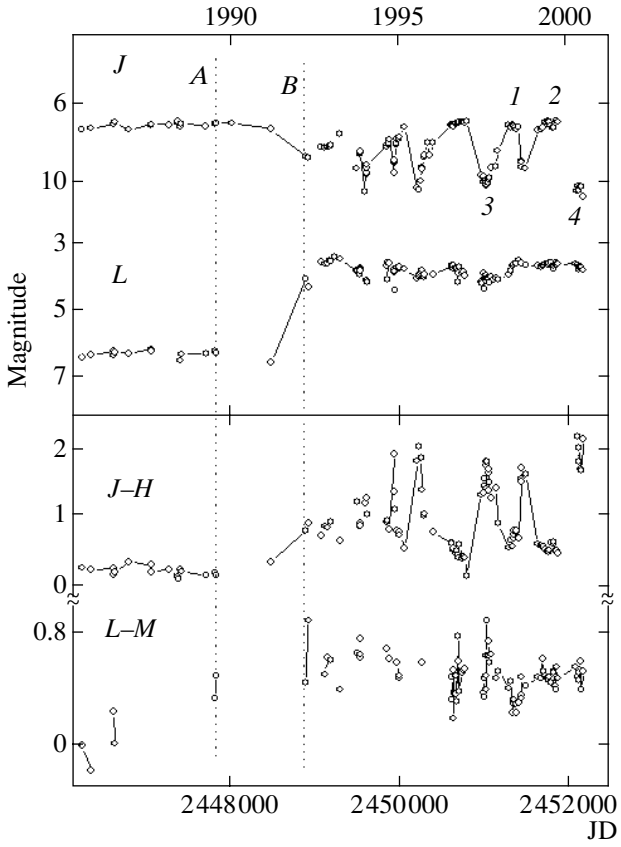


**Fig. 1.** Variations of the $J$ and $K$ brightnesses and the $J-H$ and $L-M$ color indices of FG Sge from 1985 to 2001.

papers; a bibliography can be found in González *et al.* [1] and Arkhipova *et al.* [5].

Our infrared photometry of FG Sge in 1993–1997 has been analyzed by Tatarnikov *et al.* [6] and Tatarnikov and Yudin [7]. Taranova and Shenavrin [8] analyzed $JHKLM$ photometric observations of the star obtained in 1985–2001.

The aim of the current paper is to calculate spherically symmetric, extended dust-envelope models for FG Sge on the basis of our $JHKLM$ photometry carried out in 1998–2001, supplemented by observations in the visual.

## 2. OBSERVATIONAL DATA

Figure 1 shows the variations of the brightness in the $J$, $L$ bands and of the $J-H$ and $L-M$ color indices of FG Sge from 1985 to 2001. The vertical lines $A$ and $B$ mark the dates of observations in Autumn 1989 (no appreciable dust envelope) and Autumn 1992 (in the middle of which a dust envelope formed around the star). The effect of the formation of the envelope is clearly visible in Fig. 1. At 1.25 $\mu$m ($J$ band), where the radiation from even optically thick hot dust envelopes is weak and the dust envelope is manifest almost exclusively via absorption, the stellar flux decreased (relative to 1989) by almost $1\overset{m}{.}5$. At 3.5 $\mu$m ($L$ band), the peak of blackbody radiation with temperatures of 800–900 K (typical of hot, circumstellar dust envelopes), the flux increased by more than $2^m$. After Autumn 1992, the 1.25-$\mu$m brightness varied quasi-periodically with an amplitude reaching $3\overset{m}{.}5$, and, at its maximum, the $J$ brightness sometimes exceeded its pre-Autumn 1992 value. At the same time, the stellar brightness at 3.5 $\mu$m reached its maximum in Autumn 1993, after which it varied within $0\overset{m}{.}5$. In 1992–2001, the $J-H$ color index varied with an amplitude of $\sim 2^m$ in phase with the $J$ brightness variations; i.e., the star became redder during the minimum $J$ brightness. The amplitude of the $L-M$ variations did not exceed $0\overset{m}{.}5$. As shown in [8], the photometric peculiarities in the light and color variations of FG Sge after August 1992 are consistent with a circumstellar dust-envelope model with dense, compact clouds of dust.

In the analysis considered here, we have used observations of FG Sge obtained in 1998–2001, near maxima and minima of the $J$ brightness. The numbers 1 and 2 in Fig. 1 label epochs of $J$ brightness maxima, while the 3 and 4 denote epochs of $J$ minima. The photometric data during these maxima and minima were averaged, and the average magnitudes are listed in Table 1 together with their standard deviations $s(m)$ and the numbers of averaged nights $N$.

## 3. CALCULATION OF DUST-ENVELOPE MODELS

Models of the dust envelope of FG Sge were first calculated by Tatarnikov *et al.* [6], using observational data obtained in 1993–1997 and assuming the envelope was made up of graphite particles. The model envelope consisted of a series of spherical layers, with the number of layers equal to the number of deep brightness minima, which are due to consecutive cycles of dust condensation. Tatarnikov *et al.* [6] adopted the effective temperature of the central star $T_{\rm eff} = 5900$ K, the luminosity $L = 3300 L_\odot$, and the distance to the star $d = 2.5$ kpc. In this model, the total $V$-band optical depths of the envelope $\tau_V$ for various dates varied in the range 1.7–4.0. To explain the blue emission observed during deep drops of the visual brightness of FG Sge, Tatarnikov and Yudin [7] invoked disruption of the spherical symmetry of the envelope. They suggested that the envelope could consist of individual, optically thick, compact clouds of dust filling about half the volume of a sphere around the central star and yielding an infrared excess.

There is little doubt that a disruption of symmetry during the ejection of a gas–dust envelope of the star

**Table 1.** Mean magnitudes of FG Sge during $J$ minima and maxima after 1998 (see Fig. 1)

| $\lambda$, $\mu$m | MIN | | | MAX | | |
|---|---|---|---|---|---|---|
| | $m$ | $s(m)$ | $N$ | $m$ | $s(m)$ | $N$ |
| 1.25 | 10.06 | 0.04 | 16 | 7.00 | 0.03 | 13 |
| 1.65 | 8.16 | 0.02 | 15 | 6.24 | 0.02 | 13 |
| 2.2 | 6.16 | 0.02 | 14 | 5.33 | 0.02 | 13 |
| 3.5 | 3.97 | 0.05 | 14 | 3.67 | 0.03 | 13 |
| 5 | 3.43 | 0.05 | 15 | 3.25 | 0.04 | 13 |

is plausible. Evidence for this is provided, e.g., by high-resolution HST maps of young planetary nebulae. However, it is clear that it is virtually impossible to take into account such a violation of symmetry when calculating the radiative transfer in the envelope. Therefore, spherically symmetric models are usually considered. The effect of inhomogeneities of a given size is more appreciable at shorter wavelengths. In particular, to transmit (or screen) all the visible radiation of the star, it is sufficient to have a gap (or dense cloud) in the envelope with a size coinciding with the angular diameter of the star. With increasing wavelength, the size of the radiating region increases and the effect of the inhomogeneities is averaged. Unfortunately, the mid-infrared flux from FG Sge was too low for firm detections by IRAS (1983) or ISO (1995–1996). Furthermore, much time has elapsed since these instruments were operating, and these observations of this rapidly varying object cannot be used with later observations. Therefore, when calculating the dust-envelope models, we decided to restrict our consideration to our $JHKLM$ photometric data, supplemented with observations in the visual.

Since the first deep brightness minimum, the star has experienced several cycles of dust-envelope ejection. Taking into account the dispersion of the dust-particle velocities due to the range of their sizes, which leads to smearing of the areas of enhanced density, it seems reasonable to suppose that the density distribution became more uniform during the elapsed time, in accordance with the continuity condition. Proceeding from these considerations, we adopted an inverse square law for the radial dust-density variation in the envelope.

We assumed that the envelope of FG Sge contains a mixture of two kinds of particles, consisting of amorphous carbon and silicon carbide. We took the relative abundances of these particles to be 0.95 and 0.05, respectively, close to the average values for the dust envelopes of carbon stars [9]. The data on the optical constants of $\alpha$-SiC were taken from [10], and for amorphous carbon from [11].

**Table 2.** Parameters of model dust envelopes and stellar-wind characteristics for the states of minimum and maximum $J$ brightness of FG Sge

| Parameter | Version 1 | | Version 2 | |
|---|---|---|---|---|
| | Max | Min | Max | Min |
| $L$, $L_\odot$ | 3300 | 3300 | 6300 | 6300 |
| $T_{\text{eff}}$, K | 5900 | 5900 | 5800 | 5800 |
| $T_1$, K | 1100 | 1100 | 1300 | 800 |
| $r_1$, $10^{14}$ cm | 1.79 | 1.98 | 1.65 | 6.24 |
| $\tau_V$ | 0.95 | 6.40 | 2.35 | 6.25 |
| $d$, kpc | 2.1 | 3.5 | 3.1 | 3.1 |
| $\dot{M}$, $10^{-6}M_\odot$/year | 1.3 | 3.9 | 2.9 | 9.1 |
| $V_e$, km/s | 21.1 | 13.0 | 26.4 | 9.5 |
| $M_s$, $M_\odot$ | 2.5 | 2.1 | 5.0 | 3.8 |

We assumed that the dust envelope has a sharp inner boundary at distance $r_1$ from the center of the star, that the dust density decreases in proportion to the inverse square of the distance from the star out to the outer boundary of the envelope at $r_2 = 1000r_1$, and that the particle size distribution $n(a)$ is described by the model of Mathis, Rumpl, and Nordsieck (MRN) [12]: $n(a) \propto a^{-q}$ for spherical particles with radii $a_{\min} \leq a \leq a_{\max}$, with $q = 3.5$, $a_{\min} = 0.005$ $\mu$m, and $a_{\max} = 0.25$ $\mu$m.

We calculated two versions of spherically symmetric dust-envelope models for FG Sge for the states of minimum and maximum $J$ brightness after 1998 (Fig. 1 and Table 1). Both assumed a Planck SED for the central source, with

(1) effective temperature $T_{\text{eff}} = 5900$ K and luminosity $L = 3300L_\odot$ [6];

(2) effective temperature $T_{\text{eff}} = 5800$ K and luminosity $L = 6300L_\odot$.

The second set of values and the estimated distance $d = 3.1$ kpc, were used in [8] when interpreting photometric data of FG Sge for 1985–2001.

We solved for the radiative transfer in the dust envelope for both model versions using the DUSTY code (version 2.0) for a grid of 30 points in radius and 99 wavelengths from 0.01 $\mu$m to 3.6 cm. The algorithm applied in this code is described in [13, 14]. The input parameters for the models were the dust temperature at the inner boundary $T_1$ and the optical depth of the envelope at 0.55 $\mu$m, $\tau_V$. After calculating the model SED for the first version, we found the distance $d$ providing the minimum residuals

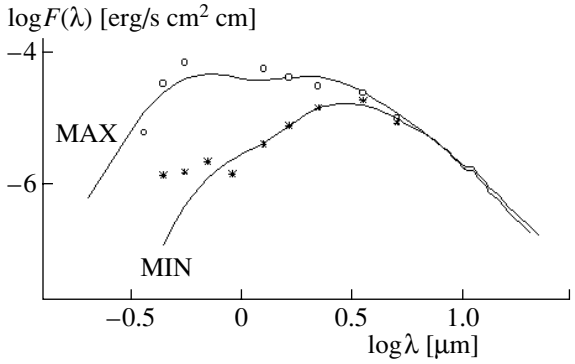


**Fig. 2.** Logarithm of the observed flux $F(\lambda)$ [erg/s cm$^2$ cm] of FG Sge in the states of maximum (circles) and minimum (asterisks) $J$ brightness as a function of the logarithm of the wavelength $\lambda$ [$\mu$m]. The solid curves show distributions for the first version of the models (see text), whose parameters are listed in Table 2.

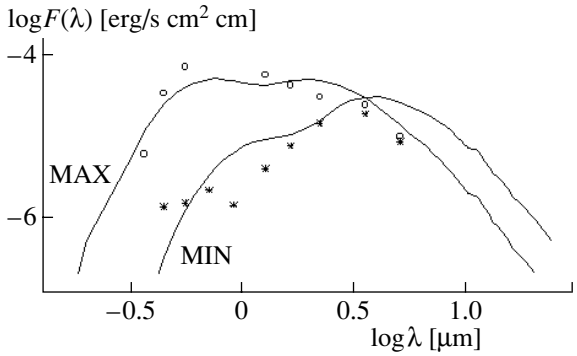


**Fig. 3.** Same as Fig. 2 for the second version of the models.

between the observed and model fluxes. In the second version, the distance was fixed at 3.1 kpc.

The obtained best-fit values of the parameters for the first model version are listed in the second and third columns of Table 2. Figure 2 presents the SEDs for the calculated models. The curves in the figure plot the logarithm of the flux $F(\lambda)$ (in erg/s cm$^2$ cm) as a function of the logarithm of the wavelength $\lambda$ (in $\mu$m), while the circles and asterisks show the observed fluxes, corrected for interstellar extinction, for the states of maximum and minimum brightness. The feature of the SED near $\log\lambda = 1.0$ is due to the presence of silicon carbide. As we can see from the figure, the models describe the observations satisfactorily.

The best-fit values of the model parameters for the second version providing the minimum residual between the observed and calculated fluxes are given in the fourth and fifth columns of Table 2; the corresponding SEDs are compared with the observational data in Fig. 3. The notation in this figure is the same as in Fig. 2. We can see from Fig. 3 that the model describes the observations for the state of maximum brightness fairly well over a broad range of wavelength, though there are also discrepancies, especially for the $U$ and $V$ fluxes. These deviations considerably exceed the probable errors of the observations and should be interpreted as reflecting a disruption of the model assumptions. This likely applies first and foremost to the assumption of spherical symmetry of the envelope.

The representation of the observations for the state of minimum brightness by the model dust envelope with luminosity $L = 6300L_\odot$ and distance $d = 3.1$ kpc is not satisfactory. As an alternative, we rejected the assumption that the dust density decreases in proportion to the inverse square of the distance and considered a model envelope with a uniform dust layer with thickness $0.1r_1$. It is possible that this dust distribution is closer to the real distribution if the dust is formed rapidly. However, this model, likewise, could not reproduce the observed fluxes at minimum brightness satisfactorily. This is a consequence of the quite unusual behavior of the star, with the fluxes in all bands decreasing simultaneously. In spherically symmetric models of the dust envelope adopting a fixed distance, this behavior can be reproduced only if we assume an abrupt decrease in the luminosity of the star.

Thus, the observed SEDs of FG Sge for the states of maximum and minimum brightness after 1998 cannot be described by spherically symmetric dust-envelope models with any fixed luminosity and distance. To bring the model into agreement with the observations, we must either vary the distance to the star keeping the luminosity fixed (Table 2) or, keeping the distance fixed, change the star's luminosity by a factor of a few. In our view, the only reasonable explanation for the models' inadequacy in describing the state of minimum brightness is a strong disruption of the spherical symmetry of the envelope, most probably due to the formation of a small, dense dust cloud in the line of sight.

## 4. STELLAR WIND PARAMETERS

To estimate the parameters of the stellar wind of FG Sge arising due to the radiation pressure on the dust and the subsequent transfer of momentum to the gaseous medium, we used the gas-dynamical mode of the DUSTY code with the derived optical depths of the envelope. In this mode, the code implements a self-consistent procedure to solve for the radiative transfer and motion of the dust in the envelope [15]. We adopted a dust-particle density of $\rho_d = 3$ g/cm$^3$ and a gas-to-dust mass ratio in the envelope of $r_{gd} =$

200. Using these values, the DUSTY code calculates the total mass-loss rate $\dot{M}$, the gas expansion velocity at the outer boundary of the envelope $V_e$, and an upper limit on the mass of the central source of radiation $M_s$. The derived characteristics of the stellar wind for the two model versions are listed in the bottom rows of Table 2. If necessary, they can be readily recalculated for other values of $\rho_d$ and $r_{gd}$, using the fact that $\dot{M} \propto (\rho_d r_{gd})^{1/2}$, $V_e \propto (\rho_d r_{gd})^{1/2}$, and $M_s \propto (\rho_d r_{gd})^{-1}$ [15].

The calculated parameters of the stellar wind for specified properties of the dust particles and their density variation are determined by the optical depth of the dust envelope, the temperature of the dust at its inner boundary, and the luminosity of the central star. The wind characteristics for each of the models considered reflect the model parameters. However, their correspondence to the real values is determined entirely by the extent to which the model of the studied object is appropriate. For instance, it is clear that the obtained estimates of $\dot{M}$, $V_e$, and $M_s$ for the brightness minimum in the second model version (last column of Table 2) are purely formal and that they do not correspond to the real values.

## 5. CONCLUSIONS

Our model dust-envelope calculations for FG Sge for the effective temperatures and luminosities of the central star considered earlier ($T_{\rm eff} = 5900$ K, $L = 3300 L_\odot$ [6] and $T_{\rm eff} = 5800$ K, $L = 6300 L_\odot$ [8]) do not enable us to discriminate between the two model versions. In both cases, the observed SED for the state of maximum brightness can be described more or less satisfactorily by models with widely differing sets of parameters and with different distances (Table 2). Accordingly, this leads to differing stellar-wind parameters.

Reproduction of the observational data for the state of minimum brightness using models with a spherically symmetric dust envelope faces large difficulties. In the first model version, keeping the stellar luminosity fixed requires an increase of the distance of the star from 2.1 to 3.5 kpc. The former value is far outside the range of estimated distances to FG Sge, 2.5–4.1 kpc, obtained earlier in [8, 16, 17], and the latter value is within this range. Nevertheless, this difference in the distances is more likely a consequence of inadequacy of the model and violation of the assumptions used in the calculations. In the second model version, with a fixed luminosity and distance, it is completely impossible to achieve a satisfactory agreement with the observations for the state of minimum brightness of the star. This is a consequence of the unusual behavior of the object, displaying simultaneous decreases of the observed fluxes in all bands. The inadequacy of the model may be due to a strong disruption of the spherical symmetry of the envelope associated with the formation of a small, dense dust cloud in the line of sight.

## ACKNOWLEDGMENTS

The authors are grateful to the astrophysics group of the University of Kentucky (Željko Ivezić, Maia Nenkova, Moshe Elitzur) for the opportunity to use the DUSTY code to solve the equation of radiative transfer. This work was partially supported by the Ministry of Industry, Science, and Technology of the Russian Federation (Federal Program in Astronomy), the Ministry of Education of the Russian Federation (grants E00-11.0-31 and UR.02.01.003), and the Russian Foundation for Basic Research (project code 00-02-16232).

## REFERENCES

1. G. González, D. L. Lambert, G. Wallerstein, *et al.*, Astrophys. J., Suppl. Ser. **114**, 133 (1998).
2. V. P. Arkhipova and O. G. Taranova, Pis'ma Astron. Zh. **16**, 808 (1990) [Sov. Astron. Lett. **16**, 347 (1990)].
3. B. Montesinos, A. Cassatella, R. Gonzalez-Reistra, *et al.*, Astrophys. J. **363**, 245 (1990).
4. C. E. Woodward, G. F. Lawrence, R. D. Gehrz, *et al.*, Astrophys. J. **408**, L37 (1993).
5. V. P. Arkhipova, V. F. Esipov, G. V. Sokol, and S. Yu. Shugarov, Pis'ma Astron. Zh. **25**, 849 (1999) [Astron. Lett. **25**, 739 (1999)].
6. A. M. Tatarnikov, V. I. Shenavrin, and B. F. Yudin, Astron. Zh. **75**, 428 (1998) [Astron. Rep. **42**, 377 (1998)].
7. A. M. Tatarnikov and B. F. Yudin, Pis'ma Astron. Zh. **24**, 359 (1998) [Astron. Lett. **24**, 303 (1998)].
8. O. G. Taranova and V. I. Shenavrin, Astron. Zh. (2002, in press).
9. M. A. T. Groenewegen, P. A. Whitelock, C. H. Smith, and F. Kerschbaum, Mon. Not. R. Astron. Soc. **293**, 18 (1988).
10. B. Pegourie, Astron. Astrophys. **194**, 335 (1988).
11. V. G. Zubko, V. Mennella, L. Colangeli, and E. Bussoletti, Mon. Not. R. Astron. Soc. **282**, 1321 (1996).
12. J. S. Mathis, W. Rumpl, and K. H. Nordsieck, Astrophys. J. **217**, 425 (1977).
13. Z. Ivezic and M. Elitzur, Mon. Not. R. Astron. Soc. **287**, 799 (1997).
14. Z. Ivezic and M. Elitzur, Mon. Not. R. Astron. Soc. **303**, 864 (1999).
15. Z. Ivezic and M. Elitzur, Astrophys. J. **445**, 415 (1995).
16. G. H. Herbig and A. A. Boyarchuk, Astrophys. J. **153**, 397 (1968).
17. A. M. Van Genderen and A. Gautscky, Astron. Astrophys. **294**, 453 (1998).

*Translated by G. Rudnitskiĭ*

*Astronomy Reports, Vol. 47, No. 7, 2003, pp. 540–550. Translated from Astronomicheskiĭ Zhurnal, Vol. 80, No. 7, 2003, pp. 589–600.*


# Calculation of Profiles of the CIV 1550 Doublet Formed in an Accretion Shock in a T Tauri Star: Axially Symmetric Radial Accretion

**S. A. Lamzin**

*Sternberg Astronomical Institute, Universitetskiĭ pr. 13, Moscow, 119899 Russia*

Received November 15, 2002; in final form, January 10, 2003

**Abstract**—We have calculated profiles for the CIV 1550 doublet arising in an accretion shock in a T Tauri star assuming that (i) the accretion zone at the stellar surface is axially symmetric (a circular spot or spherical belt), (ii) the velocity and density of the gas in front of the shock do not vary within the accretion zone, and (iii) the gas falls radially inward toward the star. The calculated CIV 1550 profiles differ qualitatively from those observed in the spectra of T Tauri stars, probably because the velocity of the infalling gas in T Tauri stars has a tangential component of some tens of km/s due to the nonradial magnetic field near the stellar surface. © *2003 MAIK "Nauka/Interperiodica".*

## 1. INTRODUCTION

Calculations of the structure of accretion shocks in classical T Tauri stars [1, 2] indicate that, if the density of the infalling gas is $N_0 > 3 \times 10^{10}$ cm$^{-3}$, the depth of the region at which the CIV 1550, NV 1240, OVI 1035, and SiIV 1400 resonance doublets are formed is much smaller than the radius of the star. This makes it possible to consider the radiation transfer in these lines in a plane-parallel model. In our previous study [3], we calculated the profiles of these lines in such an approximation. For each line, we obtained the dependence $I_\nu = I_\nu(\mu)$, where $\mu$ is the cosine of the angle between the normal to the surface of the plane shock and the line of sight.

Let $d$ be the distance to the star and $R_*$ be its radius. Then, the flux $F_\nu$ in a line formed in an accretion shock observed at the Earth can be determined using the dependence $I_\nu(\mu)$ obtained in [3], with the formula [4]

$$F_\nu = \frac{1}{d^2}\int_{S_{ac}} \mu I_\nu(\mu)\mathrm{d}S, \qquad (1)$$

where $dS$ is an element of the stellar surface area. The integration in (1) is carried out over that part of the accretion zone located on the stellar hemisphere facing the Earth and not obscured by the disk.

If the angle between the magnetic-field axis and rotational axis of the star is not too large, we expect the accretion zone to be axially symmetric; the velocity $V_0$ and density $N_0$ of the infalling gas are approximately the same in all points of the zone. The accretion zone is then either a spherical spot or a spherical belt, and these are the two geometries that will be considered here. We will assume that the gas falls radially onto the star; i.e., we neglect the tangential component of the velocity. Finally, we will assume that the disk obscures that part of the accretion disk located below the equatorial plane. This is obviously the case for the classical T Tauri stars, where the inner boundary of the disk reaches the surface of the star (see below, as well as [3]).

We introduce a rectangular Cartesian coordinate system with its origin at the center of the star. Let $OK$ be the ray connecting the center of the star and the Earth, and $OP$, the axis of symmetry of the accretion zone (a spot or belt); point $P$ is on the stellar surface (Fig. 1). Let the $Z$ axis coincide with the rotational axis of the star and the $X$ axis lie in the plane containing the $Z$ axis and the ray $OK$. We relate the Cartesian coordinates to a spherical coordinate system with the polar angle $\theta$ measured from the $OZ$ axis and the azimuth $\varphi$ measured from $XOZ$ plane in the standard way.

The coordinates of the point $K$ will then be constant ($\theta = i$, $\varphi = 0$, where $i$ is the inclination of the stellar rotational axis to the line of sight). Due to the rotation of the star, the azimuth of the point $P$ ($\theta = \theta_0$, $\varphi = \varphi_0$) will vary with time $t$ according to the law

$$\varphi_0 = 2\pi\frac{t}{T}, \qquad (2)$$

where $T$ is the rotational period of the star.

Applying the cosine theorem to the spherical triangle $KPN$, we obtain [5]

$$\cos\theta_P = \cos\theta_0\cos i + \sin\theta_0\sin i\cos\varphi_0. \qquad (3)$$

The quantity $\cos\theta_P$ does not change when $\varphi_0$ is replaced by $-\varphi_0$. Since $OP$ is the symmetry axis

1063-7729/03/4707-0540$24.00 

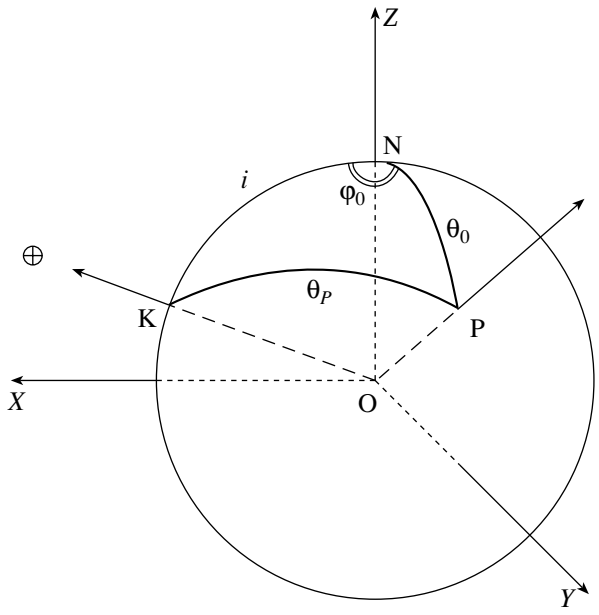


**Fig. 1.** Sketch illustrating the derivation of the expression for $\cos\theta_P$. See text for details.

of the accretion zone, this means that identical profiles will be seen from the Earth at rotational phases that are symmetric with respect to $\varphi_0 = \pi$; i.e., $\psi \equiv \{t/T\} = 0.5$. Here, $\{\}$ denotes a fractional part of a number. Consequently, it is necessary to calculate profiles only for $0 \le \varphi_0 \le \pi$; i.e., $0 \le \psi \le 0.5$. In this case, (3) can be used to unambiguously determine the angle $\theta_P$ for any time. The inclination of the stellar rotational axis to the line of sight $i$ and the position of the center of the accretion zone $P$, described by the angle $\theta_0$, are free parameters of the problem.

Since $dS = \mathrm{R}_*^2 \sin\theta \mathrm{d}\theta\mathrm{d}\varphi$, after normalizing the observed profile to the maximum value of $F_\nu^{\max}$, relation (1) is transformed to the form

$$\mathcal{F}_\nu \equiv \frac{F_\nu}{F_\nu^{\max}} = \int \sin\theta \mathrm{d}\theta \int \mu I_\nu(\mu)\mathrm{d}\varphi. \qquad (4)$$

Further, we will use (4) to calculate the profiles of the CIV 1548, 1551 doublet components. The lines of the NV 1240, OVI 1035 and SiIV 1400 doublets in the classical T Tauri spectra studied [6–11] have intensities that are too low for them to be compared with the calculated profiles.

## 2. A CIRCULAR SPOT

Let us assume that the accretion zone is a circular spot with its center at the point $P$ and an angular radius of $\Delta\theta_0$. The position of the spot center relative to the rotational axis (the angle $\theta_0$ in Fig. 1) and the inclination $i$ of the rotational axis to the line of sight are additional parameters of the problem. We will calculate the profiles of the CIV 1550 doublet lines for a set of values $i$, $\Delta\theta_0$, and $\theta_0$ for various phases of the rotational period $\varphi_0$ from 0 to $\pi$.

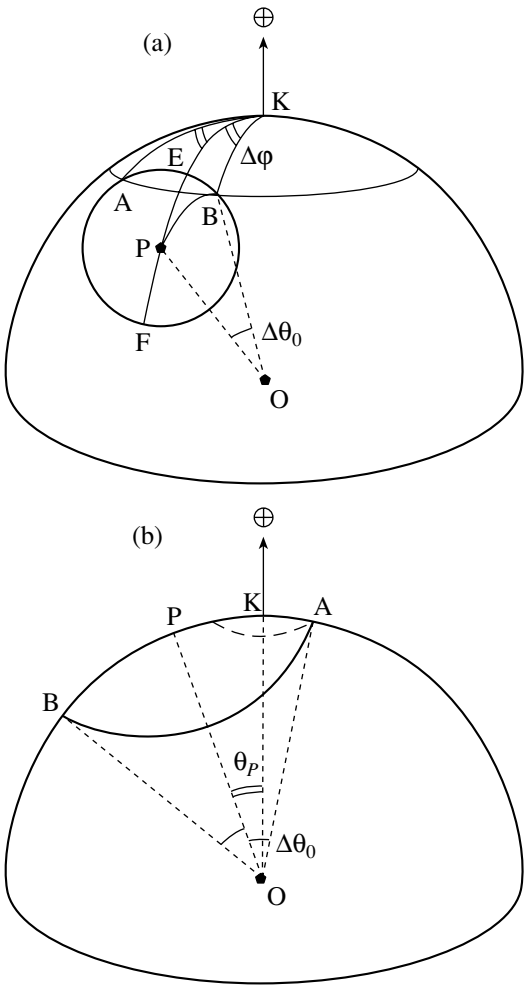


**Fig. 2.** Sketch illustrating the derivation of the expression for $\Delta\varphi$, $\mu_{\max}$, and $\mu_{\min}$ when the $OK$ axis (a) lies beyond the accretion spot and (b) intersects this spot. See text for details.

We will use spherical coordinates with the polar axis directed toward the Earth (the $OK$ axis). The polar angle $\theta$ is measured from this axis, and the azimuth $\varphi$ is measured from the plane passing through the $OK$ and $OP$ axes. Our assumption that the gas falls radially onto the star implies that the angle between the normal to the shock front at the point with coordinates $(\theta, \varphi)$ and the line of sight is $\theta$, while $\mu = \cos\theta$ and does not depend on $\varphi$.

Now, to calculate the profile using (4), we must specify the limits for the integration over $\theta$ and $\varphi$. Let us first consider the case when the $OK$ axis lies beyond the spot; i.e.,

$$\Delta\theta_0 < \theta_P. \qquad (5)$$

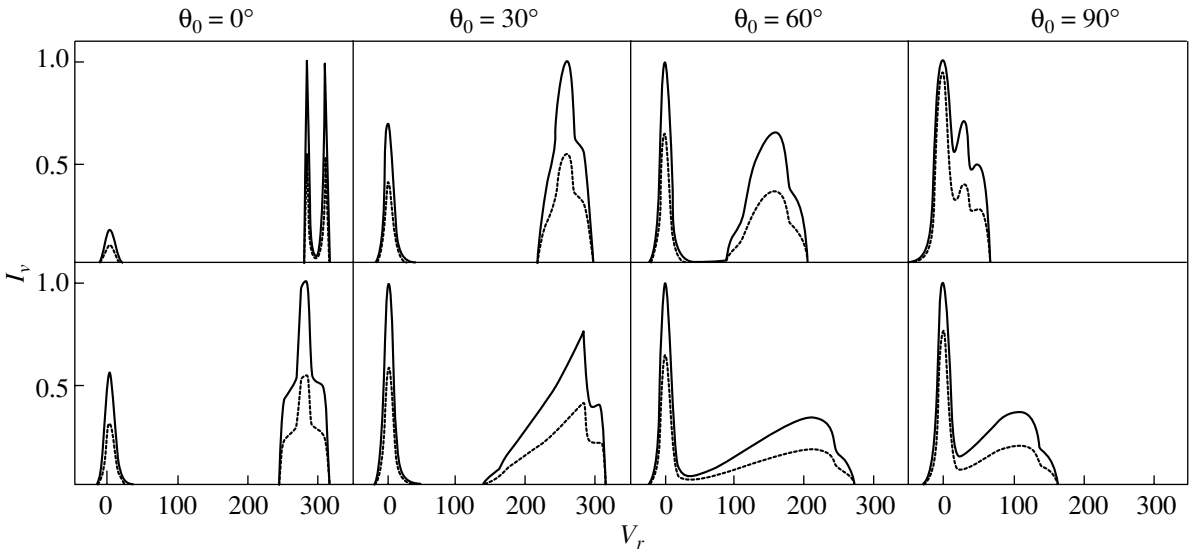


**Fig. 3.** CIV 1548.2 (solid) and CIV 1551.8 (dotted) profiles calculated for a circular spot for $i = 0$. The upper and lower rows of profiles were obtained for small and large spots, ($\Delta\theta_0 = 10°$) and ($\Delta\theta_0 = 30°$), for various positions of the spot center relative to the pole, described by the angle $\theta_0$. In all cases, $V_0 = 300$ km/s and $\log N_0 = 11.0$.

We can see from Fig. 2a that, in this situation, the value of $\theta$ in the spot varies from $\theta_{\min} = \theta_P - \Delta\theta_0$ (the arc $KE$) to $\theta_{\max} = \theta_P + \Delta\theta_0$ (the arc $KF$). Recall that the angle $\theta_P$ is found using (3).

Concerning the limits of the integration over $\varphi$, we note first and foremost that the spot is symmetric about the "central meridian" $KP$. Therefore, the extent of the parallel $AB$ (i.e., the isoline $\theta = \text{const}$) inside the spot is twice the angle $\Delta\varphi$ (Fig. 2a). Applying the cosine theorem in the spherical triangle $KPB$, we obtain

$$\cos\Delta\theta_0 = \cos\theta_P\cos\theta + \sin\theta_P\sin\theta\cos\Delta\varphi.$$

Since $\Delta\varphi \le \pi$,

$$\Delta\varphi(\Delta\theta_0) = \arccos\left(\frac{\cos\Delta\theta_0 - \cos\theta_P\cos\theta}{\sin\theta_P\sin\theta}\right). \quad (6)$$

Taking into account the fact that $I_\nu = I_\nu(\mu)$ and $\Delta\varphi = \Delta\varphi(\mu)$, we can write (4) in the form

$$\mathcal{F}_\nu = \int\limits_{\mu_{\min}}^{\mu_{\max}} \mu I_\nu \Delta\varphi \mathrm{d}\mu. \quad (7)$$

Here, $\mu_{\max} = \cos\theta_{\min}$ and $\mu_{\min} = \cos(\theta_{\max})$ for $\theta_{\max} < \pi/2$ and $\mu_{\min} = 0$ for $\theta_{\max} \ge \pi/2$, since only the points on the hemisphere facing the observer are visible.

If the $OK$ axis passes inside the spot, i.e.,

$$\theta_P \le \Delta\theta_0, \quad (8)$$

the minimum value of $\theta = 0$, so that $\mu_{\max} = 1$, and two possible cases must be considered to determine the limits of the integration over $\varphi$ in (4). Let us consider Fig. 2b, where the star is projected onto the plane of the sky, so that the plane containing the $OK$ and $OP$ rays is also in the plane of the sky. We can see that the parallel lines $\theta = \text{const}$ for $\theta \le \theta_b = \Delta\theta_0 - \theta_P$ will be completely inside the spot, so that $\Delta\varphi = \pi$. The parallel lines with $\theta_b < \theta \le \theta_P + \Delta\theta_0$ will go beyond the spot, intersecting it at the point with azimuth $\Delta\varphi$, which is specified by (6), as before. The boundary parallel $\theta = \theta_b$ is shown in Fig. 2b by the dashed line. Thus, when the $OK$ axis intersects the spot, (7) is transformed to the form

$$\mathcal{F}_\nu = \int\limits_{\mu_{\min}}^{\mu_b} \mu I_\nu \Delta\varphi \mathrm{d}\mu + \pi\int\limits_{\mu_b}^{1} \mu I_\nu \mathrm{d}\mu, \quad (9)$$

where $\mu_b = \cos(\Delta\theta_0 - \theta_P)$ and $\mu_{\min} = \cos(\Delta\theta_0 + \theta_P)$.

Figure 3 presents the calculated CIV 1548 (solid) and CIV 1551 (dotted) line profiles for the case $V_0 = 300$ km/s, $\log N_0 = 11.0$, and the line of sight coincident with the stellar rotational axis ($i = 0$). According to (3), the angle $\theta_P$ is independent of $\varphi_0$, and the profiles should therefore not vary with time. The upper row of profiles was calculated for a "small" spot with size $\Delta\theta_0 = 10°$ for various positions of the spot center relative to the rotational axis ($\theta_0 = 0°$, 30°, 60°, and 90°); the lower row was calculated for the same $\theta_0$ but for a "large" spot with size $\Delta\theta_0 = 30°$. We can see that both doublet components display essentially the same profile; therefore, below,

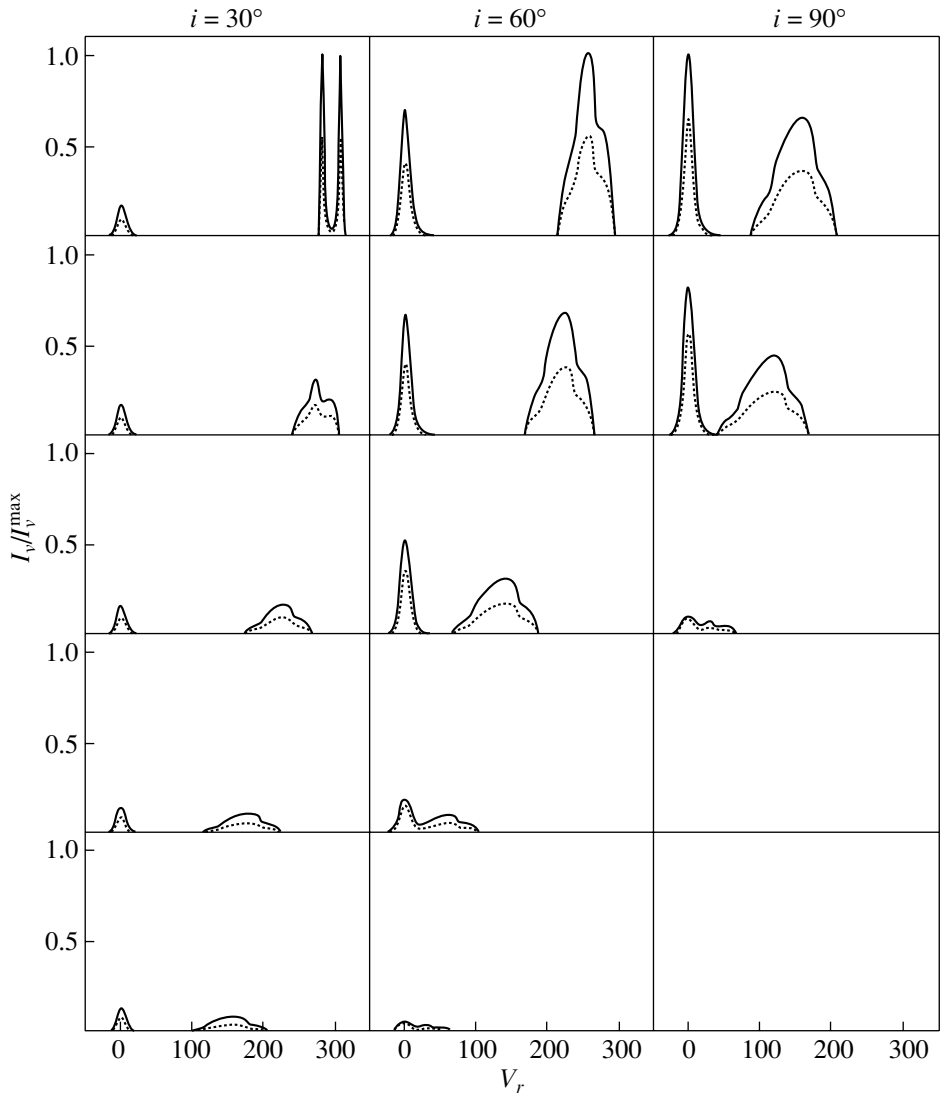


**Fig. 4.** Variations of profile shape for a small spot ($\Delta\theta_0 = 10°$) whose center is separated from the pole by $\theta_0 = 30°$ as a function of the phase of the rotational period $\psi$ for inclinations $i = 30°$, $60°$, and $90°$. From top to bottom, The profiles were calculated for $\psi = 0$, 1/8, 1/4, 3/8, and 1/2. As in Fig. 3, $V_0 = 300$ km/s and $\log N_0 = 11.0$.

we will not indicate which specific line, CIV 1548 or CIV 1551, we are considering.

Inside the small spot, whose center coincides with the pole of the star ($\theta_0 = 0$), $\mu$ varies very slightly, from 0.985 to 1. For this reason, the line profile appears almost the same as in the case of a plane shock observed perpendicular to the shock front. Recall that the lines considered are formed in two regions [2]: in front of the shock, where the gas velocity is almost constant and equal to $V_0$, and behind it, where the gas velocity is nearly two orders of magnitude smaller. For this reason, in a plane-parallel shock, the profiles of these lines consist of two components [3]: the "zero" component near $V_r = 0$ and a two-peaked "red" component displaced toward longer wavelengths by $V_r = V_0\mu$, where $\mu$ is the cosine of the angle between the normal to the shock front and the line of sight. If $V_0\mu$ exceeds the extent of the red wing of the zero component, the profile contains two separate peaks; if not, the components overlap (see [3] for details).

When the center of the small spot is displaced from the pole of the star toward the equator, the interval of $\mu$ inside the spot increases, while $\mu_{\min}$ in (7) decreases. It is obvious that this results in an increase of the intensity of the zero component and broadening of the red component. At the same time, the intensity maximum of the red component shifts toward $V_r = 0$, and the components overlap if $\theta_0$ is sufficiently large.

For a specified position of the spot center relative to the pole, the larger the size of the spot, the larger the interval of $\mu$. Therefore, in the case of a large spot

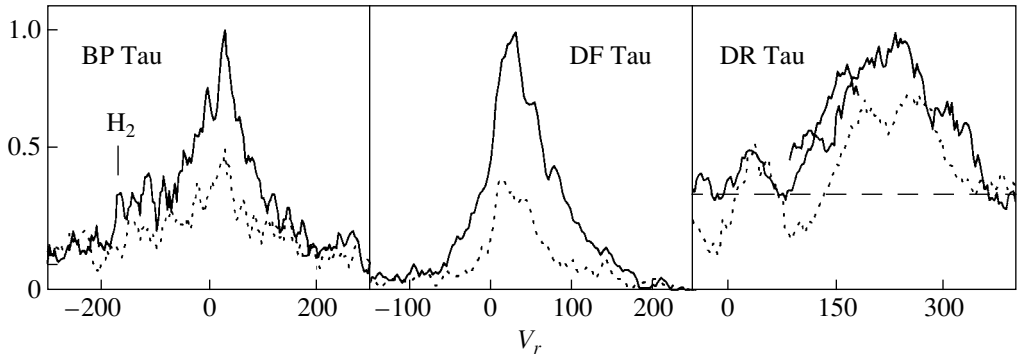


**Fig. 5.** CIV 1548.2 (solid) and CIV 1551.8 (dotted) line profiles in the spectra of BP Tau, DF Tau, and DR Tau. All the profiles are normalized to the maximum of the CIV 1548.2 line. For BP Tau, the positions of the $R(3)$ 1547.3 molecular hydrogen line and of the line superimposed on the blue wing of the CIV 1548 line are marked. The CIV 1548.2 line of DR Tau falls on the boundary of two echelle orders; for this reason, its profile consists of two partially overlapping curves. The continuum level for this star is shown by the dashed line.

($\Delta\theta_0 = 30°$ the lower row in Fig. 3) and the profiles appear broader.

If the inclination of the rotational axis to the line of sight differs from zero ($i > 0$), then, according to (2) and (3), the profile shape should vary with time. Let us first consider a small spot whose center is a distance $\theta_0 = 30°$ from the pole, with the velocity and density of the infalling gas the same as in Fig. 3, $V_0 = 300$ km/s and $\log N_0 = 11.0$. Figure 4 shows the corresponding profiles at phases (from top to bottom) $\psi = 0$, 1/8, 1/4, 3/8, and 1/2 for $i = 30°$, 60°, and 90°. (Recall that the profiles for phases $\psi$ and $1 - \psi$ are identical.) In this and other figures in this section, all the profiles for each $i$ are normalized to the maximum corresponding to zero phase.

It is obvious that, when $i = 30°$ and $\psi = 0$, the visibility conditions for a spot are the same as for $\theta_0 = 0°$ in Fig. 3, so that the profiles for these two cases are identical. The subsequent longitude shift of a spot increases the $\mu$ interval within the accretion zone, increasing the relative intensity of the zero component, while the red component becomes blurred and approaches zero. The average $\mu$ for the entire spot also decreases with increasing phase, resulting in a decrease of the total intensity of the spot in accordance with (1). In addition, at phases close to 0.5, some fraction of the spot is situated in the hemisphere that is not visible from the Earth. This effect is especially pronounced for large inclinations: when $i = 90°$, we see exactly half the spot when $\psi = 1/4$, and the spot is not visible at all when $\psi = 3/8$ and $\psi = 1/2$.

One characteristic feature of all the profiles is that they display either two separate components or (when the components merge) an extent of the blue wing smaller than 100 km/s. This is also true in the case of a small spot at a distance $\theta_0 = 60°$ from the pole, even if the velocity of the infalling gas $V_0$ increases to 400 km/s. Note that the shape of the profiles is almost independent of the density of the infalling gas; therefore, we will only consider the case $\log N_0 = 11.0$.

The ratio of the areas of the spot and of the hemisphere facing the observer is

$$f \equiv \frac{S_{ac}}{2\pi R_*^2} = \frac{1 - \cos\Delta\theta_0}{2}, \qquad (10)$$

so that $f \simeq 0.7\%$ for a small spot. Exactly this value of $f$ was found in [12] for the accretion zone of BP Tau, while an even smaller value was obtained in [13]: $f \simeq 0.4\%$. Figure 5 presents the profiles of the CIV 1550 doublet components in the spectrum of BP Tau [6]. We can see that the lines display a single-component profile, with their red wings extending to +200 km/s. It follows that, if $f < 1\%$ for BP Tau, the accretion zone cannot be a circular spot. The same is true for DF Tau, since the lines of the CIV 1550 doublet components likewise have a single peak with an extended red wing similar to that of BP Tau [9] (Fig. 5).

In the case of a large spot ($\Delta\theta_0 = 30°$), $f \simeq 6\%$, almost an order of magnitude larger than for a small spot. However, our calculations indicate that the characteristic profile shape found for the small spot is preserved in this case. This is clearly visible in Fig. 6, calculated for a large spot with $\theta_0 = 60°$ and $V_0 = 400$ km/s. The characteristic features of the profile shape cannot be removed by considering larger values of $\Delta\theta_0$, indicating that this model is not applicable to BP Tau and DF Tau.

Figure 5 also presents CIV 1550 doublet profiles in the spectrum of DR Tau taken from [11]. Due to the low signal-to-noise ratio, it is difficult to be sure whether the emission feature close to zero velocity is real. If it is real, its maximum is displaced toward

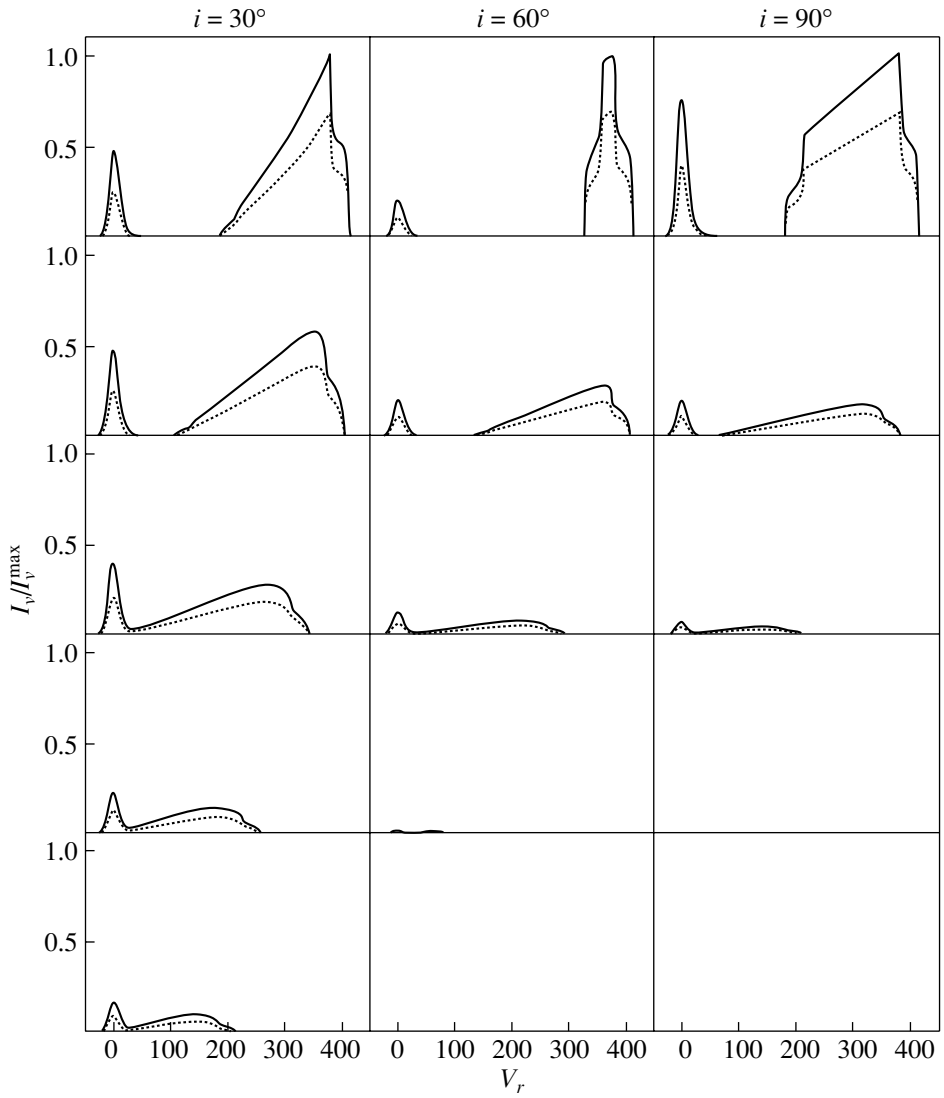


**Fig. 6.** Same as in Fig. 5 for the larger spot with $\Delta\theta_0 = 30°$, with $\theta_0 = 60°$, $V_0 = 400$ km/s, and $\log N_0 = 11.0$.

the red by roughly 40 km/s, in contradiction with the calculations: it follows from Figs. 3 and 6 that the displacement of the zero-component maximum in two-component profiles cannot exceed 10 km/s. (All the profiles in Fig. 5 have been corrected for the radial velocity of the star.) If this emission line is not a carbon feature, this means that the intensity of the zero component of the profile relative to the red component is much smaller than predicted by the calculations. Thus, the considered model of a circular spot with homogeneous and radial accretion is likewise not applicable to DR Tau.

## 3. A SPHERICAL BELT

Let us now consider the case when the accretion zone on the stellar surface forms a spherical belt symmetric about the $OP$ axis (Fig. 1). In other words, the accretion zone is the locus of the points on a sphere whose radius vectors form an angle $\Theta$ with the $OP$ axis, with $\Theta_1 \le \Theta \le \Theta_2$. Along with the angle $\theta_0$ describing the position of the symmetry axis relative to the rotational axis, $\Theta_1$ and $\Theta_2$ are the free parameters of the problem. A spherical belt can be represented as the difference of two circular spots of the sort considered above with their centers at the point $P$ and their angular radii $\Delta\theta_0$ equal to $\Theta_2$ and $\Theta_1$. It follows that (7) can be used to calculate the line profiles in the case of a spherical belt, if the limits of integration over $\mu$ are changed accordingly and the expression for $\Delta\varphi$ is modified (see Appendix).

Let us first consider the case of zero inclination of the rotational axis to the line of sight, $i = 0$. Then, according to (3), the angle between the belt symmetry axis and the line of sight is $\theta_P = \theta_0$; i.e., it does not vary with time. Figure 7 presents the calculation

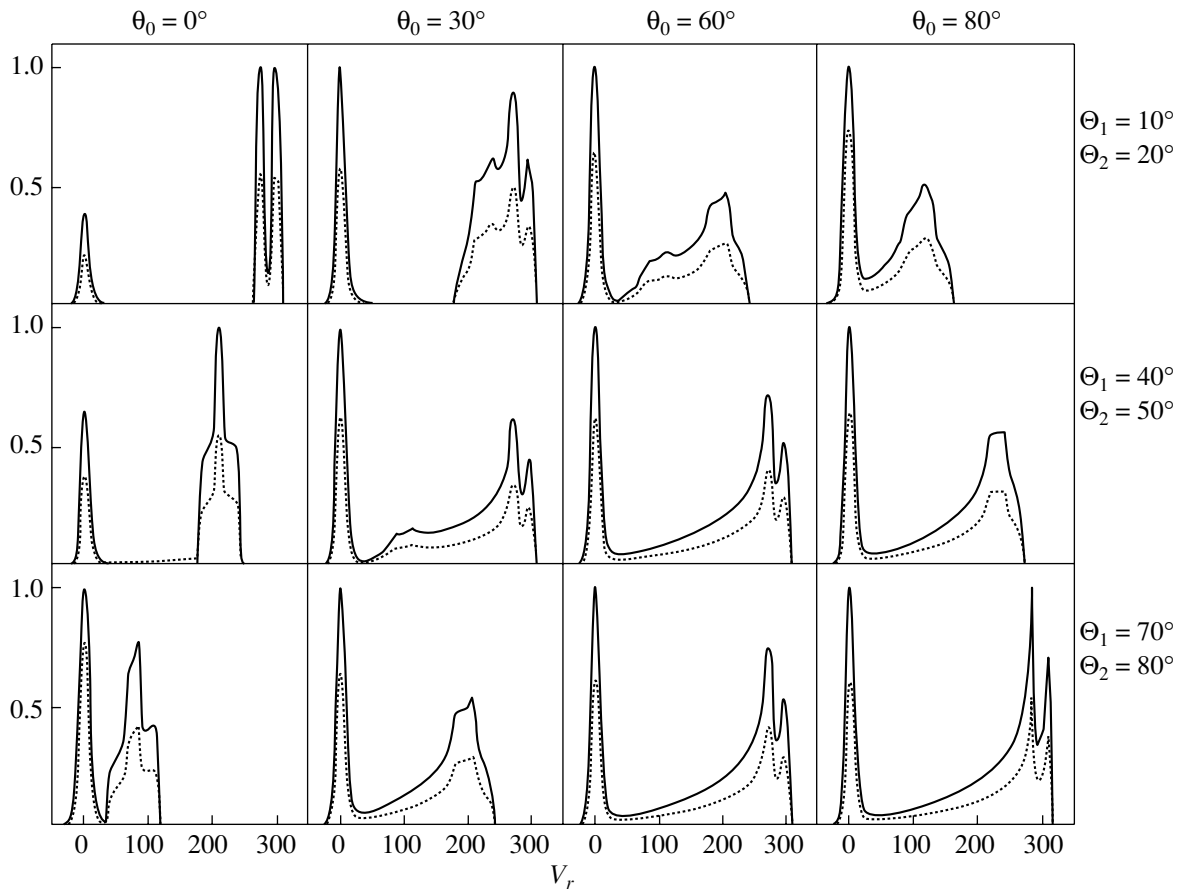


**Fig. 7.** The CIV 1550 doublet profiles for the case when the accretion zone forms a spherical belt with width $\Theta_2 - \Theta_1 = 10°$ and the line of sight coincides with the rotational axis of the star ($i = 0°$). The upper row of profiles was calculated for $\Theta_1 = 10°$ and $\Theta_2 = 20°$, with $\theta_0 = 0°$, 30°, 60°, and 90°. Profiles were also calculated for the same $\theta_0$ values and $\Theta_1 = 40°$, $\Theta_2 = 50°$ (middle row) and $\Theta_1 = 70°$, $\Theta_2 = 80°$ (lower row). See text for details.

results for a spherical belt with a constant width of $\Theta_2 - \Theta_1 = 10°$ and the accreted-gas parameters $V_0 = 300$ km/s and $\log N_0 = 11.0$.

The left column of profiles was calculated for $\theta_0 = 0°$ (the line of sight crosses the belt symmetry axis) for various positions of the belt boundary. The upper plot corresponds to $\Theta_1 = 10°$ and $\Theta_2 = 20°$; the middle, to $\Theta_1 = 40°$ and $\Theta_2 = 50°$; and the lower, to $\Theta_1 = 70°$ and $\Theta_2 = 80°$.

When ($\theta_0 = i = 0°$), $\mu$ varies within the belt from $\cos\Theta_2$ to $\cos\Theta_1$. When $\Theta_1 = 10°$ and $\Theta_2 = 20°$, this corresponds to the interval from 0.94 to 0.98. Therefore, the line profile displays approximately the same (two-component) shape as in the case of a plane-parallel shock observed for $\mu \simeq 0.96$. As the boundary of the belt approaches the equator of the star, the interval of $\mu$ within the belt increases, while $\mu_{\max}$ decreases. Because of this, the red component of the profile "blurs" and approaches the zero component. The relative area of the spherical belt is

$$f = \frac{\cos\Theta_1 - \cos\Theta_2}{2} = \sin\left(\frac{\Theta_2 - \Theta_1}{2}\right) \times \sin\left(\frac{\Theta_2 + \Theta_1}{2}\right).$$

Consequently, the area of a belt with constant width depends only on the position of its median line, i.e., on $\Theta_{12} = (\Theta_2 + \Theta_1)/2$. When $\Theta_{12} = 15°$, 35°, and 75°, the area of the belt is $f \simeq 2.3$, 6.2, and 8.4%, respectively.

The second column of profiles was calculated for the same positions of the belt with $\Theta_2 - \Theta_1 = 10°$ relative to the rotational axis, i.e., for the same $\Theta_{12}$ but assuming that the belt symmetry axis is inclined at an angle $\theta_0 = 30°$ to the rotational axis. Due to the increase in the $\mu$ interval inside the belt, the short-wavelength wing of the red component of the profiles becomes more extended and the components overlap in higher-latitude belts, in contrast to the case when $\theta_0 = 0°$. This effect is even more pronounced

for $\theta_0 = 60°$ and $\theta_0 = 90°$ (profiles in the third and fourth columns of Fig. 7, which were also calculated for $\Theta_2 - \Theta_1 = 10°$ and $\Theta_{12} = 15°$, 35°, and 75°).

All the profiles in Fig. 7 display the same characteristic feature as those obtained for a circular spot: they either consist of two clearly visible components, or (when these components merge) have a blue wing with an extent smaller than 100 km/s. Our calculations indicate that this feature remains in the set of profiles obtained for a belt with width that is twice as large; i.e., with $\Theta_2 - \Theta_1 = 20°$. Moreover, this feature cannot be removed by further increasing the belt width or by varying the velocity $V_0$ or density $N_0$ of the infalling gas.

Consequently, for the same reasons as in the case of a circular spot, the model with a spherical belt observed at the angle $i = 0$ is not applicable to either DF Tau or BP Tau. The same is true for DR Tau, since Fig. 7 shows that two-component profiles display as small a displacement of the zero component toward the red in the case of a spherical belt as in the spot models. In addition, the ratio of the zero- and red-component intensities is even larger for a belt than for a spot.

We will show that this is not due to the specific orientation ($i = 0$) of the system relative to the observer for which the profiles in Fig. 7 were calculated. It follows from (3) that $\cos\theta_P$ does not change when $\varphi$ is replaced by $-\varphi$ when $i > 0$; as $\varphi$ increases from 0 to $\pi$, $\cos\theta_P$ decreases monotonically from $\cos(i - \theta_0)$ to $\cos(i + \theta_0)$; i.e., it lies in the interval considered in the case $i = 0$, when $\theta_P = \theta_0$. However, the profile shape is unambiguously determined by $\theta_P$, $\Theta_1$, and $\Theta_2$ (see Appendix); therefore, when $i > 0$, the profiles for the spherical belt should display all the characteristic features noted for $i = 0$. Consequently, the spherical belt model is also unable to explain the line profiles observed for BP Tau, DF Tau, and DR Tau when $i > 0$; there is therefore no point in considering how the profiles should vary with time as a function of the rotational phase.

## 4. ORIGIN OF THE DIFFERENCE BETWEEN THE CALCULATED AND OBSERVED PROFILES

Recall that we calculated the profiles of the CIV 1550 doublet under the following assumptions:

(a) the accretion zone has the shape of a spot or spherical belt;

(b) the velocity and density of the accreted gas are the same at all points of the accretion zone;

(c) the gas falls onto the star strictly radially.

The discrepancy between the theory and observations implies that the accretion of gas in classical T Tauri stars cannot be described using this set of assumptions. Which of them must be altered to remove the discrepancy? To answer this question, we recall that the difference is due to two features in the spectrum of a plane-parallel shock observed at an angle $\beta$ to the normal [3].

First, the CIV 1550 lines are formed both in front of the shock, where the gas moves with the radial velocity $V_0 \cos\beta$ relative to the observer, and behind the accretion-shock front, where the gas velocity is almost zero. This results in the two-component structure of the line profiles; the two components begin to merge only when the angle $\beta$ is large enough that the total half-width of the components becomes smaller than $V_0 \cos\beta$.

Second, in the considered intervals of $V_0$ and $N_0$, both the zero and red component display half-widths are smaller than 30 km/s, so that the extent of the blue wing of the resulting profile does not exceed 60 km/s when the components merge.

According to (1), the profile of the accretion shock is the sum of the profiles of plane shocks with weights $\mu$ equal to the cosine of the angle $\beta$ between the local normal to the shock front and the line of sight. The sum of the red components of the local profiles observed at various angles forms a portion of the profile at radial velocities from $V_r = V_0\mu_{\min}$ to $V_r = V_0\mu_{\max}$, whereas the intensities of the zero components are simply summed (with the weights $\mu$).

This last circumstance results in the characteristic feature of the calculated profiles; in other words, it is this that leads to the inconsistency between the theory and observations. This feature cannot be removed by varying the shape of the accretion zone or by specifying different $V_0$ values in the accretion shock (inhomogeneous accretion).[1] The intensities of the zero components will still be summed. However, since they are summed with the weights $\mu$, we cannot rule out the possibility that we will obtain single-peaked profiles with their maximum close to $V_r = 0$ and extents of their red wings up to +200 km/s, similar to those observed in the spectra of BP Tau and DF Tau, for some nontrivial geometry of the accretion zone and distribution $V_0 = V_0(\theta, \varphi)$ within this zone. However, it is clear that the observed profile of DR Tau cannot be formed in this way: its zero component is either virtually absent or displaced toward the red by approximately 40 km/s, whereas the line maximum falls at +250 km/s (Fig. 5).

It appears that such a profile can be obtained if the velocity vector of the infalling gas has not only a radial component $V_0$ but also a tangential component

[1] According to [3], the shape of the CIV 1550 profile depends weakly on the density of the falling gas for $\log N_0 < 13$.

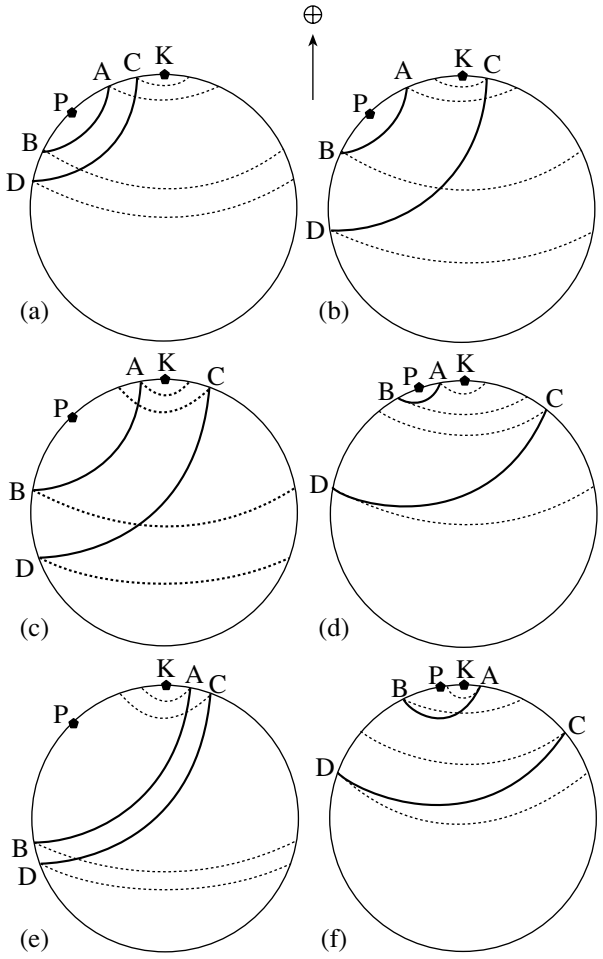


**Fig. 8.** The integration limits in (7) for the profile calculation in the case of a spherical belt. Diagrams (a–f) refer to cases 1–6 in the text. The arrow indicates the direction toward the Earth, which is the same for all cases; the dotted lines show the limiting values for $\mu$ (when they are crossed, the expression for $\Delta\varphi$ changes its form).

$V_t$. When $V_t \neq 0$, the radial velocity $V_r$ of the zero components relative to the Earth will not only differ from zero but will also vary within the accretion zone. Qualitatively, therefore, their behavior when they are summed is similar to that of the red components, for which the difference $V_r$ is due to the radial component of the infall velocity: the combined profile of the zero components will blur, and its peak intensity will decrease.

Based on this, we suggest that the classical T Tauri profiles presented in Fig. 5 can be reproduced when the tangential component of the velocity of the infalling gas is taken into account. Moreover, for specific shapes of the accretion zone, its orientation relative to the observer, and/or the dependence $V_t = V_t(\theta, \varphi)$, we can also obtain a shift of the centroid of the combined zero component toward either the blue or red. This assertion is based on our study [14], in which we calculated the profiles of optically thin SiIII] 1892 and CIII] 1909 lines originating in accretion shocks in classical T Tauri stars in the case of homogeneous accretion. The profiles were calculated for a spherical belt with various $\Theta_1$ and $\Theta_2$, and we investigated the dependence of the profile shape on the tangential component of the infalling gas velocity.

The calculations of [14] free us of the need to calculate the CIV 1550 profiles for $V_t \neq 0$ to demonstrate how this parameter affects the profile shape. On the other hand, no reliable data on time variations of the CIV 1550 profiles are currently available for any classical T Tauri star, although the variability itself has been reliably established (see, for example, [7]). Given the large number of free parameters (the zone geometry and distribution of $V_0$ and $V_t$ within the zone), there is likewise currently no point in calculating profiles with $V_t \neq 0$ to derive the characteristics of classical T Tauri stars. Therefore, we will restrict ourselves to the statement that the difference between the calculated and observed profiles is likely due to the existence of a significant tangential component of the velocity of the accreted gas, of the order of several tens km/s.

## 5. CONCLUSIONS

A comparison of the calculated profiles of the CIV 1550 doublet with those observed in the spectra of classical T Tauri stars shows that the accretion of gas onto young stars cannot be simultaneously axially symmetric, homogeneous, and radial. In our opinion, the discrepancy between the calculated and observed profiles is due primarily to the existence of a substantial tangential velocity component of the gas falling onto the star.

On the other hand, the projected rotational velocities $v \sin i$ of BP Tau, DF Tau, and DR Tau are very small; for example, $v \sin i \leq 10$ km/s for DR Tau. Therefore, the tangential velocity component of the accreted gas cannot be explained only by the axial rotation of the star in the region of formation of the accretion shock. Magnetosphere models suggest that the infalling gas moves along lines of the large-scale magnetic field of the star. Thus, the fact that the infalling gas possesses a tangential velocity component exceeding $\sim$30 km/s implies that the direction of the magnetic-field lines of classical T Tauri stars differs appreciably from the radial direction near the stellar surface, which seems quite natural.

Intense outflows of matter are observed in the vicinities of classical T Tauri stars; magnetospheric models suggest that the high-velocity component of the wind is formed in a disk, close to the corotation zone [16]. It cannot be ruled out that gas may be heated to high temperatures in this region of the disk,

enabling it to radiate in the CIV 1550 doublet lines. Ultraviolet spectra of a large number of young stars whose disks have known orientations relative to the line of sight will become openly available from the Hubble Space Telescope archive in the near future. Analysis of these spectra will help clarify whether it is realistic for these lines to form in the disks of these stars.

## 6. ACKNOWLEDGMENTS

The author thanks the referee V.P. Grinin for useful comments. This work was supported by the Russian Foundation for Basic Research (project code 02-02-16070).

## *Appendix*

## INTEGRATION LIMITS OVER $\mu$ AND $\theta$ IN THE SPHERICAL BELT CASE

Let us consider various cases for the location of a spherical belt relative to the ray $OK$ connecting the center of the star with the Earth (Fig. 8). In Fig. 8, the star is shown such that the plane $KOP$ containing the axis of symmetry of the belt $OP$ and the ray $OK$ coincides with the plane of the sky. The crossing points of the belt's boundary and the plane are denoted $A, B, S$, and $D$, so that the arcs $PA$ and $PB$ are equal to $\Theta_1$ and the arcs $PC$ and $PD$ are equal to $\Theta_2$. In addition, the arc $PK$ is equal to the angle $\theta_P$, calculated using (3). As in the case of a spot, we will use a spherical coordinate system with its center at the point $O$, with the polar angle $\theta$ measured from the $OK$ axis and the azimuth $\varphi$ measured from the $KOP$ plane.

We introduce the notation

$$\mu_A = \cos(\theta_P - \Theta_1), \mu_\mathrm{B} = \cos(\theta_P + \Theta_1),$$
$$\mu_S = \cos(\theta_P - \Theta_2), \mu_D = \cos(\theta_P + \Theta_2).$$

It is easy to show that $\mu_D$ will be the smallest of these four values, and that $\mu_A$ will always exceed $\mu_\mathrm{B}$. Then, depending on the parameters $\theta_P$, $\Theta_1$, and $\Theta_2$, there are three possible relations between $\mu_A$, $\mu_B$, and $\mu_A$ :

$$\mu_S \le \mu_B < \mu_A, \qquad \mu_B \le \mu_S \le \mu_A,$$
$$\mu_B < \mu_A \le \mu_S.$$

For a given $\mu_A$ ($\mu_B$), the angle $\Theta_1$ ($\Theta_2$) can be both larger and smaller than the angle $\theta_P$, which doubles the number of possible relations between the polar angles $\theta$ of the points $A, B$, and $S$. Consequently, there are a total of six cases, for each of which expressions for $\mu_\mathrm{max}$ and $\Delta\varphi$ in (7) must be derived. In all cases, $\mu_\mathrm{min} = \mu_D$, but zero must be taken as the minimum $\mu$ if $\mu_D < 0$.

**Case 1.** Figure 8a shows the situation when the points $P$ and $K$ are located on different sides of the belt, which corresponds to the condition

$$\Theta_2 < \theta_P.$$

We can see that the belt will only cross isolines $\theta = \mathrm{const}$ for which $\theta_P - \Theta_2 \le \theta \le \theta_P + \Theta_2$. Consequently, $\mu_\mathrm{max} = \mu_S$ in this case. It also follows from the figure that

$$\Delta\varphi = \begin{cases} \Delta\varphi_2 & \text{for} \quad \mu_A \le \mu \le \mu_S \\ \Delta\varphi_2 - \Delta\varphi_1 & \text{for} \quad \mu_B < \mu < \mu_A \\ \Delta\varphi_2 & \text{for} \quad \mu_D \le \mu \le \mu_B, \end{cases}$$

where $\Delta\varphi_i$ ($i = 1, 2$) denotes the $\Delta\varphi$ values calculated using (6) with $\Delta\theta_0$ replaced by $\Theta_i$.

It is obvious that $\mu_\mathrm{max} = 1$ if the ray crosses the belt, and the following three possibilities arise.

**Case 2.** Let $\angle COK = \Theta_2 - \theta_P < \angle AOK = \theta_P - \Theta_1$ (Fig. 8b), which corresponds to the condition

$$\frac{\Theta_1 + \Theta_2}{2} < \theta_P \le \Theta_2.$$

Then,

$$\Delta\varphi = \begin{cases} \pi & \text{for} \quad \mu_S \le \mu \le 1 \\ \Delta\varphi_2 & \text{for} \quad \mu_A \le \mu < \mu_S \\ \Delta\varphi_2 - \Delta\varphi_1 & \text{for} \quad \mu_B < \mu < \mu_A \\ \Delta\varphi_2 & \text{for} \quad \mu_D \le \mu \le \mu_B. \end{cases}$$

**Case 3.** If (Fig. 8c)

$$\frac{\Theta_2 - \Theta_1}{2} \le \Theta_1 \le \theta_P \le \frac{\Theta_1 + \Theta_2}{2},$$

then

$$\Delta\varphi = \begin{cases} \pi & \text{for} \quad \mu_A \le \mu \le 1 \\ \pi - \Delta\varphi_1 & \text{for} \quad \mu_S \le \mu < \mu_A \\ \Delta\varphi_2 - \Delta\varphi_1 & \text{for} \quad \mu_B < \mu < \mu_S \\ \Delta\varphi_2 & \text{for} \quad \mu_D \le \mu \le \mu_B. \end{cases}$$

**Case 4.** If (Fig. 8d)

$$\Theta_1 < \frac{\Theta_2 - \Theta_1}{2} \le \theta_P \le \frac{\Theta_1 + \Theta_2}{2},$$

then

$$\Delta\varphi = \begin{cases} \pi & \text{for} \quad \mu_A \le \mu \le 1 \\ \pi - \Delta\varphi_1 & \text{for} \quad \mu_B < \mu < \mu_A \\ \pi & \text{for} \quad \mu_S \le \mu \le \mu_B \\ \Delta\varphi_2 & \text{for} \quad \mu_D \le \mu < \mu_S. \end{cases}$$

Let us now consider the situation when the points $P$ and $K$ are located on the same side of the spherical belt. Then, $\mu_\mathrm{max} = \mu_A$, and two cases must be considered to determine $\Delta\varphi$.

**Case 5.** If

$$\frac{\Theta_2 - \Theta_1}{2} < \theta_P \le \Theta_1,$$

then it follows from Fig. 8f that

$$\Delta\varphi = \begin{cases} \pi - \Delta\varphi_1 & \text{for} \quad \mu_S \le \mu \le \mu_A \\ \Delta\varphi_2 - \Delta\varphi_1 & \text{for} \quad \mu_B < \mu < \mu_S \\ \Delta\varphi_2 & \text{for} \quad \mu_D \le \mu \le \mu_B. \end{cases}$$

**Case 6.** Finally, for

$$0 \le \theta_P \le \frac{\Theta_2 - \Theta_1}{2},$$

$\Delta\varphi$ is determined as follows (Fig. 8e):

$$\Delta\varphi = \begin{cases} \pi - \Delta\varphi_1 & \text{for} \quad \mu_B < \mu \le \mu_A \\ \pi & \text{for} \quad \mu_S \le \mu \le \mu_B \\ \Delta\varphi_2 & \text{for} \quad \mu_D \le \mu < \mu_S. \end{cases}$$

These expressions should be used to divide the integration interval in (7) into separate sections in the same way this was done in the spot case [see relations (5)–(9)].

## REFERENCES


1. S. A. Lamzin, Astron. Astrophys. **295**, L20 (1995).
2. S. A. Lamzin, Astron. Zh. **75**, 367 (1998) [Astron. Rep. **42**, 322 (1998)].
3. S. A. Lamzin, Astron. Zh. **80**, 542 (2003) [Astron. Rep. **47**, 498 (2003)].
4. D. Mihalas, *Stellar Atmospheres* (Freeman, San Francisco, 1978; Mir, Moscow, 1982).
5. P. G. Kulikovskiĭ, *A Handbook for the Amateur Astronomer* [in Russian] (URSS, Moscow, 2002).
6. S. A. Lamzin, Pis'ma Astron. Zh. **26**, 273 (2000) [Astron. Lett. **26**, 225 (2000)].
7. S. A. Lamzin, Pis'ma Astron. Zh. **26**, 683 (2000) [Astron. Lett. **26**, 589 (2000)].
8. L. Errico, S. A. Lamzin, and A. A. Vittone, Astron. Astrophys. **357**, 951 (2000).
9. S. A. Lamzin, A. A. Vittone, and L. Errico, Pis'ma Astron. Zh. **27**, 363 (2001) [Astron. Lett. **27**, 313 (2001)].
10. L. Errico, S. A. Lamzin, and A. A. Vittone, Astron. Astrophys. **377**, 577 (2001).
11. A. S. Kravtsova and S. A. Lamzin, Pis'ma Astron. Zh. **28**, 748 (2002) [Astron. Lett. **28**, 676 (2002)].
12. N. Calvet and E. Gullbring, Astrophys. J. **509**, 802 (1998).
13. D. R. Ardila and G. Basri, Astrophys. J. **539**, 834 (2000).
14. S. A. Lamzin, Astron. Zh. **77**, 373 (2000) [Astron. Rep. **44**, 323 (2000)].
15. L. Hartmann and J. R. Stauffer, Astron. J. **97**, 873 (1989).
16. C. Bertout, Ann. Rev. Astron. Astrophys. **27**, 351 (1989).


*Translated by K. Maslennikov*

*Astronomy Reports, Vol. 47, No. 7, 2003, pp. 551–561. Translated from Astronomicheskiĭ Zhurnal, Vol. 80, No. 7, 2003, pp. 601–612.*


# Apsidal Motion and Physical Parameters of the Eclipsing Binary System AR Cas

**A. V. Krylov, L. V. Mossakovskaya, Kh. F. Khaliullin, and A. I. Khaliullina**

*Sternberg Astronomical Institute, Moscow State University, Universitetskiĭ pr. 13, Moscow, 119992 Russia*

Received June 26, 2002; in final form, November 27, 2002

**Abstract**—Using the four-channel automatic photoelectric photometer of the Sternberg Astronomical Institute's Tien Shan Mountain Observatory, we have acquired accurate ($\sigma_{\rm obs} \approx 0.004^m$) $WBVR$ brightness measurements for the eclipsing binary AR Cas during selected phases before eclipse ingress and after egress, as well as at the center of minima. A joint analysis of these measurements with other published data has enabled us to derive for the first time a self-consistent set of physical and geometrical parameters for the star and the evolutionary age of its components, $t = (60 \pm 3) \times 10^6$ years. We have found the period of the apsidal motion ($U_{\rm obs} = 1100 \pm 160$ years, $\dot\omega_{\rm obs} = 0.^\circ327 \pm 0.^\circ049$ years$^{-1}$) and the apsidal parameter of the primary, $\log k_{2,1}^{\rm obs} = -2.41 \pm 0.08$, with the apsidal parameter being in good agreement with current models of stellar evolution. There is an ultraviolet excess in the primary's radiation, $\Delta(U-B) = -0.12^m$ and $\Delta(B-V) = -0.06^m$, possibly due to a metal deficiency in the star's atmosphere.


## 1. INTRODUCTION

The bright northern star AR Cas (HD 221253 = BD + 57°2748 = HR 8926; $V = 4.89^m$; Sp = B4.2IV + A6V), component A of the visual multiple (seven-component) star ADS 16795, was discovered as an eclipsing system with an elliptical orbit ($e = 0.21$) as early as in 1918 by Stebbins [1] using pioneering photoelectric measurements. The star was later studied photometrically many times [2–7]. However, due to the light curve's shallow minima (Min I $= 0.13^m$; Min II $= 0.03^m$) and the relatively long orbital period ($P = 6.^{\rm d}066$), it proved difficult to acquire a good photoelectric light curve of the system, which is needed to derive reliable photometric orbital elements.

A number of spectroscopic studies of the star have been published [8–12]. Most authors have determined the spectral type of the primary to be B3V, and its rotational rate to be $v_1 \sin i = 120$–$130$ km/s. The secondary is faint ($L_2 = 0.03$), and, until recently, only the mass function of the binary, $f(M) = 0.100$, was known. In their excellent photometric study of AR Cas, Holmgren *et al.* [13] determined the secondary's spectral type (A6V) and presented radial-velocity curves for both components.

Until recently, studies of the apsidal motion of AR Cas were mainly based on the spectroscopic observations of Luyten *et al.* [9], Petrie [10], Batten [14], and Kopal [15]. Using radial-velocity curves acquired between 1908 and 1943, Petrie [10] found that the longitude of periastron $\omega$ increased by approximately 30° over this time interval and concluded that the period of the apsidal motion was 413 years. However, subsequent spectroscopic observations did not confirm this value. Moreover, the photometric light curve of AR Cas obtained by Stebbins [2] yields a longitude of periastron that contradicts the spectroscopic data. The radial-velocity curves of close binary systems often exhibit various distortions, hindering spectroscopic studies of variations of $\omega$ and of periodic variations of the $\gamma$ velocity of the center of mass. Batten [17] suggested that the very rapid, asynchronous rotation of the primary of AR Cas [9, 16] was one possible origin of this distortion, but later concluded that this effect alone could not explain the observed anomalies.

In 1971, Catalano and Rodono [5] addressed the problem of the apsidal motion of AR Cas by restricting their analysis to variations of the recurrence periods of Min I and Min II using only photometric data. They derived the period of the apsidal motion $U_{\rm obs} = 1000 \pm 34$ years. However, the fairly uncertain photometric elements prevented a trustworthy determination of the internal structure parameters of the components, $k_2$. Mossakovskaya [7] obtained a similar value, $U_{\rm obs} = 922 \pm 46$ years; however, her value of $k_{2,1}^{\rm obs}$ is three times the theoretically expected value. This suggests the possible presence of a third body in the system. This possibility has been discussed in the literature for a long time. In his spectroscopic analysis, Batten [14] subdivided the observations into

1063-7729/03/4707-0551$24.00 

**Table 1.** Absolute photometry and differential $WBVR$ measurements of the multiple star AR Cas + B

| Star | Phase | $W$ | $B$ | $V$ | $R$ | $U$ | Remarks |
|---|---|---|---|---|---|---|---|
| 1 Cas | – | 3.735(5) | 4.805(4) | 4.850(5) | 4.841(5) | 3.949(9) | Kornilov *et al.* [21] |
| AR Cas + B | $0\overset{p}{.}00$ | 4.118(3) | 4.914(2) | 5.026(2) | 5.090(3) | 4.254(3) | Min I |
| AR Cas + B | $0\overset{p}{.}04$ | 3.979(2) | 4.780(1) | 4.893(2) | 4.965(1) | 4.115(2) | Outside eclipse |
| AR Cas + B | $0\overset{p}{.}57$ | 3.977(2) | 4.776(2) | 4.890(1) | 4.960(2) | 4.114(2) | Outside eclipse |
| AR Cas + B | $0\overset{p}{.}62$ | 3.989(2) | 4.800(2) | 4.927(1) | 5.008(2) | 4.126(2) | Min II |
| AR Cas + B | $0\overset{p}{.}67$ | 3.979(2) | 4.774(1) | 4.892(2) | 4.959(1) | 4.114(2) | Outside eclipse |
| AR Cas + B | $0\overset{p}{.}96$ | 3.981(2) | 4.777(2) | 4.896(1) | 4.963(2) | 4.117(2) | Outside eclipse |
| $\Delta$Min I | | 0.138(3) | 0.136(2) | 0.132(2) | 0.126(3) | 0.138(3) | Depth of Min I |
| $\Delta$Min II | | 0.011(2) | 0.025(1) | 0.036(1) | 0.048(2) | 0.012(2) | Depth of Min II |

**Table 2.** Our photometric elements of AR Cas derived from the light curves of various authors using an iterative differential-correction method for $L_3 = 0$

| Author | Stebbins [1, 2] | Botsula and Kostylev [4] | Huffer and Collins [3] | | Catalano and Rodono [5] | | Gordon and Kron [6] | | | |
|---|---|---|---|---|---|---|---|---|---|---|
| Years of observations | 1917–1921 | 1946–1951 | 1954–1956 | | 1968 | | 1947 | 1959 | | |
| $\lambda_{mean}$, Å | 4500 | 4450 | 4200 | 5400 | 4500 | 5500 | 4200 | 4200 | 4900 | 5700 |
| $r_1$ | 0.1820 | 0.1850 | 0.1740 | 0.1770 | 0.2000 | 0.2040 | 0.1760 | 0.1620 | 0.1670 | 0.1750 |
| $r_2$ | 0.0600 | 0.0605 | 0.0560 | 0.0563 | 0.0600 | 0.0600 | 0.0565 | 0.0520 | 0.0525 | 0.0570 |
| $i$ | 85°.75 | 85°.2 | 88°.8 | 86°.6 | 83°.0 | 82°.0 | 88°.0 | 88°.6 | 87°.0 | 86°.1 |
| $e$ | 0.219 | 0.271 | 0.219 | 0.218 | 0.287 | 0.285 | 0.221 | 0.207 | 0.203 | 0.221 |
| $\omega$ | 22° | 46° | 34° | 34° | 52° | 52° | 36° | 30° | 28° | 34° |
| $L_1$ | 0.9697 | 0.9661 | 0.9667 | 0.9664 | 0.9723 | 0.9639 | 0.9820 | 0.9866 | 0.9764 | 0.9686 |
| $L_2$ | 0.0303 | 0.0339 | 0.0333 | 0.0336 | 0.0277 | 0.0361 | 0.0180 | 0.0134 | 0.0236 | 0.0314 |
| $\sigma$ | $0.012^m$ | $0.008^m$ | $0.005^m$ | $0.008^m$ | $0.005^m$ | $0.006^m$ | $0.009^m$ | $0.013^m$ | $0.010^m$ | $0.012^m$ |

several groups and detected periodic variations of the center-of-mass $\gamma$ velocity with a period of about 0.7 years. However, the existence of $\gamma$-velocity variations that would have demonstrated the presence of a third body dynamically related to AR Cas could not be confirmed in [12, 13].

The apsidal-motion period derived by Holmgren *et al.* [13] was twice the earlier values, $U_{obs} = 1938 \pm 207$ years; they also noted an appreciable disagreement between the observed and theoretical values of $k_{2,1}$.

Our current study is aimed at clarifying the situation with regard to the system's apsidal motion and elucidating the reasons for the discrepant conclusions that have been obtained in earlier studies.

## 2. OBSERVATIONS

We carried out absolute and differential $WBVR$ measurements of AR Cas [18] at the Tien Shan Observatory of the Sternberg Astronomical Institute (at an altitude of about 3000 m above sea level) in 1988–1989. The observations used a four-channel automatic photoelectric photometer [19] mounted on the 48 cm reflector of the observatory. The diaphragm had a radius of $r = 20''$, so that the other members of the visual multiple system ADS 16795 ($\rho_{A\text{-}E} = 43''$, E = $11.28^m$, $\rho_{A\text{-}CD} = 75''$, CD = $7.095^m$, and others) were excluded from the telescope field of view. Only the faint component B ($\rho_{A\text{-}B} = 1''.2$, $B = 9.3^m$) was inside the photometric field. The comparison star for the differential measurements was 1 Cas (HD 218376, HR 8797, $V = 4.85^m$, B0.5IV). The

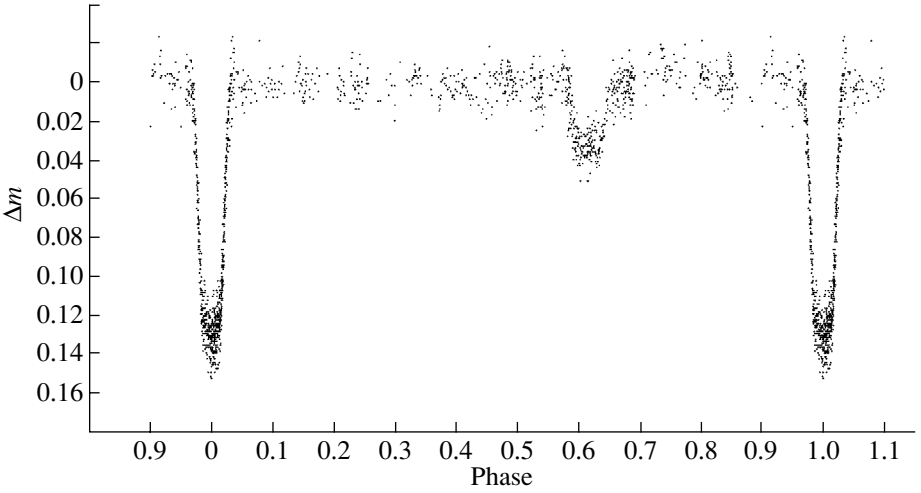


**Fig. 1.** Master light curve of AR Cas in the visual ($\lambda_{\text{mean}} \approx 5000$ Å).

averaged results of our absolute photometry and differential measurements corrected for atmospheric extinction and reduced to the standard system of [18] are presented in Table 1. Each magnitude is an average of 20 to 25 individual measurements acquired on five to eight different nights. The mean standard errors of the individual measurements are $0.006^m$, $0.004^m$, $0.004^m$, and $0.005^m$ in the $W$, $B$, $V$, and $R$ bands, respectively. The method used to correct for the atmospheric extinction is described in [20].

Our observations of AR Cas were carried out at the same time as work on the $WBVR$ catalog of bright stars of the northern sky [21]. These observations were aimed at high-precision measurements of the magnitudes and depths of minima of AR Cas in all four of these bands. On approximately forty observing nights, we obtained measurements at selected phases prior to eclipse ingress, following egress, and at the center of minima. We reduced our measured $W$ magnitudes to $U$ magnitudes using the known reaction curves of these systems [18, 22], so that we could employ the widely used and well-calibrated ($U-B$, $B-V$) two-color diagram. Though the uncertainty in this reduction can be as high as $0.015^m$, this has virtually no influence the the accuracy of the differential measurements. Table 1 also contains the results of this reduction of $W$ into $U$ magnitudes.

In addition to the described $WBVR$ observations, AR Cas was observed by one of us (L.V.M.) using the 60 cm Zeiss-600 reflector of the Sternberg Astronomical Institute's Crimean Observatory [7]. These measurements are the most accurate among previously published data and were included in the master light curve (see the next section) with the highest weight.

## 3. PHOTOMETRIC ELEMENTS

We determined the photometric elements using the iterative differential-correction method developed by Khaliullina and Khaliullin [23] for the analysis of the light curves of eclipsing systems with elliptical orbits. We first analyzed all individual light curves in various bands published by various authors. All these curves were rectified for the small reflection effect. We estimated the linear reflection coefficients $A_1$ using our outside-of-eclipse observations (Table 1) and the expression $l = A_0 + A_1 \cos\nu$, where $\nu$ is the true longitude in the orbit. All the curves were first normalized to $l = 1.00$ outside the minima, making the values of $A_0$ close to unity for all bands. The derived $A_1$ coefficients are collected in the first line of Table 4.

Table 2 presents the photometric elements of AR Cas we derived from the individual light curves in the standard notation. With the exception of $u_1$ and $u_2$, all the elements were varied freely. We fixed the darkening coefficients at their theoretical values from [24].

We use the subscript "1" and the term "primary" for the component eclipsed in the primary (deeper) minimum (Min I). The large scatter in the values for all the elements in Table 2 is evident; for example, the scatter in $r_1$ exceeds 20%. It is no wonder that different authors have arrived at considerably different values for the apsidal parameter $k_2$, since this parameter is proportional to $r^{-5}$. This scatter in the photometric elements is due, first, to the shallowness of the minima and, second, to the incompleteness and low accuracy of the individual light curves.

To improve the accuracy and completeness of the light curve, we combined all published observations in the visible ($\lambda = 4200$–$5700$ Å) to construct a master light curve ($\lambda_{\text{mean}} \approx 5000$ Å), displayed in Fig. 1. We

**Table 3.** Photometric elements of AR Cas

| | |
|---|---|
| $r_1 = 0.1754 \pm 0.0025$ | $L_1 = 0.9535 \pm 0.0006$ |
| $r_2 = 0.0573 \pm 0.0009$ | $L_2 = 0.0295$ |
| $i = 86.70 \pm 0.34°$ | $L_3 = 0.017$ |
| $e = 0.211 \pm 0.005$ | $u_1 = 0.39 \pm 0.04$ |
| $\omega_0 = 29.7 \pm 1.4°$ | $u_2 = 0.7$ (fixed) |
| $J_1/J_2 = 0.291$ | $E_{\rm I} = {\rm JD}_\odot\ 2435\,792.8982(24) \equiv {\rm JD}_0$ |
| $\sigma_{\rm O-C} = 0.0079^m$ | $E_{\rm II} = {\rm JD}_\odot\ 2435\,796.6429(70)$ |

**Table 4.** Linear reflection coefficients and luminosities for the components of the AR Cas + B system

| Component | Designation | $W$ | $B$ | $V$ | $R$ |
|---|---|---|---|---|---|
| Linear reflection coefficient | $2 \times A1$ | $-0.0021(19)$ | $-0.0035(10)$ | $-0.0036(9)$ | $-0.0040(13)$ |
| Illuminated hemisphere of the secondary | $L_2$ | 0.0101(18) | 0.0228(9) | 0.0326(9) | 0.0432(15) |
| Unilluminated hemisphere of the secondary | $L_{2f}$ | 0.0083(15) | 0.0199(8) | 0.0290(8) | 0.0392(14) |
| Visual component B | $L_3$ | 0.0049(4) | 0.0114(7) | 0.0171(9) | 0.0239(14) |
| Primary | $L_{1f}$ | 0.9868(9) | 0.9687(8) | 0.9539(7) | 0.9369(7) |

did not use the observations during Min I from [5], as the depth of this minimum was considerably ($\sim 0.03^m$) less than those derived by other authors, for reasons that are not clear. In addition, in our final reduction of the light curves, we rejected individual measurements that deviated from the mean by more than $3\sigma$. When plotting Fig. 1, we used different periods to calculate the phases of observations in the primary and secondary minima in order to compensate for their relative displacement due to the apsidal motion. However, if an eclipsing system's elliptical orbit rotates, the whole shape of the light curve varies, including the depths and widths of the minima, their relative positions, proximity effects, and other parameters. For this reason, in our analysis of long series of observations contained in the master light curve, we assumed individual values of the longitude of periastron for each time, JD: $\omega = \omega_0 + \dot{\omega}({\rm JD} - {\rm JD}_0)$. We chose the initial epoch to be ${\rm JD}_0 = {\rm JD}_\odot 2435792\overset{\rm d}{.}8892$, whereas the initial value $\omega_0$ at the time $JD_0$ and the rotation rate of the apsidal line $\dot{\omega}$ were solved for simultaneously with the other photometric elements. We discuss the problem of the apsidal motion in Section 5.

The photometric elements of AR Cas derived from our analysis of the master light curve are presented in Table 3. Some impression of the agreement between our model with spherical stars in elliptical orbits and the observations of AR Cas is given by Figs. 2 and 3, which present the observed and theoretical light curves of the system in the regions of Min I and Min II. There are no obvious systematic deviations between the curves, confirming that the adopted model adequately describes the observations. Because of the contribution from the visual companion B to the system's combined brightness ($\rho_{\rm A\text{-}B} = 1\overset{''}{.}2$, $\Delta m = V_B - V_{\rm AR\ Cas} = 4.4^m$), we assumed $L_3 = 0.017$ in the light-curve analysis. The photometric elements in Table 3 indicate that we were able to improve the accuracies of most parameters by an order of magnitude by combining all the observations into a master curve. In particular, the uncertainty in $r_1$ and $r_2$ is now 1.5%, which is quite acceptable for computations of the star's internal structure. Despite the low depth of Min I ($0.13^m$) and thanks to the primary eclipse being annular, we were also able to achieve reasonable accuracy in the linear limb-darkening coefficient of the primary, $u_1^{\rm obs} = 0.39 \pm 0.04$, which is close to the theoretically expected value $u_1^{\rm th} = 0.40$ for $\lambda_{\rm mean} \approx 5000$ Å [24].

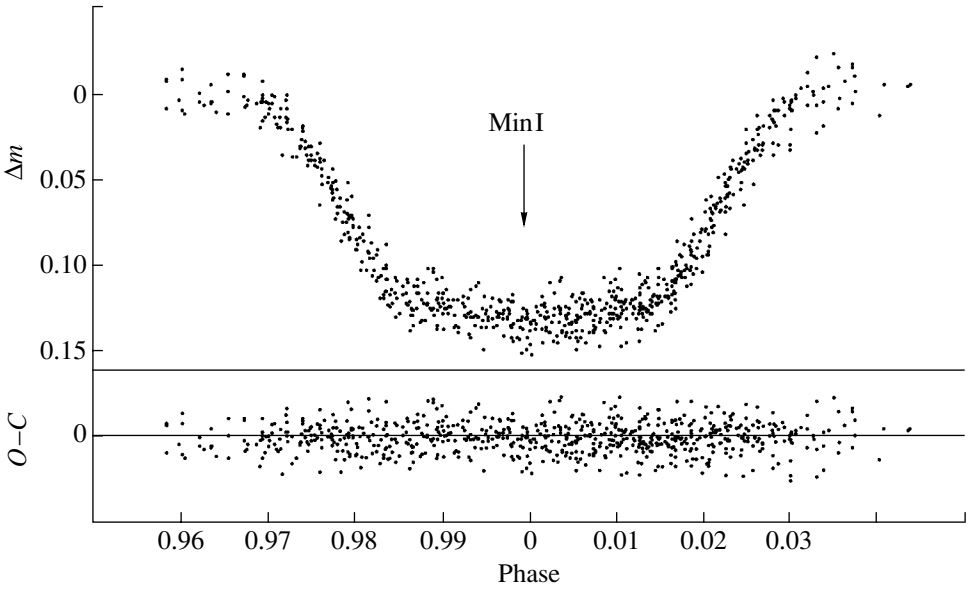


**Fig. 2.** Master light curve of AR Cas near the primary minimum (Min I). Along the bottom, we show the $O-C$ deviations of the observed points from the theoretical curve plotted for the photometric elements from Table 3.

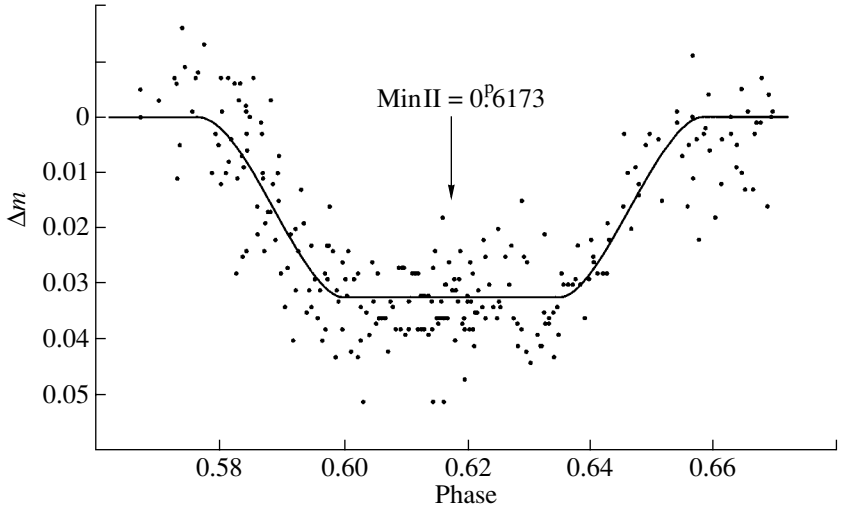


**Fig. 3.** Master light curve of AR Cas near Min II. The solid curve is the theoretical light curve.

According to the derived geometrical parameters of the system in Table 3, there is a total eclipse during the secondary minimum, and the depths of this minimum measured in different colors (Table 1) can be used to unambiguously determine the secondary's relative luminosities $L_2$ in each of the $WBVR$ bands, given in the second line of Table 4. However, these values characterize the brightness of the hemisphere facing the primary, which is higher due to the reflection effect. Using the obtained $L_2$ values and the linear reflection coefficients $A_1$ for the $WBVR$ bands collected in the first line of Table 1 (in the form of $2 \times A_1$), and applying known techniques for estimating the reflection effect [25], we can derive the relative luminosities of the secondary after correction for the reflection effect, $L_{2f}$, i.e., the luminosities of this component in the unilluminated hemisphere in the various bands. The values of $L_{2f}$ are collected in the third line of Table 4.

Now we must estimate the contribution of the visual companion B of the ADS 16795 system to the total observed brightness via the $L_3$ values for each of the $WBVR$ bands, proceeding from the only known parameter: $\Delta m = V_{\rm B} - V_{\rm AR\,Cas} = 4.4^m$. According to Tables 2 and 3, the contribution of the secondary to the total visual brightness of AR Cas is

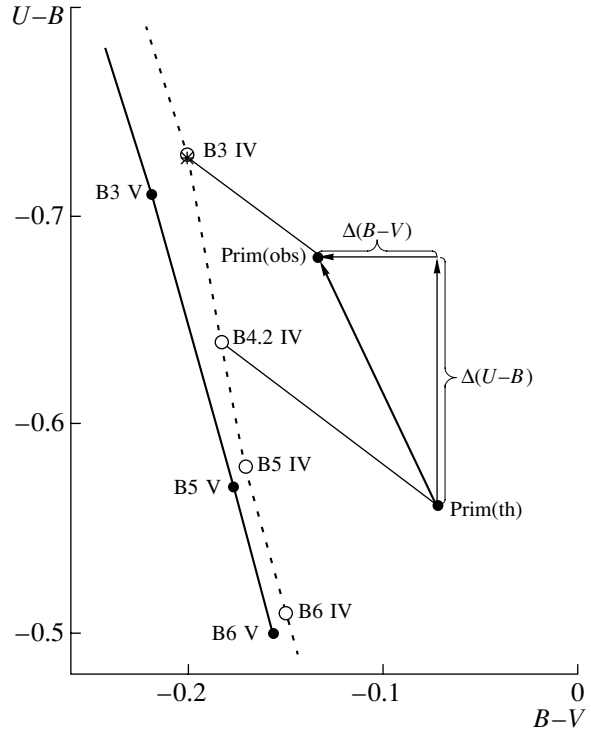


**Fig. 4.** Positions of the AR Cas primary in the two-color diagram: Prim(obs), corresponding to to the observed color indices, and Prim(th), corresponding to its spectral type (B4.2IV) and the value $E_{B-V=0.11^m}$.

about 3%, and the above parameter yields the magnitude difference between the visual companion B and the primary of AR Cas $\Delta V = V_{\rm B} - V_{\rm prim} = 4.37^m$. We show below that the primary's spectral type is B4.2IV and its absolute visual magnitude is $M_V = -1.63^m$. Based on the improbability of a chance close coincidence of the coordinates of the two fairly bright stars ($4.89^m$ and $9.29^m$; $\rho_{\rm A\text{-}B} = 1''.2$), we assume that these stars are also close in space, so that they are both the same distance from the Earth. Therefore, $M_V({\rm B}) = -1.63^m + 4.37^m = 2.74^m$. Below, we estimate the age of the components of AR Cas to be $60 \times 10^6$ years. Since AR Cas and its companion B are close to each other in space, it is very probable that their ages are also similar. According to the $M_V({\rm Sp})$ calibrations of [26] and modern evolutionary models [27], an object with $M_V = +2.74^m$ and an age of 60 million years should be a main-sequence star of spectral type A8V. Using the normal color indices of an A8V star [22] and adopting the same interstellar extinction for this star as for the components of the eclipsing system AR Cas, it is straightforward to derive the luminosities of the visual companion B relative to the combined luminosity $L_3 \equiv L({\rm A8V})$ of the entire AR Cas + B system. These luminosities are given in the fourth line of Table 4, while the fifth line gives the luminosities of the AR Cas primary normalized, as are $L_{2f}$ and $L_3$, using the condition $L_{1f} + L_{2f} + L_3 = 1$. Thus, in the case of a total eclipse, there is no need to plot complete light curves in all bands in order to derive the relative luminosities in all colors; it is sufficient to measure the depth of the total eclipse and take into account reflection effects. For this reason, we paid special attention to the measurements of the depth of the secondary minimum in the various colors when planning our observations.

The relative luminosities of the components from Table 4 and the absolute magnitudes of the AR Cas + B system as a whole from Table 1 can be used to calculate the magnitudes and color indices of each of the components. The results are given in Table 5.

## 4. ABSOLUTE PHYSICAL AND GEOMETRICAL PARAMETERS

We are now able to calculate the absolute physical and geometrical parameters of the eclipsing system AR Cas and its components using the photometric elements in Table 3, the components' relative luminosities and magnitudes in Tables 4 and 5, and the published spectroscopic results of [12, 13]. The resulting parameters are collected in Table 6.

Let us first consider the spectral type of the primary. We determined this to be B4.2IV, whereas the star appears in most spectroscopic catalogs as B3V. Judging from our value for the surface gravity, $\log g_1 = 3.84(2)$ (Table 6), there is no doubt that the star is a subgiant; i.e., its luminosity class is IV. The point marked Prim(obs) in Fig. 4 is the star's position in the ($U-B$, $B-V$) two-color diagram based on the observed color indices in Table 5. The normal color indices of unreddened stars of the corresponding spectral types are plotted in this diagram in accordance with the data of Straizys [22]. The initial position of the AR Cas primary appears to correspond to a slightly reddened B3IV star, with $E_{B-V} = 0.075^m$ and $A_V = 0.24^m$, which seems to confirm the spectroscopic estimates except for the luminosity class. However, if we adopt this spectral classification, this leads to contradictions with other observational data.

First of all, the star's trigonometric parallax based on Hipparcos data [28], $\pi = 5.67 \pm 0.56$ mas, leads to the distance $d = 176 \pm 17$ pc. However, if we apply the formula $\log d = 1 + 0.2(m_V - M_V - A_V)$, we obtain $d = 252 \pm 15$ pc for $M_V({\rm B3IV}) = -2.3^m \pm 0.1$ [26], which deviates from the Hipparcos value by more than $4\sigma$.

**Table 5.** Spectral types, magnitudes, and color indices for the components of the AR Cas + B system

| Star | Sp | $W$ | $(U)$ | $B$ | $V$ | $R$ | $W-B$ | $(U-B)$ | $B-V$ | $V-R$ |
|---|---|---|---|---|---|---|---|---|---|---|
| Primary | B4.2 IV | 3.994(10) | 4.13(2) | 4.813(5) | 4.946(4) | 5.035(5) | −0.819(11) | −0.68(2) | −0.133(5) | −0.089(6) |
| Secondary (unilluminated hemisphere) | A6 V | 9.18(5) | 9.21(5) | 9.03(3) | 8.74(3) | 8.48(2) | +0.15(5) | +0.18(5) | +0.29(4) | +0.26(3) |
| Secondary (illuminated hemisphere) | A4.5 V | 8.98(5) | 9.02(5) | 8.87(3) | 8.61(3) | 8.38(2) | +0.11(5) | +0.15(5) | +0.26(4) | +0.23(3) |
| Visual companion (component B) | A8V | 9.76(7) | 9.80(7) | 9.64(6) | 9.31(5) | 9.02(6) | +0.12 | +0.16 | +0.33 | +0.29 |

Second, the mass of the primary, $M_1 = 5.90 \pm 0.20 M_\odot$, does not correspond to a B3IV star. The standard Sp($M$) calibrations predict $M(\mathrm{B3IV}) = 7.6 M_\odot$ [26], considerably in excess of the observed mass.

Third, with $d = 252$ pc and $A_V = 0.24^m$, we obtain an interstellar extinction of $0.95^m$/kpc, or half the standard value, $2.0^m$/kpc [22], though AR Cas is situated in the Galactic plane ($b = -2.^\circ66$, $l = 112.^\circ47$). At the same time, for the nearby star we used as a comparison star, 1 Cas (B0.5IV, $V = 4.85^m$) [21], the two-color diagram gives $E_{B-V} = 0.26^m$ and $A_V = 0.84^m$. Based on $M_V(\mathrm{B0.5IV}) = -4.15^m \pm 0.10$ [26], it is easy to determine that, for this star, $d = 428 \pm 21$ pc and $A_V/d = 1.96^m$/kpc. Thus, we find no interstellar-extinction anomalies in the direction of the comparison star 1 Cas.

Considered together, these facts lead us to conclude that the color indices of the AR Cas primary are probably distorted by internal factors and do not directly reflect the spectral type or the $E_{B-V}$ and $A_V$ of the star. In order to determine the primary's absolute magnitude, luminosity, and effective temperature, we decided not to base our estimates on the observed color indices but instead to adopt a distance to the system of $d = 0.176$ kpc, in accordance with the Hipparcos data, and to use the standard value for the interstellar extinction [22]: $A_V = 2.0^m \times 0.176 = 0.35^m$; $E_{B-V} = 0.11^m$. In this case, applying the known relations

$$M_V = 5 + m_V - A_V - 5\log d,\ M_{\mathrm{bol}} = M_V + \mathrm{B.C.},$$
$$2.5\log(L/L_\odot) = M_{\mathrm{bol}}^\odot - M_{\mathrm{bol}},$$
$$\log(L/L_\odot) = 2\log(R/R_\odot) + 4\log(T_e/T_e^\odot),$$

we obtain

$$M_V = -1.63^m, \qquad M_{\mathrm{bol}} = -3.38^m,$$
$$\log L/L_\odot = 3.23, \qquad T_e = 16\,800\ \mathrm{K}.$$

These are the values presented in Table 6. The derived set of physical characteristics of the AR Cas primary ($M$, $R$, $M_V$, $M_{\mathrm{bol}}$, $T_e$) agrees most closely with the spectral type B4.2IV. Note that, when determining $M_{\mathrm{bol}}$, we used the value $\mathrm{BC} = -1.75^m$ for the bolometric correction, which differs by $-0.11^m$ from the mean value for this spectral type, $\mathrm{BC(B4.2IV)} = -1.64^m$ [29]. This decision was based on the observed ultraviolet excess, which is probably due to a metal deficiency in the star's atmosphere (see below).

The point in the two-color diagram (Fig. 4) labeled Prim(th) shows the position the star should occupy according to its spectral type (B4.2IV) and the above value $E_{B-V} = 0.11^m$. The line connecting the points Prim(th) and Prim(obs) can be considered the blanketing vector for metal-deficient stars [26]. Based on this vector, we derive $\Delta(U-B) = -0.12^m$, $\Delta(B-V) = -0.06^m$, and the vector's slope, $\Delta(U-B)/\Delta(B-V) = 2.0$, which provides a firm basis for interpreting this offset as being due to the

**Table 6.** Physical and geometrical parameters of AR Cas and its components

| Parameter | Primary | Secondary |
|---|---|---|
| Mass $M$ | $5.90 \pm 0.20 M_\odot$ | $1.86 \pm 0.06 M_\odot$ |
| Radius $R$ | $4.86 \pm 0.10 R_\odot$ | $1.59 \pm 0.03 R_\odot$ |
| Luminosity $\log(L/L_\odot)$ | $3.23 \pm 0.02$ | $1.02 \pm 0.02$ |
| Effective temperature $T_e$ | $16800 \pm 200$ K | $8250 \pm 100$ K |
| Spectral type Sp | B4.2IV | A6V |
| Gravity $\log g$ | $3.84 \pm 0.02$ | $4.30 \pm 0.02$ |
| Linear darkening coefficient $u$ | $0.39 \pm 0.04$ | – |
| Linear rotational velocity $v \sin i$ | $125 \pm 5\, km\, s^{-1}$ | – |
| $V$ | $4.946 \pm 0.004^m$ | $8.74 \pm 0.03^m$ |
| $W-B$ | $-0.82 \pm 0.01^m$ | $0.15 \pm 0.10^m$ |
| $B-V$ | $-0.133 \pm 0.005^m$ | $0.29 \pm 0.04^m$ |
| $V-R$ | $-0.089 \pm 0.006^m$ | $0.26 \pm 0.03^m$ |
| Absolute visual magnitude $M_V$ | $-1.63 \pm 0.06^m$ | $2.16 \pm 0.06^m$ |
| Bolometric correction BC | $-1.75 \pm 0.05^m$ | $-0.01 \pm 0.01^m$ |
| Absolute bolometric magnitude $M_{\rm bol}$ | $-3.38 \pm 0.07^m$ | $2.15 \pm 0.06^m$ |
| Apsidal parameter $\log k_2^{\rm obs}$ | $-2.41 \pm 0.08$ | – |
| Anomalistic orbital period $P_a$ | $6.066315 \pm 0.000004^{\rm d}$ | |
| Orbital semimajor axis $a$ | $27.7 \pm 0.3 R_\odot$ | |
| Eccentricity $e$ | $0.211 \pm 0.005$ | |
| Orbital inclination $i$ | $86.70 \pm 0.34°$ | |
| Distance to the system $d$ | $176 \pm 17\, pc$ | |
| Color excess $E_{B-V}$ | $0.11 \pm 0.01^m$ | |
| Interstellar extinction $A_V$ | $0.35 \pm 0.03^m$ | |
| The system's age $t$ | $(60 \pm 3) \times 10^6$ years | |
| Apsidal period $U_{\rm obs}$ | $1100 \pm 160$ years | |
| Trigonometric parallax $\pi$ | $0.00567 \pm 0.00056''$ | |

effect of metal-line blanketing. We return to this point in the Conclusions.

We derived the system's age using $M_1$ and $\log g_1$ and the stellar-evolution models of Claret and Gimenez [27]. Whenever possible, we estimated the uncertainties in each of the parameters in Table 6 taking into account the contributions from the uncertainties of all components used to determine that parameter.

**Table 7.** Mean heliocentric epochs of minima of AR Cas derived from our analysis of photoelectric observations published by various authors. The $O-C$ values are based on the linear ephemeris (2)

| No. | $JD_\odot$ | $E$ | $O-C$ | Author |
|---|---|---|---|---|
| | Min I | | | |
| 1 | 2422 580.4204(27) | −2178 | $-0.0035^d$ | Stebbins [2] |
| 2 | 2428 834.8130(24) | −1147 | −0.0007 | Gordon and Kron [6] |
| 3 | 2432 480.6813(30) | −546 | 0.0011 | Gordon and Kron [6] |
| 4 | 2432 498.889(11) | −543 | 0.0097 | Botsula and Kostylev [4] |
| 5 | 2435 052.8015(23) | −122 | −0.0040 | Huffer [37] |
| 6 | 2435 792.8948(29) | 0 | −0.0034 | Huffer and Collins [3] |
| 7 | 2436 890.9112(42) | 181 | 0.0066 | Gordon and Kron [6] |
| 8 | 2440 081.7902(33) | 707 | −0.0059 | Catalano and Rodono [5] |
| | Min II | | | |
| 1 | 2422 584.2354(85) | −2178 | $-0.0129^d$ | Stebbins [2] |
| 2 | 2432 502.661(15) | −543 | 0.0176 | Botsula and Kostylev [4] |
| 3 | 2436 894.643(11) | 181 | 0.0005 | Gordon and Kron [6] |
| 4 | 2440 085.5231(75) | 707 | 0.0083 | Catalano and Rodono [5] |
| 5 | 2446 746.2953(61) | 1805 | −0.0135 | Mossakovskaya [7] |

## 5. APSIDAL MOTION

An elliptical binary orbit will rotate in space due to the components' tidal and rotational distortions, as well as to general relativistic effects, at a rate that depends on the system's parameters [30, 31]. The main formulas describing this rotation are presented in modern notation in [32], and we will not reproduce them here. Our first goal is to determine the observed rate of the apsidal motion, $\dot\omega_{\rm obs}$, and then to calculate the parameter $k_2$ reflecting the radial density distribution based on $\dot\omega_{\rm obs}$ and the photometric and absolute elements derived above.

The apsidal motion in eclipsing systems is primarily manifest as a cyclic displacement of Min II with respect to phase $0.5P$ with the apsidal period $U_{\rm obs}$. This shift leads to a difference in the recurrence periods of the primary ($P_I$) and secondary ($P_{II}$) minimum, with the difference between them at any time ($\Delta P$) being described by the formula [32]

$$\frac{P_I - P_{II}}{P_a} = 4e\frac{P_a}{U_{\rm obs}} \times \left(\sin\omega - e^2\frac{1+3\sqrt{1-e^2}}{(1+\sqrt{1-e^2})^3}\sin 3\omega\right), \quad (1)$$

where, as above, the longitude of periastron is defined by the expression $\omega = \omega_0 + \dot\omega(\mathrm{JD} - \mathrm{JD}_0)$. To determine $P_I - P_{II}$, we analyzed all published photoelectric observations of AR Cas using the iterative differential-correction method of [23] in order to determine the epochs of Min I and Min II simultaneously with the photometric elements; the results are presented in Table 7. The least-squares solution for the data in this table leads to the ephemeris

$$\begin{aligned}\text{Min I} &= \text{JDH } 2435792.8982(24)^d \\ &+ 6.0663335(25)^d E, \\ \text{Min II} &= \text{JDH } 2435796.6429(70)^d \\ &+ 6.0662969(52)^d E.\end{aligned} \quad (2)$$

We can see that the periods of the primary and the secondary minima differ:

$$\Delta P = P_I - P_{II} = 0.0000366(57)^d = 3.16(47)^s,$$

with the secondary minimum occurring at phase $\varphi_{II} = 0.6173(12)^p$ for $\mathrm{JD}_0 = 2435792.8982^d$. Substituting this $\Delta P$ value and the $P_a$, $e$, and $\omega$ values from Table 6 into (1), we find

$$U_{\rm obs} = 1100 \pm 160 \text{ years};$$
$$\dot\omega_{\rm obs} = 0.327 \pm 0.049^\circ \text{ per year}.$$

As noted in Section 3, $\dot\omega_{\rm obs}$ was also determined simultaneously with the other photometric elements during the light-curve analysis. It is natural that these

two results should coincide. We can now use the known relations of [32] to compute the theoretically expected apsidal period, $U_{\rm th}$, and orbit rotation rate, $\dot{\omega}_{\rm th}$:

$$U_{\rm th} = 1070 \pm 76 \text{ years};$$

$$\dot{\omega}_{\rm th} = 0.336 \pm 0.021^\circ \text{ year}^{-1}.$$

We see that $\dot{\omega}_{\rm obs}$ and $\dot{\omega}_{\rm th}$ agree within their uncertainties. When computing $\dot{\omega}_{th}$, we adopted the theoretical apsidal motion parameters, $k_{2,1}^{\rm th}$ and $k_{2,2}^{\rm th}$, in accordance with the stellar-evolution models of Claret and Gimenez [27] and took the linear velocity of the axial rotation of the AR Cas primary, $v_1 \sin i$, to be $125 \pm 5$ km/s, in accordance with [12, 13]. The rotation rate of the secondary is not known from observations, and we assumed that the axial and orbital rotation are synchronized at periastron.

If we invert the problem and determine $k_{2,1}$ and $k_{2,2}$ from the observed $\dot{\omega}_{\rm obs}$, we obtain $\log k_{2,1}^{\rm obs} = -2.41 \pm 0.08$, which is very close to the theoretical value for $M_1 = 5.86 M_\odot$, $\log g_1 = 3.84$, and the chemical composition $X = 0.7$ and $Z = 0.02$, $\log k_2^{\rm th} = -2.39$ [27]. We cannot determine $k_{2,2}$ for the secondary: since its relative radius $r_2$ is small, the secondary's contribution to the apsidal motion is nearly two orders of magnitude (a factor of 64) lower than that of the primary.

## 6. CONCLUSIONS

Our joint analysis of published photometric, astrometric, and spectroscopic data along with our precise $WBVR$ measurements of AR Cas have enabled us to derive for the first time a self-consistent set of physical and geometrical parameters for this eclipsing binary and to determine the evolutionary status of its components (Table 6). We were also able to resolve the apsidal-motion problem: the apsidal parameter $k_{2,2}^{\rm obs}$ describing the internal structure of the primary we have found is in very good agreement with current models of stellar evolution.

It was somewhat unexpected to find an ultraviolet excess for the primary (B4.2IV, $M_1 = 5.9 M_\odot$), possibly due to a metal deficiency in the atmosphere of this star. Metal deficiencies are usually observed for stars of later spectral types (A–F–G). However, there exist metal-deficient stars with masses up to $6 M_\odot$—the so-called "blue stragglers" [26]—which are not adequately described in the framework of current theories of stellar formation and evolution. On the other hand, it was noted in [33] that a metal deficiency or excess in the atmosphere of a star should not be taken as a straightforward indicator of the star's age, and, in some cases, this may be a transient phenomenon reflecting diffusion processes when the opposing forces of gravity and light pressure have led to a separation of elements in the surface layers. One possible example of a star in which this mechanism operates is the eclipsing system RR Lyn, in which one component is a "metal-line" (Am) star and the other exhibits a metal deficiency [34–36]. Thus, in the case of AR Cas, whose age is only $60 \times 10^6$ years, the possible metal deficiency in the primary's atmosphere may not reflect the initial chemical composition of the star as a whole at the time of its formation. Spectroscopic studies of the chemical compositions of the components of AR Cas are needed before more definite conclusions can be drawn.

## ACKNOWLEDGMENTS

This study was supported by the State Science and Technology Program "Astronomy" (topic "Variability studies of unstable stars, including relativistic objects," project 40.022.1.1.1103).

## REFERENCES

1. B. J. Stebbins, Publ. Am. Astron. Soc. **4**, 115 (1919).
2. B. J. Stebbins, Astrophys. J. **54**, 81 (1921).
3. C. M. Huffer and G. W. Collins, Astrophys. J., Suppl. Ser. **7**, 351 (1962).
4. R. A. Botsula and K. V. Kostylev, Bull. Kazan. Astron. Obs. **35**, 34 (1960).
5. S. Catalano and M. Rodono, Astrophys. J. **76**, 557 (1971).
6. K. C. Gordon and G. E. Kron, Astrophys. Space Sci. **23**, 403 (1973).
7. L. V. Mossakovskaya, Astron. Astrophys. Trans. **3**, 163 (1992).
8. R. H. Baker, Publ. Allegheny Obs. **2**, 28 (1910).
9. W. J. Luyten, O. Struve, and W. W. Morgan, Publ. Yerkes Obs. **7**, 251 (1939).
10. R. M. Petrie, Astron. J. **51**, 22 (1944).
11. W. I. Gorza and J. F. Heard, Publ. David Dunlap Obs. **3**, 99 (1971).
12. M. Gaida and W. Seggewiss, Acta Astron. **31**, 231 (1981).
13. D. E. Holmgren, P. Hadrava, P. Harmanec, *et al.*, Astron. Astrophys. **345**, 855 (1999).
14. A. H. Batten, Publ. Astron. Soc. Pac. **72**, 349 (1960).
15. Z. Kopal, Adv. Astron. Astrophys. **3**, 89 (1965).
16. A. Slettebak and R. F. Howard, Astrophys. J. **121**, 102 (1955).
17. A. H. Batten, J. R. Astron. Soc. Can. **55**, 120 (1961).
18. Kh. F. Khaliullin, A. V. Mironov, and V. G. Moshkalev, Astrophys. Space Sci. **111**, 291 (1985).
19. V. G. Kornilov and A. V. Krylov, Astron. Zh. **67**, 173 (1990) [Sov. Astron. **34**, 90 (1990)].
20. V. G. Moshkalev and Kh. F. Khaliullin, Astron. Zh. **62**, 393 (1985) [Sov. Astron. **29**, 227 (1985)].
21. V. G. Kornilov, I. M. Volkov, A. I. Zakharov, *et al.*, Tr. Gos. Astron. Inst. Shternberga **LXIII**, 3-399 (1991).

22. V. Straizys, *Multicolor Stellar Photometry* [in Russian] (Mokslas, Vilnyus, 1977).
23. A. I. Khaliullina and Kh. F. Khaliullin, Astron. Zh. **61**, 393 (1984) [Sov. Astron. **28**, 228 (1984)].
24. J. Grygar, M. L. Cooper, and I. Jurkevich, Bull. Astron. Inst. Czechosl. **23**, 147 (1972).
25. D. Ya. Martynov, *Eclipsing Variables* [in Russian] (Nauka, Moscow, 1971).
26. V. Straizys, *Stars with Metal Deficiencies* [in Russian] (Mokslas, Vilnyus, 1982).
27. A. Claret and A. Gimenez, Astron. Astrophys., Suppl. Ser. **96**, 255 (1992).
28. M. A. C. Perryman, E. Hog, J. Kovalevsky, *et al.*, *The Hipparcos and Tycho Catalogues* (ESA SP-1200, 1997).
29. D. M. Popper, Ann. Rev. Astron. Astrophys. **18**, 115 (1980).
30. Z. Kopal, *Dynamics of Close Binary Systems* (Reidel, Dordrecht, 1978).
31. T. Levi-Civita, Am. J. Math. **59**, 225 (1937).
32. Kh. F. Khaliullin, in *Binary Stars* [in Russian] (Kosmoinform, Moscow, 1997), p. 139.
33. L. S. Lyubimkov, *The Chemical Composition of Stars: Method and Analysis Results* [in Russian] (Astroprint, Odessa, 1995).
34. L. S. Lyubimkov and T. M. Rachkovskaya, Astron. Zh. **72**, 64 (1995) [Astron. Rep. **39**, 56 (1995)].
35. L. S. Lyubimkov and T. M. Rachkovskaya, Astron. Zh. **72**, 72 (1995) [Astron. Rep. **39**, 63 (1995)].
36. Kh. F. Khaliullin, A. I. Khaliullina, and A. V. Krylov, Astron. Zh. **78**, 1014 (2001) [Astron. Rep. **45**, 888 (2001)].
37. C. M. Huffer, private communication, 1961.

*Translated by N. Samus'*

*Astronomy Reports, Vol. 47, No. 7, 2003, pp. 562–572. Translated from Astronomicheskiĭ Zhurnal, Vol. 80, No. 7, 2003, pp. 613–623.*


# Butterfly Diagram for Starspots on LQ Hya

**M. A. Livshits[1], I. Yu. Alekseev[2], and M. M. Katsova[3]**

[1] *Institute of Terrestrial Magnetism, Ionosphere, and Radiowave Propagation, Russian Academy of Sciences, Troitsk, Moscow oblast, 142190 Russia*

[2] *Crimean Astrophysical Observatory, National Academy of Sciences of Ukraine, Nauchnyi, Crimea, 334413 Ukraine*

[3] *Sternberg Astronomical Institute, Universitetskiĭ pr. 13, Moscow, 119992 Russia*

Received December 30, 2002; in final form, January 10, 2003

**Abstract**—Information on the latitude distribution of starspots and changes in this distribution from year to year is very important for our understanding of the nature of stellar activity and for developing dynamo theory. The concept of butterfly diagrams is introduced for highly spotted stars of late spectral types, by analogy to the Maunder diagrams for the Sun. Our approach is based on the zonal spottedness models constructed by Alekseev and Gershberg. A detailed analysis is given for the single active star LQ Hya, and a comparison is made to similar analyses for several stars with two well-separated spot belts—EK Dra, VY Ari, V775 Her, and V833 Tau. The lower boundary of the butterfly diagram drifts toward the equator during the activity-rise phase, i.e., during years when the relative spotted area increases. This effect is clearly expressed for LQ Hya and other stars whose orientation enables observation of both hemispheres and virtually vanishes for V833 Tau, which is viewed nearly pole-on. The upper boundary of the diagram is virtually unchanged for all the considered spotted stars except V775 Her, for which it moves toward the pole. The drift rate of the lower boundary is $-1$ to $-2$ deg/yr, a factor of two to three smaller in magnitude than the corresponding solar value. Our analysis provides an independent confirmation of the occurrence of high-latitude spots on stars that are younger than the Sun and whose activity is high but less regular than the solar activity; it also enables the identification of the starting times of stellar cycles.


## 1. INTRODUCTION

Recent advances in solar–stellar physics have revealed a number of regularities, among which the dependence of the X-ray luminosity of late-type stars on their axial-rotation rate is most important. This provided weighty evidence for the realization and widespread occurrence of dynamo processes generating and amplifying magnetic fields in such stars.

Numerous studies have been devoted to the development of dynamo theory, primarily with regard to the Sun, for which not only solar surface observations but also recent helioseismological data can now be used to try to understand and develop theoretical concepts. We note here only one important result. The latitude drift of tracers of activity (sunspots, flocculi, filaments, etc.) in the course of the cycle can be satisfactorily explained using a dynamo theory that takes into account the helioseismologically determined radial and latitude dependences of the angular rotation rate in the solar convection zone.

When applied not only to the Sun but also to late-type stars, such investigations are of interest for two reasons. First, it is now becoming possible to compare theoretical and observational results not only for one star—the Sun—but also for dozens of stars with different axial-rotation rates, convection-zone thicknesses, etc. Second, apart from the Sun, only about ten G–K stars exhibit well-defined solar-type cycles. Such cycles are most likely a special, asymptotic realization of the dynamo process. The conditions for the development of this regime and differences between processes on the Sun and on more active (normally, younger) stars are currently very topical issues.

We study here the distribution of spots over a star's surface and changes in their positions from year to year. Our approach was first implemented in [1], which presents a new representation of the zonal spot-distribution models for active late-type stars developed by Alekseev and Gershberg [2–4]. We consider here the single star LQ Hya, for which reliable photometric observations are available and the latitude distribution of spots can be determined most accurately. This dK1 star is characterized by a fairly high level of activity, consistent with its fast rotation (with a period of 1.601136 days). Its X-ray luminosity is $10^{29}$–$10^{30}$ erg/s, which exceeds the so-

1063-7729/03/4707-0562$24.00 

lar value by three orders of magnitude. The activity of this star, which reached the main sequence only very recently [5], is not strictly cyclic, and there is evidence for optical variations with periods of about 5 and 15 yr. In contrast to the Sun, with its well-defined cycle, this star exhibits much higher but less regular activity.

Doppler imaging [6–9] and analyses based on inversion techniques [10, 11] have been carried out for this star in a number of studies. The parameters $v \sin i = 25 \pm 2$ km/s and $R_* = 0.79\ R_\odot$ reported for LQ Hya [12] yield the estimate $i \approx 70^\circ$ for the angle between the rotational axis and the line of sight.

We briefly compare known techniques for studying surface inhomogeneities and analyze the distribution of spots over the stellar surface and variations in the latitudes of the spot zones. We also compare our results for LQ Hya with those obtained previously for other active late-type stars [1].

## 2. TECHNIQUES FOR MAPPING SURFACE INHOMOGENEITIES

We study here the latitude distribution of spots over the surface of a star when the total spotted area is large (exceeding the area of sunspots at solar-activity maxima by a factor of 100 or more). The Doppler imaging of stellar surfaces is a widely known method that is especially effective when applied to the components of eclipsing binaries. The main ideas behind this technique were presented, e.g., by Rodonó, Piskunov, Strassmeier, and Berdyugina at IAU Symposium 176 in Vienna in 1995 [13]. These studies showed that, in some cases, activity can extend to high latitudes and can remain concentrated near certain longitudes for many years; moreover, the first estimates of stellar differential rotation were obtained (see [14, 15] and references therein).

However, such techniques also have disadvantages, which are most prominent in analyses of highly spotted stars. First, the corresponding models are essentially hierarchical: the parameters of the spot distribution are derived from the observed light curve assuming the existence of some hierarchy of spots with regard to their effects on the integrated luminosity of the star. In such models, it is convenient to place the first large spot near one of the poles, then add the second and any additional spots. The rapid growth in the number of parameters—the area, location, and contrast of each spot—makes it necessary to restrict the modeling to one, two, or, very rarely, three spots.

Arguments against the existence of polar spots are clearly formulated by Birn ([13], p. 299); a detailed discussion of other drawbacks of the hierarchical models is given in [16]. Further developments in this area have made it possible to remove a number of sources of errors—in particular, to reduce the effects of the polar spot and better identify active longitudes. Obviously, in some cases, the characteristic features of the brightness variations with the axial-rotation phases of active late-type stars are related to a concentration of spots near some fixed longitude. However, it would be incorrect to claim that the rotational brightness modulation is completely determined by the longitude distribution of the spots. The example of the Sun strongly contradicts this assertion: the sunspot latitudes drift toward the equator from year to year, while the active longitudes are difficult to distinguish even in the declining phase of a cycle, when their effect is most pronounced.

One fundamental difficulty in mapping the surface inhomogeneities is the impossibility of unambiguously reconstructing the pattern of the spot distribution. Currently available techniques strongly overstate the effect of active longitudes, especially for systems outside of eclipses. For example, Berdyugina *et al.* [11], analyzing photometric observations, claim that "Since a light curve represents a one-dimensional time series, the resulting stellar image contains information on the spot distribution only in one direction, in longitudes, while spot extents and locations in latitudes remain uncertain." This statement is not entirely correct for even one star, since such a one-dimensional time series contains information on the longitude spot distribution in both hemispheres; if the spot latitudes vary from season to season, this should be reflected by the light curves. If we analyze data for several stars with various orientations of their rotational axes relative to the Earth, comparisons of the corresponding light curves can provide information about the latitude distribution of the spots. The latitude dependence is more pronounced if we consider cases in which there are numerous spots rather than only one spot on the surface of the observed star.

Only one alternative approach is known: joint analysis of data on the rotational modulation and long-term variability of the optical emission to elucidate the latitude distribution of the spotted zone. We are referring here to the zonal spot models developed by Alekseev and Gershberg [2–4] several years ago. It is important that they completely abandoned hierarchical models, which makes their approach attractive for situations with fairly high surface spot densities.

It was assumed in [2–4] that the spots are localized in two belts symmetric with respect to the equator and bounded by two parallels separated by some distance $\Delta\phi$, with the lower boundaries of these belts at latitudes of $\pm\phi_0$. To take into account the longitude nonuniformity of the spot distribution, it was assumed that the width of the belt has a maximum at a certain longitude and decreases to $f_{\min}$ on the opposite side of the star (Fig. 1). The last parameter of the model is the

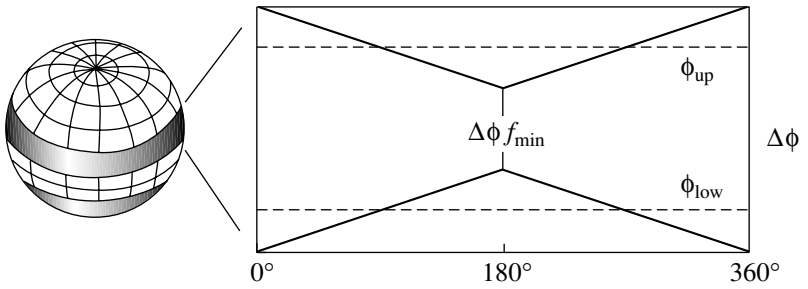


**Fig. 1.** Schematic representation of the spot-belt boundaries. Shown on the right is a fragment of a synoptic map for one spot belt; the dashed lines are the upper and lower boundaries of the butterfly diagram for the spot distribution.

spot contrast relative to the unperturbed photosphere, which was derived from $BVRI$ photometry together with the other parameters.

The zonal models can be used to calculate the maximum and minimum relative spots areas for a given observation epoch, which encompasses several rotational periods of the star. The ratio of the total spotted area to the entire surface area of the star (the relative spotted area) $S_{sp}$ is calculated as the sum of the maximum and the minimum values for the given epoch. Note that this parameter is virtually independent of the technique used to map the surface inhomogeneities.

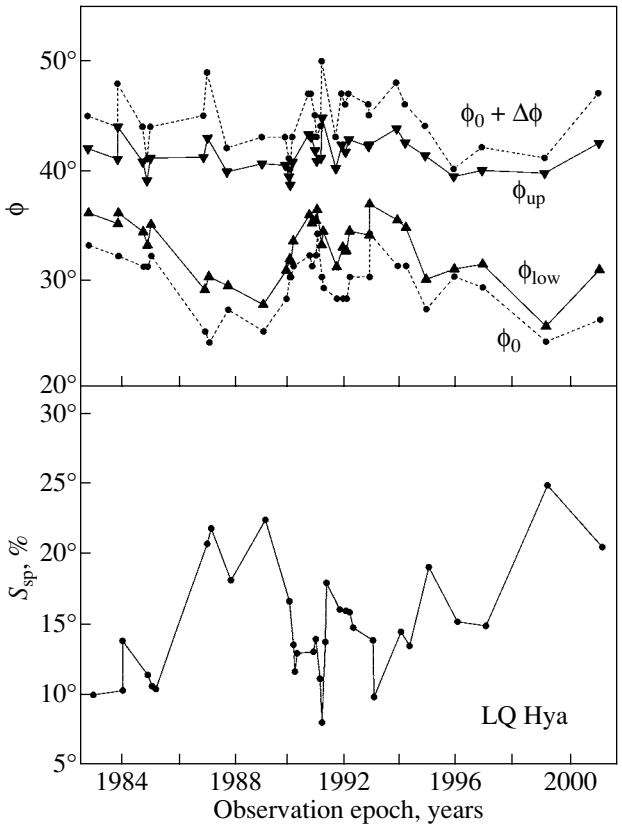


**Fig. 2.** Top: time variations in the latitudes of spot appearance (dashed lines) and in the positions of the upper and lower boundaries of the butterfly diagram (solid lines). Bottom: variations in the relative spotted area on LQ Hya.

Thus, the zonal model for a given observation epoch is described by four independent parameters—$\phi_0$, $\Delta\phi$, $f_{min}$, and the spot contrast $\beta$. The formalism developed by Dorren [17] can be applied to find the best agreement between the observed and computed light curves. If the angle $i$ between the rotational axis and the line of sight is 90°, the integrals in the solution can be calculated analytically, and the factors depending on the longitude and latitude separate in the integrals. For other inclination angles, these integrals must be computed numerically.

In the context of the problem under discussion, it is useful to compare briefly the two approaches to analyzing the surface inhomogeneities of late-type stars. In Doppler-imaging hierarchical models and similar techniques, the rotational modulation of the optical radiation is associated with the main spot, and it is the longitude of this spot that is the most important parameter of the model, along with its relative area. Therefore, the use of such approaches proved to be highly successful in studies of the effect of active longitudes, and it may even be that the influence of the longitude dependence was overstated in some cases. Note, however, that the most attention in this approach is given to careful solution of the corresponding inverse problem.

On the other hand, underlying the zonal models is the assumption that there are two spotted zones well separated in latitude. In essence, the rotational modulation data are analyzed in parallel with the data on long-term luminosity variations. This yields some information about the latitudes of the spotted regions. However, currently available methods of solving the inverse problem allow only an approximate treatment of the spot distribution in longitude. Instead of studying the latitude dependence for only one star, it is better to study such dependences for several stars with similar activity but different inclinations of their

**Table 1.** Active late-type stars studied and their variability

| Star | Spectrum | $P$, days | $i$ | $\Delta V$ | $\Delta\langle V\rangle$ | $\alpha$ | Remark |
|---|---|---|---|---|---|---|---|
| LQ Hya | dK1e | 1.60 | 70° | $0^m.19$ | $0^m.09$ | 2.11 | single |
| EK Dra | dG1e | 2.7 | 60 | 0.12 | 0.10 | 1.20 | single? |
| VY Ari | dG9e | 16.4 | 60 | 0.31 | 0.27 | 1.15 | SB1 |
| V775 Her | dK0e | 3.8 | 80 | 0.15 | 0.43 | 0.35 | SB1 |
| V833 Tau | dK5e | 1.85 | 20 | 0.08 | 0.31 | 0.25 | SB1 |
| BY Dra | dK6e | 3.8 | 70 | 0.20 | 0.38 | 0.53 | SB2 |
| EV Lac | dM4.5e | 4.4 | 90 | 0.14 | 0.25 | 0.56 | single |

Here, $P$ is the period of axial rotation of the star, $i$ is the angle between the rotational axis and the line of sight adopted for the zonal models, $\Delta V$ and $\Delta\langle V\rangle$ are the amplitudes of the rotational and long-term variabilities, and $\alpha$ is the ratio of these amplitudes; the last column contains information on binaries.

rotational axes to the line of sight (see Section 5). In this case, the spots on both stellar hemispheres contribute to the variability of the total brightness, and the effect of the spot latitudes is manifest along with that of the spot concentration near certain longitudes. The advantages of zonal models are fairly clear when the spots cover a significant fraction of the stellar surface. A number of arguments—first and foremost, the magnetic-field strengths in spots—indicate that the parameters of starspots and sunspots are similar, but that the spots on active late-type stars are much more numerous than on the Sun. Therefore, the zonal-model approach is preferable over the use of hierarchical models for highly spotted late-type stars.

Zonal models have been constructed for 25 late-type stars at about 350 epochs. The coolest stars have northern and southern belts merging into one equatorial belt, while the solutions for some G and K stars correspond to two well-separated belts during most epochs for which model calculations have been carried out. We present below an analysis based on a new representation of the results obtained from zonal spottedness models for LQ Hya and several other similar stars with two well-separated spot belts. Some parameters of these stars and their variability are presented in Table 1. For comparison, data for two flare stars are also included in this table.

## 3. BUTTERFLY DIAGRAM FOR STARSPOTS ON LQ Hya

In principle, the parameters $\phi_0$ and $\Delta\phi$ already give some idea of the latitude distribution of spots over the surfaces of active late-type stars. The time variations of $\phi_0$ and $\Delta\phi$ for LQ Hya during 33 observation epochs are shown in Fig. 2, in accordance with the zonal model described in [18]. Figure 2 corresponds only to the northern hemisphere of the star. Such a latitude–time dependence is a very crude analog of the Maunder butterflies well known in solar physics. However, one difference is that any sunspot can be observed individually, whereas only averaged characteristics can be analyzed for starspots. Moreover, the effect of active longitudes is not taken into account in such a representation of the latitude range occupied by the spotted region.

Several techniques used to construct such diagrams for the Sun are described, for example, in the monograph of de Jager [19]. Even if we consider diagrams based on analyses of sunspot areas rather than their number at a given latitude (as has usually been done), the Maunder diagrams differ from the time-variation diagrams for the latitude boundaries of the spottedness ($\phi_0$ and $\phi_0 + \Delta\phi$) in that each sunspot is recorded irrespective of its longitude, while the latitudes of the spottedness boundaries on a star correspond to a model representation that includes some form of dependence for the concentration of activity near certain longitudes.

Setting aside this difference for the moment, let us analyze the relationship between the boundaries of the spotted belts and the variation in the relative spotted area. First, we can see from Fig. 2 that the spot zone on LQ Hya is situated at fairly high latitudes, in agreement with the results of Doppler imaging [7]. Second, the most distinctive feature is that the displacement of a spot zone to lower latitudes (a decrease in $\phi_0$) corresponds to an increase in the relative spot area $S_{\rm sp}$. The anticorrelation of these quantities is fairly high for all rise phases of activity; e.g., the correlation coefficient $r(\phi_0, S_{\rm sp}) = -0.98$ for

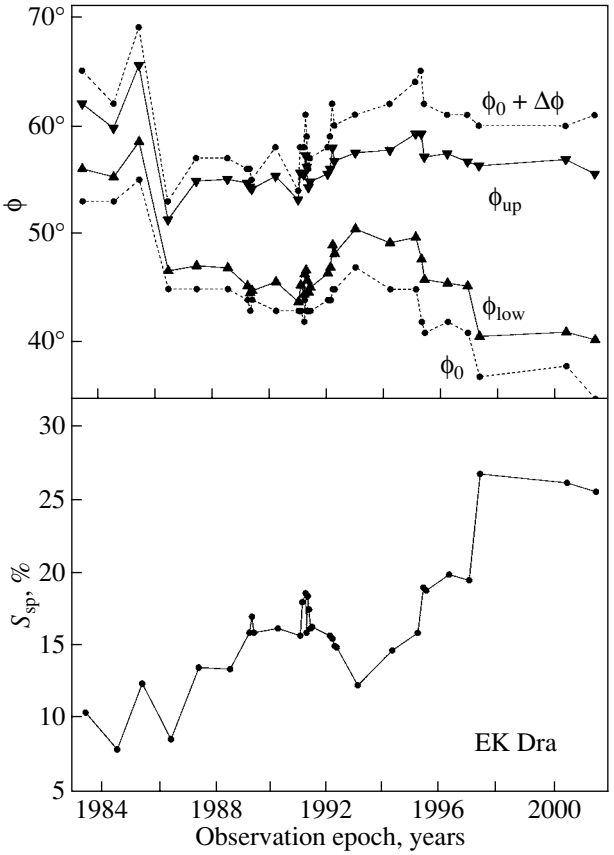


**Fig. 3.** Same as Fig. 2 for EK Dra.

1993–2000, although it is lower for the entire 20-yr observation interval (33 points): $r(\phi_0, S_{\rm sp}) = -0.95$. By analogy with the Sun, it seems reasonable to suggest that this newly discovered fact is related to an equatorward drift of the spots, as is clearly manifest in Maunder diagrams. However, the stellar observations differ from solar observations, and the effect of active longitudes may be more pronounced in the former case. These problems are the subject of the analysis below.

It makes sense to construct a new definition of butterfly diagrams for stars. The parameter $\Delta\phi$ in the zonal models is the maximum spot-belt width, which corresponds to the minimum brightness of the star; this time is adopted as the zero phase of the axial rotation. The center of the spot belt is located at the latitude $\bar{\phi} = \phi_0 + \Delta\phi/2$. The spot-belt width varies linearly from $\Delta\phi$ to $\Delta\phi \times f_{\rm min}$ (the latter value is reached on the opposite side of the star, at phase 0.5); see Fig. 1. During a given epoch, such a spot belt covers a fraction $(1 + f_{\rm min})/2$ of the entire region bounded by the latitudes $\phi_0$ and $\phi_0 + \Delta\phi$ (here and below, we present latitudes for the northern hemisphere of the star). Upon averaging this fraction over longitude, we obtain the mean width of the "effective" spot belt

$$w_b = \frac{\Delta\phi(1 + f_{\rm min})}{2}.$$

The upper and the lower boundary of this effective belt are given by the expression

$$\left\{ \begin{array}{c} \phi_{\rm up} \\ \phi_{\rm low} \end{array} \right\} = (\phi_0 + \frac{\Delta\phi}{2}) \pm \frac{\Delta\phi}{4}(1 + f_{\rm min}),$$

where the plus sign refers to the upper boundary of the butterfly diagram, and the minus sign, to the lower boundary.

Thus, we propose to adopt the latitude–time distribution for the majority of the spotted area as a butterfly diagram for stars. In other words, while any spot can be individually observed on the Sun, for stars, we consider only the spotted region that makes the largest contribution to the spottedness area on the stellar surface. Note that the case considered above in this section corresponds to $f_{\rm min} = 1$.

The behavior of the upper ($\phi_{\rm up}$) and lower ($\phi_{\rm low}$) boundaries of the butterfly diagram for LQ Hya is also shown in Fig. 2. The difference from the above variations of $\phi_0$ and $\phi_0 + \Delta\phi$ is essentially due to the fact that we consider here the longitude-averaged boundaries of the spot belt, shown in Fig. 1 by the dashed lines. In essence, such changes in the diagram boundaries are associated with the approximate elimination of the effect of active longitudes.

The relative spotted area $S_{\rm sp}$ coincides numerically with the width of the effective spot belt $\Delta w_b$ in radians (here, the area of the two spot belts is divided by $4\pi R_*^2$). Let us compare this value with the temporal behavior of the butterfly-diagram boundaries. The conclusion that the spot belt drifts toward the equator during the rise phase remains valid. The correlation between $S_{\rm sp}$ and the position of the lower boundary of the diagram $\phi_{\rm low}$ is high for various intervals during the rise phases of activity; for example, the correlation coefficient for 1983–1989 is $-0.90$. During the same years, the equatorward drift of the spots is quite pronounced (see Fig. 2 and the corresponding section below).

Although the variations in $\phi_0 + \Delta\phi$ were significant over almost 20 yr, after taking into account the effect of active longitudes, the position of the upper boundary of the diagram $\phi_{\rm up}$ remains virtually unchanged. We note only a small decrease in $\phi_{\rm up}$ by no more than a few degrees in 1993–1995, during the rise phase of one of the five-year quasi-periods of the stellar activity. A simultaneous decrease in the latitude of the diagram boundaries is typical of the rise phase of the solar cycle.

## 4. COMPARISON OF THE BUTTERFLY DIAGRAMS FOR STARSPOTS AND SUNSPOTS

Revealing the latitude dependence of the spot distribution is a very difficult task, and it is expedient to consider not one star but as many stars with comparable activity levels as possible. The effect of the longitude and latitude dependences should be different for stars with widely differing inclinations of their rotational axes to the lines of sight. If the star is viewed nearly pole-on (at small inclination angles $i$), the longitude effect is not distorted, while the longitude and latitude dependences compete with each other when $i$ is large. Clearer manifestations of the latitude dependence are expected when the relative spotted area is a factor of some tens higher than on the Sun but does not exceed $S_{sp} \approx 40\%$.

The tables presented by Alekseev [13] can be used to construct butterfly diagrams for some stars that have been observed for ten years or longer. Such an analysis was carried out for six stars in [1]; here, we include observations obtained in 2000–2001. The required parameters of the stars are presented in Table 1. Let us first consider G–K stars with large angles $i$, and then V833 Tau with $i \approx 20°$; we will also briefly describe the butterfly diagrams of flare stars.

We first compare our results for LQ Hya with data for a star that is definitely characterized by high-latitude activity: the spotted star EK Dra (dG1), which has been intensely studied during the past decade. Its age does not exceed $10^8$ yr, as is also the case for LQ Hya. The variability of EK Dra was analyzed in detail as part of the HK project, and EK Dra had the highest chromospheric activity among the stars investigated. The activity of the outer atmosphere of EK Dra is somewhat higher than that of LQ Hya, despite its lower rotation rate (Table 1).

The butterfly diagram for EK Dra is shown in Fig. 3 in a form similar to that for LQ Hya in Fig. 2. Compared to [1], we also include here recent observations made up to 2001. We can see that a period of high spotness, observed on this star for the first time, has already lasted for about four years, which only slightly exceeds the duration of the activity maximum for the stars considered (VY Ari, V775 Her), with characteristic time scales for the quasi-cyclic brightness variations exceeding ten years.

The zonal model for EK Dra is based on the calculations of [18]. The method used reveals high-latitude spots on this star, in overall agreement with the results of Doppler imaging. The spot latitude range for EK Dra is located, on average, 10°–15° higher than for LQ Hya, with the relative spotted areas averaged over the 20-yr observation period being similar.

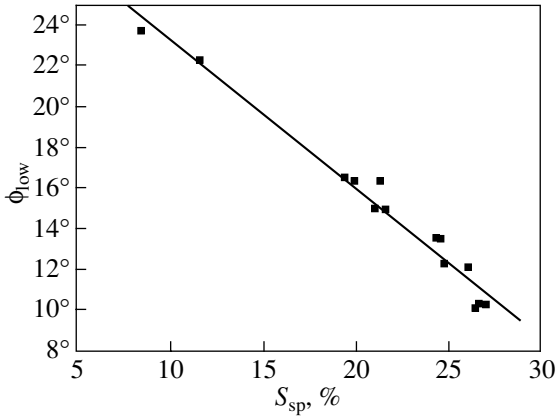


**Fig. 4.** Latitude of the lower boundary of the butterfly diagram for VY Ari during various observation epochs as a function of the relative spotted area (points) and the corresponding linear regression fit (solid line).

The butterfly diagrams for these two stars share a number of traits. The growth of the spottedness on EK Dra during 1986–1990 and 1995–2000 was accompanied by some drift of the spotted zone toward lower latitudes. This drift was especially strong in recent years. Note, however, that the appreciable decrease in the spot-belt latitude between 1985.5 and 1986.5 was not accompanied by a growth in the spotness. The anticorrelation between the spotted-zone latitude and the relative spotted area could be disrupted by several factors, such as anomalously small widths of the spot zone and the large time intervals between observations in the early stages of this study.

Taking into account the effect of active longitudes leads to a similar change in the diagrams for these stars. Generally, the behavior of the lower boundary of the diagram for EK Dra changes little, while the poleward drift of the upper boundary becomes considerably weaker. However, whereas there is virtually no drift of the upper boundary for LQ Hya, the weak poleward drift of the spotted zone on EK Dra persists over 12–15 yr.

The main differences in the butterfly diagrams are most likely due to the characteristic variability of these two active stars. Long-term brightness variations of EK Dra are most pronounced. We can see from Fig. 3 that, on average, the spotted area continuously increases over 13 yr and, accordingly, the entire duration of the "cycle" (if there is a cycle for this star) is even longer. Variations with shorter periods (5–7 yr) are not clearly defined.

The brightness of EK Dra varies very smoothly on a characteristic time scale of more than ten years. In contrast, while the brightness variations of LQ Hya have a period close to 15 yr, they also exhibit fluctuations on characteristic time scales of several years.

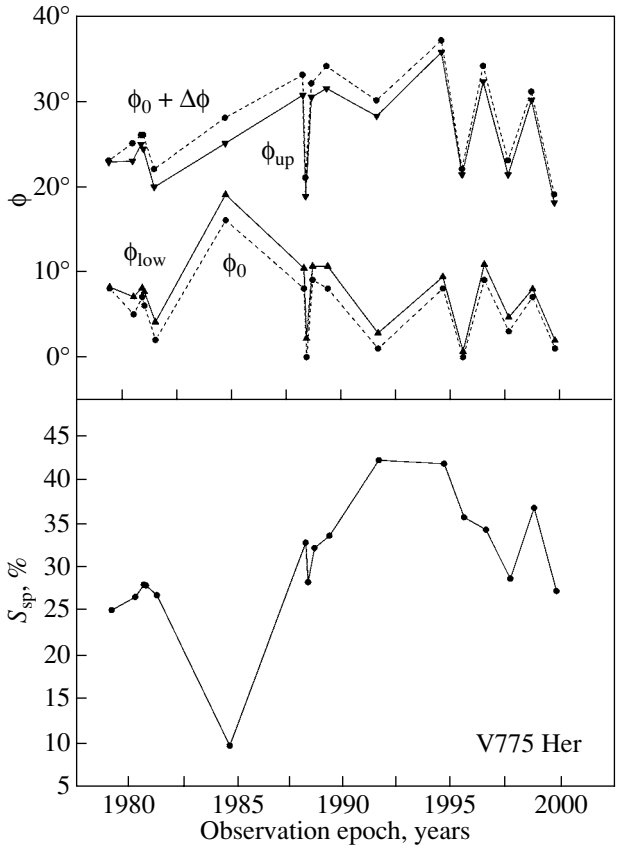


**Fig. 5.** Same as Fig. 2 for V775 Her.

This follows both from Fig. 2 and the study of Berdyugina et al. [11], who reported periods of 5.2, 7.7, and 15 yr. The spot drifts on LQ Hya during the rise phases of activity can be traced with certainty for at least two five-year cycles. The differences between the behavior of the activity of LQ Hya and EK Dra may provide a source of information on mechanisms for the formation of cyclic variations.

A similar analysis was done for three other stars—VY Ari, V775 Her, and V833 Tau, whose activity levels are similar to that of LQ Hya. These are binaries but with widely separated components, so that their binary structure does not seem to affect the activity level and the associated physical processes. Note that the relatively slow rotation of VY Ari (Table 1) does not lead to a lower activity level compared to the other stars considered. The viewing conditions for VY Ari and V775 Her are nearly the same as for LQ Hya and EK Dra, while V 833 Tau is viewed almost pole-on.

**Table 2.** Rates of the latitude drift of starspots

| Star | $D$, deg/yr | $\Delta t$, years |
|---|---|---|
| LQ Hya | −1.58 | 1983–1989 |
| LQ Hya | −1.71 | 1993–1999 |
| LQ Hya | −0.88 | 1991–1999 |
| EK Dra | −1.22 | 1993–1997 |
| VY Ari | −1.3 | 1984–1994 |
| V775 Her | −2.2 | 1984–1992 |

VY Ari and V775 Her are highly spotted, with $S_{sp}$ reaching 40% or more; however, in contrast to the examples above, the spots are located at nearly the same latitudes as on the Sun, no higher than 30°–40°. Active longitudes are fairly pronounced on VY Ari. If this effect is taken into account, the relationship between the latitude and $S_{sp}$ remains clearly expressed for the lower boundary of the butterfly diagram during the rise phase of activity. This dependence is shown in Fig. 4 for 14 analyzed epochs of VY Ari observations in 1984–1995. The correlation coefficient is very high (−0.987). However, near the activity maximum (when the lower boundary approaches the equator during some epochs, i.e., $\phi_0$ vanishes), this regular dependence is disrupted. A similar disruption of the $S_{sp}$–$\phi_{low}$ relationship occurred on V775 Her after 1995, when the hypothetical activity cycle was already in the decline phase (Fig. 5). The durations of the cycles for VY Ari and V775 Her are estimated to be 14–15 yr, and these variations can be traced in the butterfly diagram even better than directly in the long-term brightness variations.

The activity of VY Ari grew slowly from 1986 to 1995. The spotted area increased on V775 Her much more rapidly, manifest as an accelerated drift of the spots toward the equator. The effect of active longitudes was weakly pronounced in this case. In contrast to the constant position of the upper boundary of the diagram for VY Ari in 1983–1995, the butterfly diagram for V775 Her (Fig. 5) exhibits a poleward drift of its upper boundary over about 14 yr. Sunspots do not demonstrate such movement.

To conclude this section, we note another piece of evidence that latitude dependence plays an important role in the integrated brightness variations. The variability of active late-type stars is influenced by both the longitude and latitude distributions of the spots. There is reason to believe that, under identical viewing conditions, the longitude distribution affects the rotational brightness modulation more strongly. In this case, the degree of rotational modulation and complexity of the light curve can serve as indicators of the presence of active longitudes. This means that the effect of spot concentrations near certain fixed longitudes can tentatively be characterized by the ratio of the maximum amplitude of the rotational modulation to the amplitude of the long-term variability, $\alpha = \Delta V/\Delta\langle V\rangle$. We present this quantity $\alpha$ in our

Table 1, based on the data in Table 1 of [20]. In our analysis, we should consider the fact that the largest-amplitude long-term brightness variations during the entire observation period, 1900–2002, were recorded for V775 Her and V833 Tau. In these cases, the main characteristic time scale for the brightness variations ranged from 50 to 100 yr.

For all the stars considered except V833 Tau, the viewing conditions can be taken to be the same. Among these stars, LQ Hya has the largest $\alpha$, while this quantity is about a factor of two smaller for EK Dra and VY Ari and a factor of six smaller for V775 Her. This may provide evidence for gradual decreases in the contribution of active longitudes to the brightness variability of these stars. This view is consistent with previous analyses of the latitude dependences of the spotted areas [1], which revealed the most pronounced contribution of active longitudes in the case of VY Ari (epochs 1987.9 and 1988.1), while, in contrast, this contribution for V775 Her was relatively small and did not interfere with the detection of both the equatorward and poleward drifts of the spots. On the other hand, the effect of active longitudes on LQ Hya is quite pronounced during some epochs [11].

The case of V833 Tau, which is viewed nearly pole-on, should be considered separately. Here, the small $\alpha$ is simply related to the weak effect of the mid-latitude surface inhomogeneities on the integrated luminosity of the star. Thus, even the most clearly expressed effect—the decrease in the latitude of the lower boundary of the spot belt during the rise phase of spottedness—is strongly reduced [1]. However, in the case of such small angles $i$, the influence on the brightness variations of the spot concentration near active longitudes also becomes weaker, consistent with the fact that V833 Tau has the smallest amplitude of the rotational brightness modulation among the stars we have considered. Note, however, that the amplitude of long-term variations of V833 Tau was high in the 20th entury.

The butterfly diagrams for flare stars with one spotted belt differ from those for the stars considered above [1]. They mainly reflect the fact that the relative spotted area is closely related to the belt width. When $\phi_0 = 0$, this situation prevents analyses of the spot drifts using the technique proposed here. The parameter $\alpha$ for the flare stars BY Dra and EV Lac is about a quarter the value for LQ Hya, but this is not completely due to the presence of less pronounced active longitudes compared to LQ Hya or VY Ari. The latitude distribution of spots on flare stars deserves a separate analysis and comparisons with the expectations of the dynamo theory for very thick convection zones.

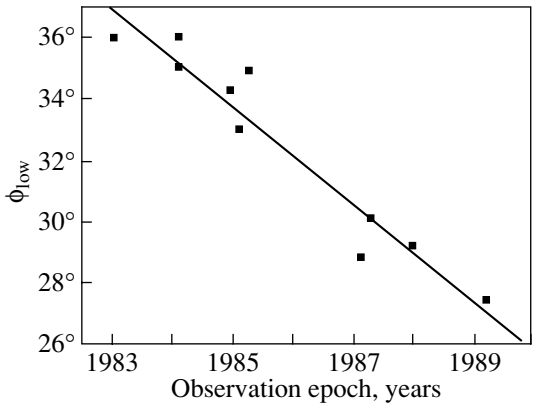


**Fig. 6.** Latitude of the lower boundary of the butterfly diagram for starspots on LQ Hya as a function of time (points) and the corresponding linear-regression fit.

## 5. DRIFTS OF STARSPOTS AND CYCLIC ACTIVITY

As noted in the Introduction, LQ Hya is characterized by high but irregular activity. Cyclic variations with periods of about 5 and 15 yr are suspected based on both the long-term brightness variations and the behavior of the relative spotted area on this star.

The drift rate of the lower boundary of the effective spot belt on LQ Hya can be estimated for various epochs using data similar to those presented in Fig. 2. In particular, the linear regression fit for 1983–1989 corresponds to a drift rate of $D = d\phi_{low}/dt = -1.58$ deg/yr with a correlation coefficient of $r = -0.96$ (Fig. 6). Similar figures were obtained for 1993–1999: the drift rate is $D = -1.71$ deg/yr, with $r = -0.92$. It seems likely that this drift and the close relationship between the spotted area and the latitude of the lower boundary of the diagram for LQ Hya reflect the rise phase of a cycle with a period of five to seven years. However, if we consider the entire rise phase of the 15-yr activity cycle of LQ Hya (1991–1999), the corresponding drift proves to be slower, $D = -0.88$ deg/yr, with a correlation coefficient of $-0.72$.

The drift rates of the lower boundary of the butterfly diagram for the activity-rise phases of the spotted stars studied are given in Table 2. The data in this table refer to the activity-rise years indicated, when the anticorrelation between the position of the lower boundary of the diagram and the spotted area was clearly pronounced ($|r| > 0.90$). We can see that the drift rates $D$ for the different stars do not differ widely. The drift of the spots on EK Dra and VY Ari is somewhat slower than on V775 Her. In this respect, LQ Hya occupies an intermediate position.

The obtained drift rates for the spotted stars are a factor of two to three lower than the corresponding

rates derived from the variations in the sunspot areas. The drift rate of the mean latitude of the Maunder butterflies during the rise phase of the 11-yr solar cycle was close to 4 deg/yr for the past (20th) century. The differences in the drift rates of the Sun and of the spotted stars considered here are related to differences in the characteristic time scales for their long-term variations, or, more precisely, to different durations of their activity-rise phases. The main period for the brightness variations is about three years for the Sun and ranges from five to ten years for the other spotted stars.

## 6. CONCLUSIONS AND DISCUSSION

Long-term photometric observations of active late-type stars are an important source of information about the characteristics of starspots and their distribution over the stellar surface. The spotted area can be determined most reliably and is virtually independent of the technique used to map the surface inhomogeneities. Multicolor photometry can be used to derive the spot temperatures with a fairly high degree of certainty.

In the absence of eclipses, the localization of spots on the stellar surface encounters severe difficulties. The most clearly expressed features of the light curve (the rotational modulation) are mainly due to the concentration of spots near certain longitudes. This problem has received much attention, first using Doppler imaging and, more recently, using inversion techniques. The effects of the latitude spot distribution on the brightness variations due to rotation and on variations of the activity level on characteristic time scales of one to ten years were either completely neglected or largely de-emphasized. In some cases, surface inhomogeneities were associated with only one, for example, the northern, hemisphere of the star.

The approach described here is a new representation and development of the zonal models. In principle, it can be applied to analyze the dependence of the brightness of the star on the latitudes of its spots. First and foremost, this is possible for stars that, according to the zonal models, have two well-separated spot belts. To make use of this possibility, we have introduced the notion of Maunder butterflies for stars, taking into account in a first approximation the effect of active longitudes. We have studied the single star LQ Hya in detail, while some other stars were discussed in [1].

The main conclusion of our analysis is that the latitude dependence of the brightness variations of a star is much more pronounced in the cases considered than was previously expected. When $\phi_0$ is constant in time, we can formally substitute $S_{sp} = \Delta w_b$ into the expression for $\phi_{low}$, which indicates that $\phi_{low}$ should grow linearly with $S_{sp}$ for a constant influence of the active longitudes (i.e., for a constant $f_{min}$). However, we have observed the opposite effect: $\phi_{low}$ decreases with increasing $S_{sp}$, which implies a decrease in the real lower boundary of the spot belt—the quantity $\Delta\phi_0$, which is due not only to the broadening of the belt but also to a real drift of the spots toward the equator.

Let us elucidate the physical meaning of this effect for the case when the stellar rotational axis is perpendicular to the line of sight. If spots appear at the beginning of a cycle in the region $\phi_1$, $\lambda_1$, their movement toward the equator as the cycle maximum approaches will increase their effect on the brightness of the star. This effect may be enhanced if spots in both the northern and southern hemispheres are concentrated near certain longitudes. In some cases, the influence of the latitude of the spot distribution on photometric measurements is already manifest in the behavior of the mean latitudes of the spot belt.

As noted above, the quantity $\bar{\phi} = \phi_0 + \Delta\phi/2$ and its variations from year to year depend implicitly on the spotted area via $\Delta\phi$. Before constructing the butterfly diagrams, it seemed that the second term in this expression should dominate during the activity-rise phase, i.e., $\bar{\phi}$ should increase with $\Delta\phi$. This behavior was observed for flare stars, which have only one spot belt. However, for the other spotted stars considered, the dependence of $\bar{\phi}$ on $\phi_0$ turned out to be strong and to exceed the effect of what we would expect to be the dominant factor—the increase of $\Delta\phi$ in the transition from low to high activity of the star.

The example of V833 Tau, which is viewed at an angle $i$ much smaller than 90°, provides independent confirmation of the detected effect. In this case, the second hemisphere of the star is essentially not observed at all, and the latitude effect should not reduce the rotational modulation of the brightness of the star due to the concentration of the spots near active longitudes. Indeed, the effect is considerably weaker for this star. In addition, the ratio of the amplitudes of the rotational modulation and long-term brightness variations, $\alpha$, also varies accordingly for V833 Tau.

We can see that the lower boundary of the butterfly diagram drifts toward the equator during the activity-rise phase (i.e., as the relative spotted area increases from year to year). This effect is very clearly expressed in all the cases considered (for zonal models with two spot belts), enabling us to determine the drift rates of the spots. These rates were found to be $-1$ to $-2$ deg/yr, a factor of two to three lower than the corresponding rate for the Sun. This result is important in the context of the dynamo theory for stars that are younger than the Sun.

Moreover, our analysis has yielded independent confirmation for the phenomenon of high-latitude activity, most notably on EK Dra and LQ Hya. Here, we have considered the single star LQ Hya in detail and demonstrated that the effects of tidal forces on the development of the dynamo process are not the only mechanism by which high-latitude activity can develop (as is likely the case in many RS CVn systems [21]). Note, however, that we are not referring here to the existence of polar spots on active late-type stars.

Some particular results of this study require further confirmation. The high stability inferred for the upper boundary of the butterfly diagram is interesting, and it would be instructive to verify this behavior using other tracers of stellar activity, such as calcium flocculi or prominences. It is known that sunspots do not drift poleward, but filaments (disk prominences) clearly demonstrate such drifts in the course of the solar cycle. The predictions of zonal models and of this study are sensitive to the accuracy of estimates of the angle $i$. Some poorly understood features in the behavior of the spot-belt parameters were detected near the activity maxima of the stars with the highest absolute values of $S_{sp}$. In this case, when the star spots approach the equator, it is difficult to choose between two possibilities: the model with two separated belts can be used almost interchangeably with the model with one equatorial belt. As a result, the accuracy of the zonal-model parameters could deteriorate compared to the accuracy given in [3]. On the other hand, further analyses of the spot distributions are needed during periods corresponding to the reversal of the global dipole field on the Sun. Despite these difficulties, it is important for studies of surface inhomogeneities based on the widespread Doppler-imaging and inversion techniques to take into account as fully as possible the latitude dependence of the spot distribution on the stars discussed here.

Our approach opens new possibilities for studies of surface activity. It is already clear that manifestations of the beginning of cyclic activity appear in the behavior of the spot-belt latitudes even before the corresponding maximum becomes reliably identifiable in the Fourier power spectrum of the brightness variations. Both the very existence of the equatorward drift of spots and its rate are important in this context. In our sample of spotted stars—LQ Hya, EK Dra, VY Ari, V775 Her, and V833 Tau—the drift rate is virtually independent of the axial-rotation rate. Although this result formally refers to periods from 1.6 to 16 days, it is likely valid for a large number of late-type stars with high but irregular activity and axial-rotation periods from 1–13 days. Studies of such stars were pioneered in [20, 22, 23], where an anticorrelation between the long-term variations of the photospheric and chromospheric emission was detected (in contrast to the *correlation* observed for stars with cyclic activities, including the Sun). A continuation of these studies and interpretation of our results in the framework of dynamo theory are topical problems.

## ACKNOWLEDGMENTS

We are grateful to R.E. Gershberg, D.D. Sokoloff, and G. Belvedere (Italy) for useful discussions. This work was supported by the Russian Foundation for Basic Research (project codes 01-02-17693 and 00-15-96553).

## REFERENCES

1. M. M. Katsova, M. A. Livshits, and G. Belvedere, Solar Phys. (2003, in press).
2. I. Yu. Alekseev and R. E. Gershberg, Astron. Zh. **73**, 589 (1996) [Astron. Rep. **40**, 538 (1996)].
3. I. Yu. Alekseev and R. E. Gershberg, Astron. Zh. **73**, 579 (1996) [Astron. Rep. **40**, 528 (1996)].
4. I. Yu. Alekseev and R. E. Gershberg, Astron. Zh. **74**, 240 (1997) [Astron. Rep. **41**, 207 (1997)].
5. F. C. Fekel, B. W. Bopp, J. L. Africano, *et al.*, Astron. J. **92**, 1150 (1986).
6. S. H. Saar, N. E. Piskunov, and I. Tuominen, in *The 8th Cambridge Workshop on Cool Stars, Stellar Systems, and the Sun,* ASP Conf. Ser. **64**, Ed. by Caillault J. P. (Astronomical Society of the Pacific, San Francisco, 1994), p. 661.
7. K. G. Strassmeier, J. B. Rice, W. H. Wehlau, *et al.*, Astron. Astrophys. **268**, 671 (1993).
8. J. B. Rice and K. G. Strassmeier, Astron. Astrophys. **336**, 972 (1998).
9. J. F. Donati, Mon. Not. R. Astron. Soc. **302**, 457 (1999).
10. S. V. Berdyugina, I. Ilyin, and I. Tuominen, *11th Cambridge Workshop on Cool Stars, Stellar Systems, and the Sun,* ASP Conf. Ser. **223**, Ed. by R. J. Garcia Lopez, R. Rebolo, and M. R. Zapatero Osorio (Astronomical Society of the Pacific, San Francisco, 2001), p. 1207.
11. S. V. Berdyugina, J. Pelt, and I. Tuominen, Astron. Astrophys. **394**, 505 (2002).
12. L. Jetsu, Astron. Astrophys. **276**, 345 (1993).
13. *IAU Symposium 176: Stellar Surface Structure,* Ed. by K. G. Strassmeier and J. L. Linsky (Kluwer, Dordrecht, 1996).
14. A. F. Lanza, S. Catalano, G. Cutispoto, *et al.*, Astron. Astrophys. **332**, 541 (1998).
15. S. S. Vogt, A. P. Harzes, and A. A. Misch, Astrophys. J., Suppl. **121**, 547 (1999).
16. I. Yu. Alekseev, *Spotted Low-Mass Stars* [in Russian] (Astroprint, Odessa, 2001).
17. J. D. Dorren, Astrophys. J. **320**, 756 (1987).

18. I. Yu. Alekseev, Astron. Zh. **80**, 467 (2003).
19. C. De Jager, *Structure and Dynamics of the Solar Atmosphere* (East. Berlin, 1959; Inostr. Lit., Moscow, 1962).
20. I. Yu. Alekseev, R. E. Gershberg, M. M. Katsova, and M. A. Livshits, Astron. Zh. **78**, 558 (2001) [Astron. Rep. **45**, 482 (2001)].
21. D. D. Sokolov and N. E. Piskunov, Mon. Not. R. Astron. Soc. **334**, 925 (2002).
22. R. R. Radick, G. W. Lockwood, B. A. Skiff, and S. L. Baliunas, Astrophys. J., Suppl. Ser. **118**, 239 (1998).
23. E. A. Bruevich, M. M. Katsova, and D. D. Sokolov, Astron. Zh. **78**, 827 (2001).

*Translated by A. Getling*

*Astronomy Reports, Vol. 47, No. 7, 2003, pp. 573–579. Translated from Astronomicheskiĭ Zhurnal, Vol. 80, No. 7, 2003, pp. 624–630.*


# Characteristic Features of the Spectrum of the Unique roAp Star HD 101065 near the 6708 Å Lithium Resonance Doublet

**A. V. Shavrina[1], N. S. Polosukhina[2], Ya. V. Pavlenko[1], A. V. Yushchenko[3], and V. F. Gopka[3,4]**

[1] *Main Astronomical Observatory, National Academy of Sciences of Ukraine, ul. Zabolotnogo 27, Kiev, 03680 Ukraine*

[2] *Crimean Astrophysical Observatory, Nauchnyi, Crimea, Ukraine*

[3] *Odessa National University, Park Shevchenko, Odessa, 65014 Ukraine*

[4] *Chonbuk National University, Chonju, 561-756 Korea*

Received June 6, 2002; in final form, November 27, 2002

**Abstract**—Synthetic spectrum of the peculiar roAp star HD 101065 (Przybylski's Star) have been computed in the wavelength interval 6705.8–6708.7 Å in order to describe the observed spectrum in the vicinity of the 6708 Å lithium line. Our detailed computations of the synthetic spectrum allowing for the hyperfine structure of the lithium line, lithium isotopic composition, and blending due to lines of rare-earth elements (CeII, NdII, SmII, and others) have yielded estimates of the atmospheric lithium abundance of the star and its $^6$Li/$^7$Li isotopic ratio. © *2003 MAIK "Nauka/Interperiodica".*

## 1. INTRODUCTION

Among roAp stars, whose spectra abound in individual peculiarities, HD 101065 is probably the most peculiar and most popular [1, 2]. Przybylski's first report demonstrating the unusual nature of the spectrum of HD 101065 in 1975 at IAU Colloquium 32 made a very strong impression on specialists interested in Ap stars, and this star immediately became a popular target of study. The absence (or very low intensity) of lines of such "normal" elements as iron and iron-group elements first noted by Przybylski imposes strong constraints on model atmospheres that are appropriate for analyses of the spectrum of this star. Along with certain substantial differences between the spectrum of this star and those of other Ap stars, Przybylski also pointed out a number of similarities:

(i) The strong absorption lines of rare-earth elements (REEs) in the spectrum of HD 101065 are also strong in the spectra of typical Ap stars ($\beta$ CrB and $\gamma$ Equ).

(ii) Some Ap stars, such as HD 25354, are strongly deficient in iron-peak elements.

(iii) Przybylski predicted that HD 101065 should possess a strong surface magnetic field (he interpreted the elemental-abundance anomalies in this star as a consequence of the stability of its atmosphere due to this strong magnetic field).

In 1976, Wolff and Hagen [3] discovered that the star indeed possesses a strong surface magnetic field with an intensity of about 2.5 kG. In the 1970s, Kurtz and Wegner [4] initiated observations of the oscillations of this star and detected well-defined pulsations with an amplitude of about $0.013^m$ and a period of 12.14 min. The object became the first Ap star for which such oscillations had been discovered. This phenomenon proved to be typical of some other Ap stars as well, forming the group of so-called roAp stars. Przybylski [1, 2] and Warner [5] were the first to try to identify the lines observed in the spectrum of HD 101065; these papers based on the earliest analyses of the spectrum of this unique Ap star were the first to note the possible presence of the resonance lithium doublet in the spectrum. In subsequent studies, Wegner and Petford [6] showed that Przybylski's star is the coolest known roAp star and attributed the peculiarities in the spectrum to the combined effect of the star's low temperature and an overabundance of RREs (by about 4 dex). The line identifications carried out by Warner [5] and Wegner *et al.* [6, 7] showed that most of the strong lines belong to REEs. Cowley *et al.* [8] demonstrated the presence of weak iron lines by analyzing the statistics of wavelength coincidences.

The effective temperature of the star is an important parameter when determining elemental abundances, especially when analyzing the ionization-stage distribution of REEs. The profiles of hydrogen lines, in particular, $H_\alpha$, have narrow cores and broad wings, making them unsuitable for determining the effective temperature. Strong blanketing due to

1063-7729/03/4707-0573$24.00 

**Table 1.** Observations of HD 101065

| Number of spectrum | Date | UT | Exposure, min | HJD 2450000+ | Spectral interval, Å |
|---|---|---|---|---|---|
| 04 | Mar. 11, 1996 | 5 11 | 20 | 153.726 | 6675–6735 |
| 26 | Mar. 10, 1996 | 4 41 | 20 | 152.705 | 6120–6180 |

numerous intense violet and blue REE lines makes correct photometric determinations of the temperature difficult. Theoretical computations of blanketing and its effect on model atmospheres are further hindered by the incompleteness of the atomic data for numerous REE lines for the three observed ionization stages. The effective temperature estimates of Kurtz and Wegner [4] based on observations of the infrared Paschen hydrogen lines and IUE spectra yielded the value $T_{\rm eff} = 7500$ K, and these authors classified the object as a cool roAp star. However, based on six-color observations, Przybylski concluded that the temperature of this star is close to that of the Sun, about 6000 K. This discrepancy was discussed extensively, and the effect of blanketing emerged as the most likely explanation. The increase of the density of absorption lines in the UV, especially those of REEs, reddens the star (so-called "back heating"). This effect is also well known for other Ap stars.

Cowley and Mathys [9] were the first to perform a detailed quantitative analysis of the spectrum of this star at 3900–6500 Å, and they pointed out the presence of lines of doubly ionized atoms of REEs (PrIII, NdIII, CeIII)—a feature that is not in good agreement with the low temperature estimate determined earlier. Further, Cowley *et al.* [10] concluded that spectral peculiarities similar to those observed for HD 101065 could develop only in stars with shallow convection zones, i.e., in stars with spectral types no later than F2. According to one possible explanation, the stellar atmosphere could be stabilized by a strong magnetic field. Cowley *et al.* [10] based their analysis on data for 3959–6652 Å and did not address the problem of the atmospheric lithium abundance.

The current paper supplements the work of Cowley *et al.* [10] with observations at 6675–6735 Å, with the primary aim of analyzing the lithium blend at 6708 Å and determining the atmospheric lithium abundance of HD 101065.

## 2. LITHIUM IN THE SPECTRUM OF HD 101065

Przybylski [1] was the first to note the presence of lithium in this star, in 1961. Warner [5] performed dedicated observations of the star with the 74″ reflector of the Radcliffe Observatory (Pretoria). He observed the spectrum at 3770–6880 Å with a dispersion of 6 Å/mm and found very strong lines of doubly ionized REEs at 5500–6880 Å, whose relative intensities were similar to the laboratory values tabulated by Meggers *et al.* [11]. However, Przybylski [1] pointed out that the SmII 6707.45 Å line can only be considered as a part of the lithium blend, while the main contributor is the lithium resonance doublet. Warner [5] was the first to estimate the lithium abundance of the star relative to the Sun ([Li] = 2.4) and to report the possible presence of $^6$Li.

## 3. OBSERVATIONS

Here, we analyze high-resolution (100 000), high signal-to-noise ($> 100$) spectra taken by P. North using the ESO CCD 34 (2048 pixels in the direction of the dispersion) mounted at the Coudé focus of the 1.5-m telescope of the European Southern Observatory. A Th–Ar lamp was used for the wavelength calibration, with the resulting errors being less than 0.3 km/s. The preliminary reduction of the data was performed by P. North using the IHAP software package of the European Southern Observatory. Table 1 gives a log of the observations (the time of the observations, exposure, and wavelength interval covered).

## 4. COMPUTATION OF THE MODEL ATMOSPHERES

Cowley *et al.* [10] performed a detailed analysis of the spectrum of HD 101065 using a model atmosphere with $T_{\rm eff} = 6600$ K and $\log g = 4.2$. We used the SAM12 [12] program to compute a model atmosphere with the same parameters and elemental abundances. SAM12 is a modified version of the ATLAS12 [13] code and of the previous versions of programs for computing model atmospheres and synthetic spectra [14, 15]. Pavlenko [12] made important modifications to the opacity-computation subroutines. The main advantage of SAM12 is that it can be used to compute model atmospheres for stars with different chemical compositions. As with ATLAS12, we specified the abundances of 99 elements as input parameters. These abundances were assumed to be independent of depth, as was the microturbulence velocity. The cross sections for free–bound absorption by CI, NI, and OI atoms were

computed earlier [12] using the TOPBASE [16] database. We allowed for the opacity of atomic lines using the opacity-sampling method [17]. The profile of the line-absorption coefficient was fitted using a Voigt function $H(a, v)$, and the damping constants were adopted from the databases or computed using the approximation of Unsold [18]. We compiled a list of atomic and ionic absorption lines at wavelengths $\lambda\lambda$ 40–60 000 nm based on the VALD list of atomic lines [19]. We adopted the parameters of the lines of REEs computed using the well-known program by Cowan (see, e.g., [20]), taken from the DREAM database [21]. Unfortunately, this database currently contains lines for only about one-quarter of the REEs. We also computed 6750/4.0 and 6500/4.0 models for $[M] = 0$ and compared them with Kurucz models [22] computed using the same parameters. A comparison of the temperature distribution in optical depth and the synthetic spectra shows that the models are similar; the blanketing by REEs is apparently compensated by the use of a different method to describe the turbulence, namely, convective overshooting instead of the mixing length.

## 5. ANALYSIS OF THE SPECTRUM OF HD 101065

We analyzed the spectrum of HD 101065 by computing synthetic spectra based on model atmospheres, using the STARSP [23] and ROTATE [24] programs developed by Tsymbal [23] and the URAN [25] program developed by Yushchenko. This latter code can be used to fit the elemental abundances in an automatic mode using the SYNTHE program [22] to compute the synthetic spectra. We computed the profile of the LiI 6708 Å blend for two model atmospheres: a 6750/4.0 Kurucz model and a model with the parameters and elemental abundances of the 6600/4.2 model of Cowley *et al.* [10], as described above. We used the VALD [19] atomic-line lists and DREAM [21] REE-line lists, preferring, when possible, the DREAM $gf$ values. We also computed the wavelengths of lines of (singly and doubly ionized) REEs based on REE energy levels adopted from the NIST database [26], taking into account the selection rules ($\delta J = 0, \pm 1$) and the odd–even and even–odd rule for the energy levels of the lower and upper states. For lines absent from the VALD and NIST databases, we chose the $gf$ values that resulted in the best agreement between the observed and computed spectra. There was only one such line in the immediate vicinity of the lithium line—SmII 6707.779 Å. We were able to place an upper limit on the $gf$ for this line of $-2.68$. The $gf$ values for two other lines neighboring the lithium line—NdII 6707.755 Å and 6708.03 Å, with $gf = -3.55$ and $gf = -1.13$, respectively—were estimated in [27] using the program of Cowan to supplement a trial identification of the upper level for the second line, which was absent from the NIST list of energy levels for REEs. This line (6708.03 Å) is blended with the strong CeII 6708.099 Å line, whose $gf$ value is included in the DREAM lists. The wavelength interval studied also contains a fairly "clean" CeII 6706.05 Å line, and the cerium abundance that we determined based on this line ($\log N(\mathrm{Ce}) = -7.63$) is in good agreement with the estimate of Cowley *et al.* [10] ($\log N(\mathrm{Ce}) = -7.60$). This cerium abundance yields $\log N(\mathrm{Nd}) = -7.97$, based on the 6708.03 Å NdII line with $\log gf = -1.13$. This estimate differs from that of Cowley *et al.* [10] ($-7.65(\pm 0.28)$) by 0.32, which only slightly exceeds the quoted error.

Table 2 lists all the lines included when computing the synthetic spectrum at 6705.5–6708.7 Å. The asterisks indicate lines with VALD or DREAM $gf$ values, while the last column indicates the corresponding sources. For the remaining lines, we chose the $gf$ values that resulted in the best agreement between the computed and observed spectra. Note that the VALD lines not included in this list do not contribute significantly to absorption in the spectral interval considered.

The lithium doublet was included as sixth component of a multiplet, with the wavelengths and oscillator strengths taken from [28]. We adopted a microturbulence velocity of $V_t = 2$ km/2 and the elemental abundances of [10], adjusting the latter for the four elements that are the main contributors to the absorption at wavelengths 6705–6709 Å to ensure the best agreement with the observed spectrum. The figure shows three synthetic spectra based on our model atmosphere with $T_{\mathrm{eff}} = 6600$ K and $\log g = 4.2$ for three cases: model A, which includes only lines of the main lithium isotope $^7$Li; model B, which includes lines of the $^6$Li isotope as well, with the $^6$Li/$^7$Li isotopic ratio fit as a free parameter; and model C, which excludes all the lithium lines, substituting the SmII 6707.799 Å line in their place. We chose the $gf$ value for this line to yield the best agreement with the observed spectrum. The marks at the top of the figure indicate the positions of lines that are the main contributors to the absorption in the wavelength interval considered. $^7$Li and $^6$Li mark the minima of the blends of the six lines of each isotope.

Table 3 lists the ion abundances derived by fitting the computed spectra for models A and B to the observed spectrum near 6708 Å. It is obvious that the fitted abundances vary only slightly. In all three cases, we used the same elemental abundances, corrected

**Table 2.** Lines included in the synthetic-spectrum computations at 6705.8–6708.7 Å

| Element | Wavelength, Å | Energy of the lower level (eV) | log $gf$ | Source |
|---|---|---|---|---|
| DyII | 6705.727 | 2.078 | −2.68 | |
| NdII | 6705.891 | 3.269 | −2.70 | |
| *YbII | 6705.965 | 5.856 | −3.04 | DREAM |
| *CeII | 6706.051 | 1.840 | −0.95 | DREAM |
| *TmII | 6706.150 | 5.322 | −1.07 | DREAM |
| *TmII | 6706.262 | 3.955 | −2.36 | DREAM |
| *CeII | 6706.307 | 3.195 | −2.40 | DREAM |
| PrIII | 6706.492 | 3.104 | −1.28 | |
| *PrIII | 6706.705 | 0.550 | −1.64 | DREAM |
| NdII | 6706.738 | 2.868 | −2.48 | |
| SmII | 6706.789 | 1.586 | −2.00 | |
| SmII | 6706.807 | 1.874 | −1.78 | |
| *TmII | 6706.906 | 4.908 | −2.47 | DREAM |
| NdII | 6706.922 | 3.211 | −0.88 | |
| NdII | 6707.015 | 1.490 | −1.88 | |
| NdII | 6707.033 | 2.222 | −3.68 | |
| *CeII | 6707.121 | 1.255 | −3.76 | DREAM |
| DyII | 6707.153 | 3.292 | −1.27 | |
| DyII | 6707.266 | 2.890 | −1.28 | |
| SmII | 6707.342 | 0.884 | −2.00 | |
| ErII | 6707.418 | 3.482 | −1.44 | |
| NdII | 6707.433 | 1.499 | −2.17 | |
| NdII | 6707.453 | 2.880 | −3.18 | |
| GdII | 6707.462 | 3.270 | −1.98 | |
| *SmII | 6707.473 | 0.930 | −1.48 | VALD |
| *YbII | 6707.603 | 6.651 | −1.38 | DREAM |
| SmII | 6707.648 | 1.746 | −1.27 | |
| *NdII | 6707.755 | 0.170 | −3.55 | DREAM (Quinet [27]) |
| *$^{7}$LiI | 6707.756 | 0.000 | −0.427 | (Smith *et al.* [28]) |
| *$^{7}$LiI | 6707.768 | 0.000 | −0.206 | " |
| SmII | 6707.779 | 2.037 | −2.68 | |
| *$^{7}$LiI | 6707.907 | 0.000 | −0.931 | (Smith *et al.* [28]) |
| *$^{7}$LiI | 6707.908 | 0.000 | −1.161 | " |
| *$^{7}$LiI | 6707.919 | 0.000 | −0.712 | " |
| *$^{6}$LiI | 6707.920 | 0.000 | −0.478 | " |
| *$^{7}$LiI | 6707.920 | 0.000 | −0.931 | " |
| *$^{6}$LiI | 6707.923 | 0.000 | −0.179 | " |
| *NdII | 6708.030 | 1.522 | −1.13 | DREAM (Quinet [27]) |
| *$^{6}$LiI | 6708.073 | 0.000 | −0.304 | (Smith *et al.* [28]) |
| *CeII | 6708.077 | 2.250 | −2.50 | DREAM |
| ErII | 6708.088 | 3.155 | −2.58 | |
| *CeII | 6708.099 | 0.701 | −2.12 | DREAM |
| NdII | 6708.400 | 3.192 | −2.48 | |
| NdII | 6708.458 | 3.536 | −1.08 | |
| NdII | 6708.629 | 0.746 | −4.58 | |

for NdII based on the 6708.03 Å line. Table 3 also gives the ion abundances corresponding to the best fit of the observed spectrum by the 6750/4.0 Kurucz atmosphere for model C, together with the results of Cowley *et al.* [10] for comparison. Our estimate of the lithium abundance for models A and B is $\log N(\mathrm{Li}) = -8.90$. Adding the lines of the $^6$Li isotope with the adopted isotopic ratio of $^6\mathrm{Li}/^7\mathrm{Li} = 0.3$ improved the agreement between the observed (dots in the figure) and computed (solid bold curve) spectra. The observed minimum at 6707.83 Å corresponds well to a blend of lithium lines with an isotopic ratio of $^6\mathrm{Li}/^7\mathrm{Li} = 0.3$. The corresponding minimum for case A, in which only the lines of $^7$Li were taken into account, is at 6707.80 Å.

Note the discrepancy between the VALD and DREAM $gf$ values for the PrIII 6706.705 Å line ($-1.285$ and $-1.64$, respectively). The DREAM PrIII abundance with $\log gf = -7.55$ is closer to the estimate of Cowley ($-7.60$), whereas the VALD $gf$ yields $\log N(\mathrm{PrIII}) = -7.91$. The $gf$ value that we used in our computations and which we adopted from the DREAM database also differs from the VALD value for CeII 6706.051 Å (by 0.3 dex). As noted above, we adopted the DREAM $gf$ values: this database provides data for a greater number of REE lines in the spectral interval considered. The fairly clean SmII 6707.47 Å line with $\log gf = -1.477$ from the VALD database yields a significantly lower SmII abundance ($-8.32$) than Cowley's estimate ($-7.75 \pm 0.29$). The DREAM database does not contain any SmII line lists, since Cowan's program cannot compute $gf$ values for this ion.

Table 4 gives the contribution of the absorption in the REE and lithium lines included in the computations as percentages of the total absorption at wavelengths 6707.64–6707.94 Å in steps of 0.02 Å (for $V_{\mathrm{micro}} = 2$ km/s without instrumental broadening, as is given by the STARSP program for model B, with $^6\mathrm{Li}/^7\mathrm{Li} = 0.3$).

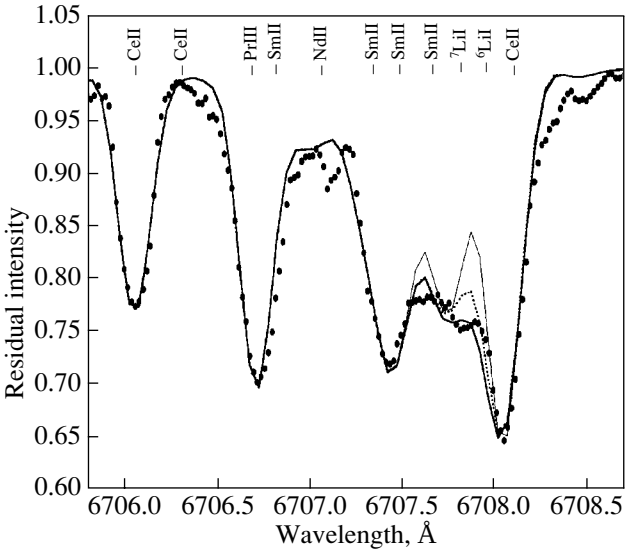


Comparison of the observed and computed spectra of HD 101065 in the vicinity of the 6708 Å blend. The dots show the observed spectrum, the dotted curve shows the spectrum computed taking into account only the main lithium isotope $^7$Li, and the bold solid curve shows the spectrum computed taking into account $^6$Li as well, with the isotopic ratio $^6\mathrm{Li}/^7\mathrm{Li} = 0.3$. The thin solid curve shows our attempt to fit the observed absorption near 6708 Å without lithium lines, using instead a SmII line with $\log gf = -0.629$. The marks at the top of the figure indicate the positions of lines that are the main contributors to absorption at the wavelengths considered. $^6$Li and $^7$Li mark the minima of the lithium-line blends for each isotope.

## 6. RESULTS AND DISCUSSION

Since the discovery of HD 101065 by Przybylski, the effective temperature of this star has remained a subject of debate. This is probably a consequence of blanketing due to strong absorption in the lines of rare-earth elements, both identified and unidentified. The incompleteness of the data for these lines makes it difficult to rigorously take this blanketing into account in model-atmosphere computations.

Cowley *et al.* [10] demonstrated conclusively the presence of a large overabundance of rare-earth elements and a deficit of iron-peak elements (Fe, Ni), although cobalt proved to be overabundant by 1.5 dex. They supplemented the list of REE lines with newly identified lines in the wavelength interval 3959–6652 Å. Our results are for the wavelength interval 6670–6735 Å, which includes the well-defined blend with the lithium resonance doublet at 6708 Å. We describe in detail our choice of parameters for the synthetic spectra near the LiI 6708 Å line computed allowing for REE lines with known and unknown $gf$ values. We analyzed models with and without lithium lines, and our results clearly demonstrate that the lithium doublet at 6708 Å is present in the spectrum of HD 101065. The profile of the observed blend is best fit by setting the $^6\mathrm{Li}/^7\mathrm{Li}$ isotopic ratio equal to 0.3. The peculiar chemical composition of the atmosphere, with a strong enhancement of REEs, may indicate a dredge-up of $r$-process elements, as was first suggested by Warner [5] in 1966. At the same time, the observed high lithium abundance (3.1 dex relative to hydrogen) suggests the action of some mechanisms preventing the complete de-

**Table 3.** Abundances of ions making the main contribution to the absorption spectrum of HD 1010645 near 6708 Å

| Element | Model A (only $^7$Li) | Model B ($^6$Li/$^7$Li = 0.3) | | [10] |
|---|---|---|---|---|
| | 6600/4.2 | 6600/4.2 | 6750/4.0 (Kurucz) | 6600/4.2 |
| LiI | −8.90 | −8.90 | −8.80 | – |
| CeII | −7.63 | −7.63 | −7.65 | −7.60+−0/26 |
| PrIII | −7.55 | −7.55 | −7.60 | −7.46+−0.16 |
| SmII | −8.32 | −8.32 | −8.25 | −7.75+−0.19 |
| NdII | −7.97 | −8.07 | −7.87 | −7.65+−0.28 |

**Table 4.** Absorption contribution of lines included when computing the blend as a function of wavelength (in percent of the continuum)

| Element | λ, Å | λ − 6707, Å | | | | | | | | | | | | | | | |
|---|---|---|---|---|---|---|---|---|---|---|---|---|---|---|---|---|---|
| | | 0.64 | 0.66 | 0.68 | 0.70 | 0.72 | 0.74 | 0.76 | 0.78 | 0.80 | 0.82 | 0.84 | 0.86 | 0.88 | 0.90 | 0.92 | 0.94 |
| SmII | 6707.648 | 19 | 18 | 13 | 7 | 2 | 1 | | | | | | | | | | |
| NdII | 6707.755 | | | | 1 | 1 | 2 | 3 | 2 | 1 | | | | | | | |
| $^7$LiI | 6707.756 | 3 | 4 | 6 | 7 | 9 | 9 | 11 | 9 | 8 | 6 | 5 | 3 | 2 | 1 | 1 | |
| $^7$LiI | 6707.768 | 3 | 5 | 8 | 10 | 13 | 15 | 18 | 15 | 14 | 12 | 10 | 6 | 4 | 3 | 2 | 1 |
| SmII | 6707.779 | | | | | | 1 | 1 | 1 | 1 | | | | | | | |
| $^7$LiI | 6707.907 | | | | | | | | 1 | 1 | 1 | 2 | 2 | 2 | 3 | 3 | 3 |
| $^7$LiI | 6707.908 | | | | | | | | | 1 | 1 | 1 | 1 | 1 | 2 | 2 | 1 |
| $^7$LiI | 6707.919 | | | | | | 1 | 1 | 1 | 1 | 2 | 3 | 3 | 4 | 4 | 4 | 5 |
| $^7$LiI | 6707.920 | | | | | | | | | 1 | 1 | 2 | 2 | 2 | 3 | 3 | 3 |
| $^6$LiI | 6707.920 | | | | | | | | 1 | 1 | 1 | 2 | 2 | 2 | 3 | 3 | 3 |
| $^6$LiI | 6707.923 | | | | | | | | 1 | 1 | 2 | 2 | 3 | 3 | 4 | 5 | 4 |
| NdII | 6708.029 | | | | | | | | | | | | | | | | 3 |

struction of lithium in mixing processes. This may be associated with the magnetic field, whose intensity reaches 2300 G at the surface [10]. In addition, the observed lithium may be produced in so-called spalling reactions at the stellar surface. This hypothesis is supported by the fact that the spectrum is better fit when the $^6$Li isotope is included with an isotopic ratio of $^6\mathrm{Li}/^7\mathrm{Li} = 0.3$. Based on a spectrum with a resolution of 0.3 Å, Warner [5] estimated the lithium abundance of the star to be 2.4 dex relative to the solar value, i.e., 3.3 dex relative to hydrogen. Warner also suggested the presence of $^6$Li at the surface of the star.

According to HIPPARCOS measurements, the parallax of the star is $7.95 \pm 1.07$ mas, implying an absolute magnitude of $M_v = 2.5 \pm 0.3^m$. This identifies the star as a relatively unevolved subgiant. At the same time, its spectrum is similar to those of S stars, which are located in another part of the Hertzsprung–Russell diagram and whose atmospheres are enriched in freshly synthesized material from deep layers. Thus, the spectral anomalies of HD 101065 described here await interpretation.

## 7. ACKNOWLEDGMENTS

We are grateful to P. North for presenting us the observed spectra, to V. V. Tsymbal for providing the STARSP and ROTATE programs, and to P. Quinet for the computations of $gf$ values to supplement those given in the DREAM lists. We are also grateful to

the administrators of the VALD, DREAM, NIST, and ADS databases, which are available via the Internet.

## REFERENCES

1. A. Przybylski, Nature **189**, 739 (1961).
2. A. Przybylski, Nature **210**, 20 (1966).
3. S. C. Wolff and W. Hagen, Publ. Astron. Soc. Pacif. **88**, 119 (1976).
4. D. Kurtz and G. Wegner, Astrophys. J. **232**, 510 (1979).
5. B. Warner, Nature **211**, 55 (1966).
6. G. Wegner and A. D. Petford, Mon. Not. R. Astron. Soc. **168**, 557 (1974).
7. G. Wegner, D. Cummins, P. Burne, *et al.*, Astrophys. J. **272**, 646 (1983).
8. C. R. Cowley, A. P. Cowley, G. Aikman, *et al.*, Astrophys. J. **216**, 37 (1977).
9. C. R. Cowley and G. Mathys, Astron. Astrophys. **339**, 165 (1998).
10. C. R. Cowley, T. Ryabchikova, F. Kupka, *et al.*, Mon. Not. R. Astron. Soc. **317**, 299 (2000).
11. W. F. Meggers, C. H. Corliss, and B. F. Seribnez, Nat. Bur. Stand. Mon. 32 (1961).
12. Ya. V. Pavlenko and S. Zhukovskaya, Kinemat. Fiz. Neb. Tel (2003, in press).
13. R. Kurucz, http://cfaku5.harvard.edu/.
14. Ya. V. Pavlenko, Astron. Zh. **76**, 115 (1999) [Astron. Rep. **43**, 94 (1999)].
15. Ya. V. Pavlenko and L. A. Yakovina, Astron. Zh. **77**, 243 (2000) [Astron. Rep. **44**, 209 (2000)].
16. M. J. Seaton, Rev. Mex. Astron. Astrophys. **23**, 180 (1992).
17. C. Sneden, H. Johnson, and B. Krupp, Astrophys. J. **204**, 281 (1976).
18. A. Unsold, *Physics der Sternatmospharen* (Springer, Berlin, 1955).
19. F. Kupka, N. E. Piskunov, T. A. Ryabchikova, *et al.*, Astron. Astrophys., Suppl. Ser. **138**, 119 (1999).
20. P. Quinet, P. Palmeri, and E. Bi'emont, J. Quant. Spectrosc. Radiat. Transf. **62**, 625 (1999).
21. E. Biemont, P. Palmeri, and P. Quinet, *Database of Rare Earths at Mons University,* http://www.umh.ac.be/astro/dream.shtml.
22. R. L. Kurucz, CD-ROM N 1-23 (Cambridge, MA, Smithsonian Astrophysical Observatory, 1993).
23. V. Tsymbal, Odessa Astron. Publ. **7**(2), 146 (1996).
24. A. V. Shavrina, N. S. Polosukhina, V. Tsymbal, *et al.*, Astron. Zh. **77**, 273 (2000) [Astron. Rep. **44**, 235 (2000)].
25. A. V. Yushchenko, in *Proceedings of the 20th Stellar Conference of the Czech and Slovak Astronomical Institutes,* Ed. by J. Dusek, ISBN 80-85882-08-6 (Brno, 1998), p. 201.
26. http://physics.nist.gov/cgi-bin/AtData.
27. P. Quinet, Private Communication (2002).
28. V. V. Smith, D. L. Lambert, and P. E. Nissen, Astrophys. J. **506**, 405 (1998).

*Translated by A. Dambis*

*Astronomy Reports, Vol. 47, No. 7, 2003, pp. 580–586. Translated from Astronomicheskiĭ Zhurnal, Vol. 80, No. 7, 2003, pp. 631–637.*


# Photometric and Polarimetric Activity of RZ Psc

**D. N. Shakhovskoĭ[1], V. P. Grinin[1,2], and A. N. Rostopchina[1]**

[1] *Crimean Astrophysical Observatory, Nauchnyi, Crimea, 98409 Ukraine*

[2] *Main Astronomical Observatory in Pulkovo, Pulkovskoe sh. 65, St. Petersburg, 196140 Russia*

Received August 12, 2002; in final form, January 10, 2003

**Abstract**—We present the results of synchronous photometric and polarimetric $UBVRI$ observations of the irregular variable star RZ Psc, acquired at the Crimean Astrophysical Observatory in 1989–2002. The star's photometric behavior is characterized by short, sporadic Algol-like dimmings. We observed only one deep minimum, with a $V$ amplitude of about $1.5^m$, during the entire observation time. During this minimum, the star's linear polarization reached 3.5%. Comparisons with polarization observations of RZ Psc during another deep minimum in 1989 show that the two minima can be described by the same polarization–brightness relation, testifying to an eclipsing nature for the minima. This provides evidence that the optical characteristics of the flattened circumstellar dust envelope that gives rise to the star's intrinsic polarization have remained virtually unchanged over the last 13 years. We argue that the origin of this stability is the presence of a large dust-free cavity in the central region of the circumstellar dust disk of RZ Psc. The cavity could be associated with binarity of the star or the formation of a planetary system, with most of the dust in the central region of the disk being transformed into large bodies—planetesimals and planets.


## 1. INTRODUCTION

The variability of RZ Psc was first discovered by Hoffmeister [1] in photographic observations. The star is classified in the variable-star catalog [2] as an irregular variable of spectral type KOIV displaying aperiodic Algol-like dimmings. Such stars spend most of their time in their bright state, and only occasionally dim their brightness by $2–3^m$, subsequently returning to the bright state. An important feature of their photometric behavior is the so-called "bluing effect," first observed by Götz and Wenzel in 1968 for CQ Tau [3]. This effect for RZ Psc was apparently first detected by Pugach [4] during the star's egress from a minimum.

An interesting property of RZ Psc is the brevity of its deep minima: as a rule, their duration does not exceed a day [4–11]; the descending and ascending branches of the minima are steep and symmetrical. Zaitseva [5] observed a brightness "standstill" during a deep minimum, when the star's brightness remained constant within 5–10% for several hours. In other words, the behavior of RZ Psc is similar to classical Algol-type eclipsing systems. Attempts have been made to detect periodicity in the occurrence of the deep minima for RZ Psc, but none of the suggested periods have been confirmed by subsequent observations [6, 7].

Thus, the pattern of the photometric activity of RZ Psc is similar to that observed for young UX Ori stars, which display large variability amplitudes due to variable circumstellar extinction [12]. However, no other evidence for RZ Psc being young has been revealed. The star was not detected as an infrared source by the IRAS satellite, and there is no Balmer line emission in its spectrum [13]. The existing observations in the near IR [14] do not show any significant infrared excess. In addition, RZ Psc is far from known star-forming regions. In this connection, the evolutionary status of the star remains incompletely understood.

For UX Ori stars, similar to RZ Psc in the character of their variability, the crucial confirmation of the eclipsing nature of their minima, as well as of the disklike shape of their circumstellar envelopes, was provided by the discovery of strong polarization of their light during brightness minima and the specific character of their polarization–brightness relation, predicted by the model of variable circumstellar extinction of [15]. In the case of RZ Psc, strong polarization was observed by Kiselev *et al.* [16] in one deep minima, but it is difficult to judge the character of the brightness–polarization relation from a single observation.

## 2. OBSERVATIONS

Our observations of RZ Psc were acquired on the 1.25-m telescope of the Crimean Astrophysical Observatory from 1987 until 2002 using the $UBVRI$

1063-7729/03/4707-0580$24.00 

photometer and polarimeter designed by Piirola [17]. Comparison star 1 from [3] was used as a local photometric standard. The photometric uncertainties did not exceed $0.05^m$ in the $U$ band and $0.03^m$ in the other bands. In our photometric observations, we applied the standard technique of correcting for the instrumental polarization using monthly observations of standard stars. The results of our photometry and polarimetry of RZ Psc are collected in the electronic table available in the database fttp://cdsarc.u-strasbg.fr/pub/cats/J and displayed in Figs. 1–5.

## 3. RESULTS

Figure 1 presents histograms of the activity of RZ Psc in the $UBVRI$ bands based on our observations and photoelectric observations by other authors [4–7, 10, 16]. Each point in a histogram corresponds to a single observation in a single night. When several brightness measurements were acquired on the same night, the results were averaged.

We can see from Fig. 1 that deep dimmings of RZ Psc are very rare. Thus, studies of this variable star require substantial effort and amounts of observing time.

### *3.1. The Photometric Activity of RZ Psc*

**Light curve.** The light curve of RZ Psc from our photometry and all published photoelectric observations is presented in Fig. 2. Earlier, we suggested [18] the presence of a many-year cycle in the behavior of RZ Psc during its bright state, with possible periods of 5200 and 2600 days. It follows from Fig. 2 that the later observations are better described by the shorter of these two cycles. Taking into account the new observations, we estimate that its duration is about 2700 days, or 7.4 years.

Figure 2 shows that the cyclic component of the light curve is a low-amplitude ($\Delta V \approx 0^m.3$–$0^m.4$) variation of the level of the star's bright state. We find no connection between the cyclic component of the light curve and the occurrence of deep minima for RZ Psc.

**Color–magnitude diagrams.** Figure 3 displays variations of the color indices of RZ Psc accompanying its $V$-band brightness changes, from our observations and the data of Kiselev *et al.* [16]. The color–magnitude relations for RZ Psc are similar to those for many other UX Ori stars [12]. They include an upper, linear part where the star is reddened and a subsequent change of the color indices in the opposite sense (the bluing effect) during the extended period of fading, due to the increased contribution from light scattered by circumstellar dust [15]. Comparison with photoelectric observations by other authors shows

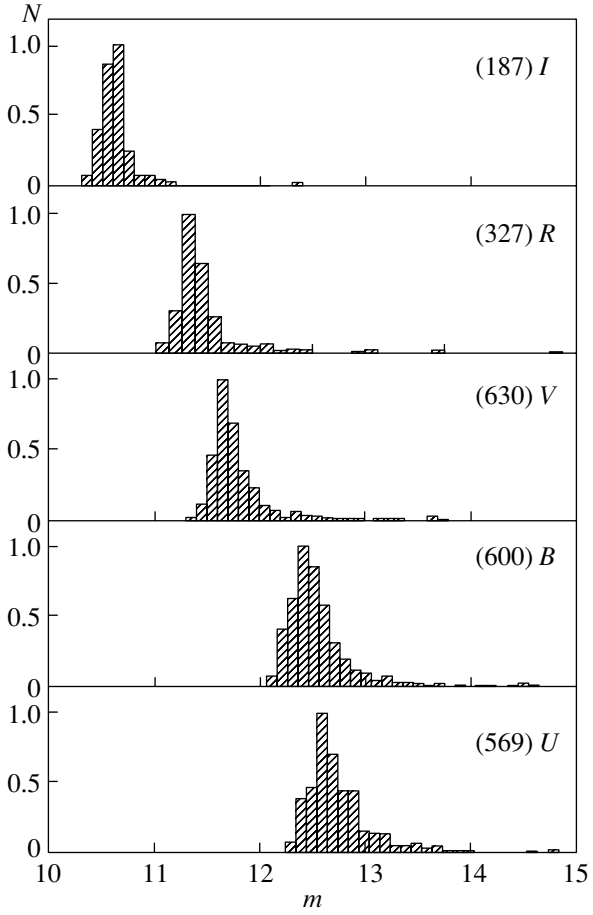


**Fig. 1.** Histograms of activity of RZ Psc based on photoelectric observations [4–8, 10, 16] and the data of this study.

that the behavior of the color indices of RZ Psc in the color–magnitude diagram (Fig. 3) does not differ from that observed during earlier years.

The slope of the upper part of the relationship between $B-V$ and $V$ (Fig. 3) can be used to estimate the ratio of the total circumstellar extinction to the selective extinction for RZ Psc: $R = \Delta V/\Delta(B-V) = 3.1 \pm 0.3$. This nearly coincides with the reddening law characteristic of the interstellar medium and differs somewhat from $R$ values derived earlier for other UX Ori stars ($R \approx 4$–$5$ [19–21]). This $R$ value gives us some idea of the mean selective extinction law in the circumstellar clouds. The large scatter of the data points in the color–magnitude diagrams (Fig. 3) shows that variations of the optical characteristics of the dust in individual clouds can be fairly substantial.

### *3.2. Linear Polarization of RZ Psc*

As can be seen in Fig. 2, we were able to measure the polarization of RZ Psc only during a single deep minimum, on JD = 24452208. Its depth, $\Delta V \approx 1^m.6$,

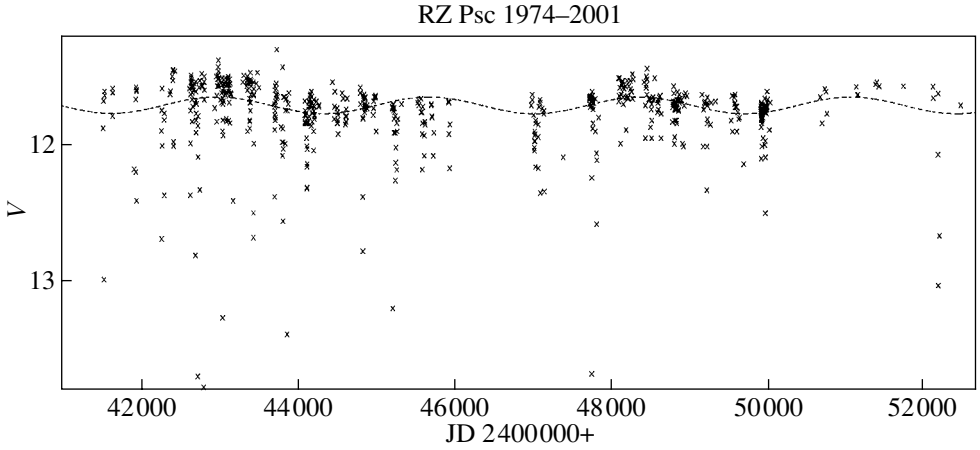


**Fig. 2.** Combined $V$ light curve of RZ Psc. The dashed curve is the hypothetical cyclic component with a 2700-day (7.4-year) period.

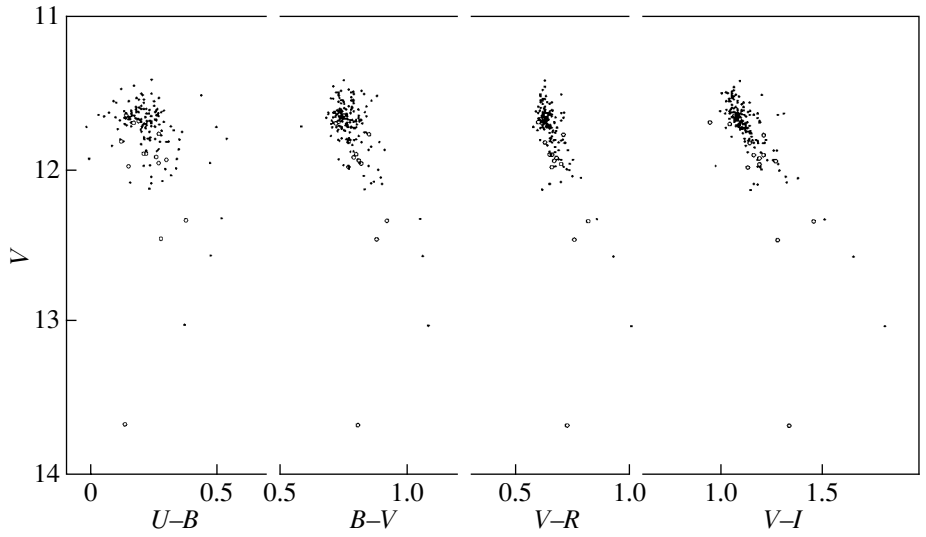


**Fig. 3.** Color–magnitude diagrams for RZ Psc. The points show our observations, and the circles, the data of Kiselev *et al.* [16].

was somewhat smaller than for the minimum observed by Kiselev *et al.* [16]. The degree of linear polarization was also lower, about 3.5%. This observation is just in the gap in the polarization–brightness relations (Fig. 4), between the main group of data points corresponding to the bright state and the single deep minimum observed by Kiselev *et al.* [16].

Figure 4 displays the relations between the polarization of RZ Psc and the star's brightness in the $V$ and $R$ bands, where we have polarization measurements for two deep minima. We can see that the polarization–brightness relation is similar to those observed for UX Ori stars [12], which can be described by the variable circumstellar extinction model of [15]. In this model, the relationship between the polarization parameters and the brightness is given by

$$\mathbf{P} = \mathbf{P}_{\rm is} + \mathbf{P}_{\rm in0} \times 10^{0.4\Delta m}, \qquad (1)$$

where $\mathbf{P}_{\rm is}$ and $\mathbf{P}_{\rm in}(0)$ are the pseudo-vectors corresponding to the interstellar polarization and the star's intrinsic polarization in its bright state (outside eclipses), due to light scattered by the circumstellar dust; $\Delta V$ is the amount of dimming, relative to the brightest state of the star.

Equation (1) is valid provided that (a) the dust clouds causing the eclipses introduce no additional polarization and (b) the Stokes parameters of the scattered light do not change during the studied time interval. Substituting the observed Stokes parameters of the linear polarization into the left-hand side of this relation and the amplitude of the dimming

Interstellar and intrinsic polarization of RZ Psc in its bright state derived from (1)

| Filter | $P_{is}$, % | $\sigma_{P_{is}}$, % | $PA_{is}$, % | $\sigma_{PA_{is}}$, % | $P_{in}(0)$, % | $\sigma_{P_{in}}$, % | $PA_{in}(0)$, % | $\sigma_{PA_{in}}$, % |
|---|---|---|---|---|---|---|---|---|
| $V$ | 0.54 | 0.06 | 111 | 3 | 0.68 | 0.04 | 48 | 2 |
| $R$ | 0.48 | 0.05 | 113 | 2 | 0.73 | 0.04 | 49 | 2 |

into the right-hand side, we obtain a redundant set of algebraic equations whose least-squares solution yields the Stokes parameters for the interstellar and intrinsic polarizations. The results of this analysis for the $V$ and $R$ bands are given in the table and shown as curves in Fig. 5.

It follows from the table that $\mathbf{P}_0$ and $\mathbf{P}_{is}$ are nearly orthogonal. Comparison with the intrinsic polarizations of UX Ori stars derived in a similar way [19–21] shows that the intrinsic polarization of RZ Psc is somewhat higher than the values observed for most UX Ori stars in their bright state. Thus, the light scattered by the circumstellar dust of RZ Psc is strongly polarized, possibly due to a somewhat smaller size of the dust grains in the envelope of RZ Psc. Here, the scattering medium is fairly conservative: the theoretical polarization–brightness relation describes equally well the star's polarization behavior during two deep minima separated by an interval of about 13 years.

Since the scattered light from the circumstellar disk places a natural restriction on the amplitudes of Algol-like minima of the corresponding stars [15], we can estimate the intensity of this scattered light. The maximum $V$ amplitude of the minima of RZ Psc (Fig. 1) is $\Delta V_{max} \approx 2\overset{m}{.}5$, so that $I_{sc} \approx 0.1 I_*$. Approximately the same ratio of the intensities of the direct and scattered light is observed for UX Ori stars [12].

## 4. DISCUSSION

Thus, the analysis above demonstrates deep similarities between the main characteristics of the optical light of RZ Psc and young UX Ori stars due to their circumstellar dust. The amount of scattered light, which contributes about 10% of the total light in the star's bright state, increases during eclipses by circumstellar dust clouds, explaining the growth of the star's polarization during minima and the decrease of its color indices (the bluing effect) observed during the deepest minima. As for UX Ori stars, the high polarization of the scattered light of RZ Psc requires that the circumstellar dust envelope be strongly flattened and have a small inclination to the line of sight.

The fact that the star + dust-disk system demonstrates strong scattering of light and simultaneously no evidence for thermal emission from the dust is quite surprising. This contradiction can be explained only if we suppose that their is a cavity in the dust envelope of RZ Psc that is void (or nearly void) of dust. If the inner boundary of the dust envelope is far from the star, the dust will be cool and the maximum of its thermal emission will be in the far IR.

Some UX Ori stars exhibit appreciable variability of the Stokes parameters of the scattered light, attributed to motion of the dust envelope in the close vicinity of the star [22]. These stars display a near-IR excess [12] and are variable on time scales from one to several weeks [23–25]. The fact that RZ Psc does not have an IR excess and the parameters of its scattered light were stable over more than 10 years provides further support for this interpretation.

However, the compact dust clouds that eclipse the star during deep minima most likely move close to the star, as suggested by the short duration of the minima. If the clouds are assumed to move in circular Keplerian orbits, then a duration of the minima of about 1 day corresponds to a distance of about 2 AU to the star.

The presence of a dust-free inner region could provide evidence for the formation of a planetary system around the young star, with the original material in the inner region of the protoplanetary disk already being partially dissipated and transformed into planetesimals and planets. In classical models of protoplanetary disks [26], the formation of terrestrial planets takes about a million years. The formation of giant planets takes $10^7$–$10^8$ years [27]. RZ Psc may be a comparatively young, solar-type (post T Tauri) star in which the inner part of the planetary system has already formed but the formation of giant planets has not been completed.

Another possible origin of a central cavity void of matter could be that we are dealing with a young binary system. According to the computations of Artymowicz and Lubow [28], a cavity is formed in this case due to periodic tidal perturbations caused by the orbital motion of the system's components around their common center of mass. The characteristic size of this cavity depends on the secondary's orbital eccentricity and is approximately $2$–$4a$, where $a$ is the semimajor axis of the orbit. This theoretical result is generally confirmed by high-angular-resolution IR observations of young binary systems (cf. the review of Mathieu *et al.* [28] and references therein).

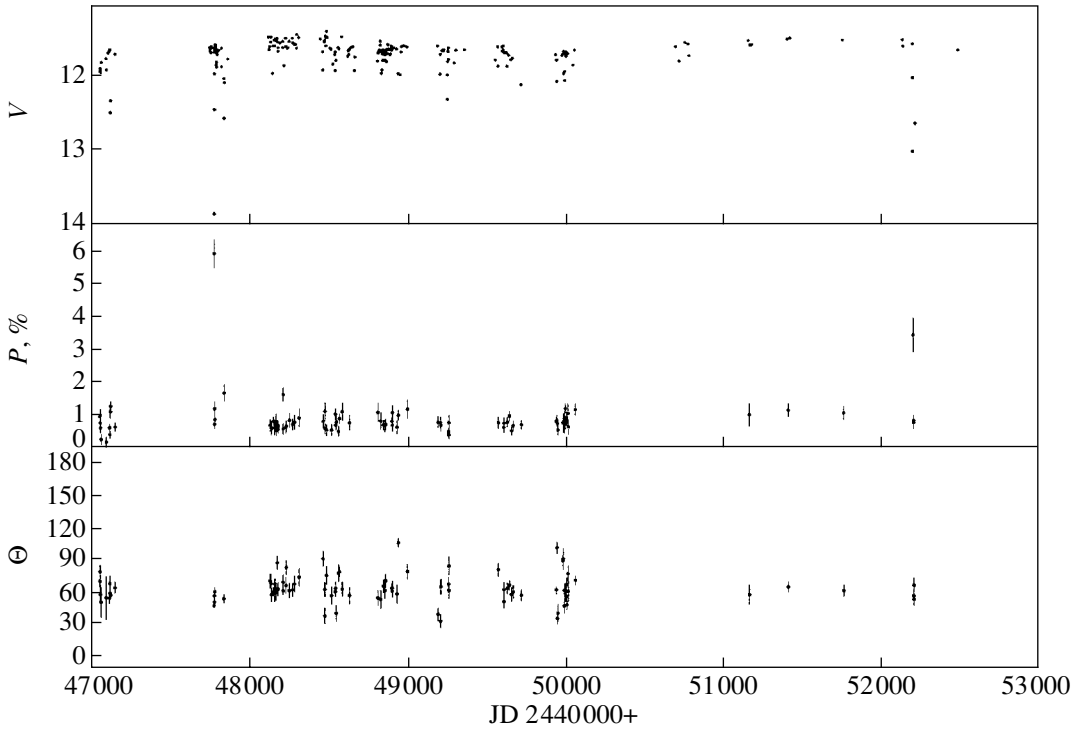


**Fig. 4.** $V$-band light curve and polarization parameters of RZ Psc based on data from the current paper and from Kiselev *et al.* [16].

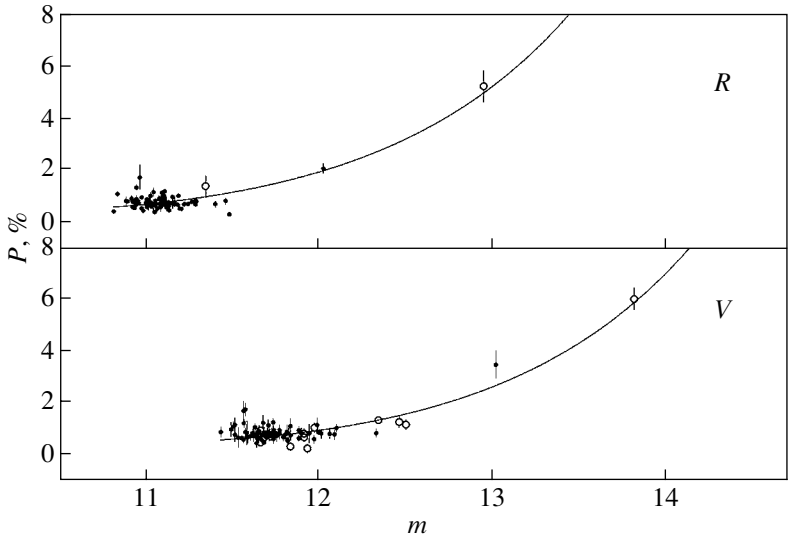


**Fig. 5.** $VR$ polarization–brightness relations for RZ Psc. The dots show the data of the current paper, and the circles, the data of Kiselev *et al.* [16]. The curves are theoretical polarization–brightness relations for the variable circumstellar-extinction model of [15] computed using data from the table.

In addition to giving rise to an inner cavity void of matter, the proposed binarity of RZ Psc could be manifest in the star's cyclic low-amplitude brightness variability. The characteristic duration of the cycle is about 7.4 years. If the star's mass is about 1 $M_\odot$, the radius of the secondary's orbit should be about 3 AU. In this case, in the model of Artymowicz and Lubow [28], the size of the dust-free cavity should be about 10 AU, in agreement with the supposed low temperature of the scattering envelope.

At the same time, the compact dust clouds that eclipse the star during deep minima are probably

moving fairly close to the star, as evidenced by the short duration of the minima. Judging from the rareness of the deep minima, these compact clouds inside the nearly dust-free cavity can screen only a small fraction of the star's light and, therefore, do not contribute significantly to the infrared radiation or to scattering in the optical.

## 5. CONCLUSIONS

The observed characteristics of the photometric and polarimetric activity of RZ Psc lead to the following conclusions about the optical properties and geometry of its circumstellar dust.

(1) The star is surrounded by a flattened dust envelope (circumstellar disk) whose equatorial plane has a small inclination to the line of sight. This orientation of the circumstellar disk is the primary distinguishing feature of UX Ori stars [12] and one of the conditions required for the formation of the strongly polarized scattered light observed during their deep minima.

(2) The intensity of the scattered light of RZ Psc is about 10% of the intensity of the star's direct light, comparable to the values of this ratio for UX Ori stars [12, 15, 19–21]. The optical properties of the dust in the circumstellar clouds probably do not differ strongly from those of interstellar dust. This conclusion is based on our analysis of color–magnitude diagrams for RZ Psc, which show that the extinction law in the circumstellar-dust envelope ($R \approx 3.1$) is close to the mean extinction law for the interstellar medium.

(3) The character of its brightness variability, behavior of its color indices during deep minima, and linear polarization of RZ Psc indicate that this object is a member of the group of UX Ori stars, which are young objects (predominantly Herbig Ae stars and early-type T Tauri stars). On the other hand, no line emission was detected for RZ Psc [13], it displays no IR excess, and the star is far from regions of intense star formation.

(4) The absence of an IR excess together with the presence of strong scattering of light provides evidence for an extended dust-free cavity between the star and its circumstellar disk. The disk itself is fairly cool (partly because the star's luminosity is not high), and it efficiently scatters the star's optical light. However, most of its thermal emission is in the far IR.

(5) The existence of a dust-free cavity may mean that the process of planetary formation is already over in the inner part of the protoplanetary disk of RZ Psc, so that the primordial matter has already been either transformed into planetesimals and planets or scattered. Another possibility is that RZ Psc is a young binary system, and the central cavity was formed by the orbital motion of the system's components.

We failed to find radial-velocity measurements of this star in the literature. Such measurements would be highly desirable to test the hypothesis of its binary nature.

It is clearly of considerable interest to continue studies of RZ Psc in order to determine its evolutionary status. The detection of excess radiation in the far IR due to remnants of the protoplanetary disk would provide important evidence that the star is indeed relatively young.

## ACKNOWLEDGMENTS

We are grateful to S.A. Lamzin for helpful remarks.

This study was supported by the grant "Nonstationary Processes in Astrophysics" from the Presidium of the Russian Academy of Sciences.

## REFERENCES

1. C. Hoffmeister, Astron. Nachr. **242**, 129 (1931).
2. P. N. Kholopov, N. N. Samus', V. P. Goranskiĭ, *et al.*, *General Catalog of Variable Stars* [in Russian] (Nauka, Moscow, 1985).
3. W. Götz, W. Wenzel, Mitt. Verand. Sterne Bd. **5**, 13 (1968).
4. A. F. Pugach, in *IAU Symp. No. 67: Variable Stars and Stellar Evolution*, Ed. by V. Sherwood and L. Plaut (Reidel, Dordrecht-Boston, 1975), p. 143.
5. G. V. Zaitseva, Pis'ma Astron. Zh. **4**, 283 (1978) [Sov. Astron. Lett. **4**, 154 (1978)].
6. V. I. Kardopolov and G. K. Filip'ev, Astron. Zh. **65**, 816 (1988) [Sov. Astron. **32**, 424 (1988)].
7. V. I. Kardopolov, V. V. Sakhanenok, and N. A. Shutemova, Perem. Zvezdy **21**, 310 (1980).
8. A. F. Pugach, Perem. Zvezdy **23**, 391 (1996).
9. V. P. Tsesevich, Perem. Zvezdy **10**, 406 (1955).
10. G. V. Zaitseva, Perem. Zvezdy **22**, 181 (1985).
11. V. G. Karetnikov and A. F. Pugach, Inf. Bull. Var. Stars, No. 783, 1 (1973).
12. V. P. Grinin, N. N. Kiselev, N. Kh. Minikulov, *et al.*, Astrophys. Space Sci. **186**, 283 (1991).
13. B. M. Kaminskiĭ, G. U. Koval'chuk, and A. F. Pugach, Astron. Zh. **77**, 689 (2000) [Astron. Rep. **44**, 611 (2000)].
14. I. S. Glass and M. V. Penston, Mon. Not. R. Astron. Soc. **167**, 237 (1974).
15. V. P. Grinin, Pis'ma Astron. Zh. **14**, 65 (1988) [Sov. Astron. Lett. **14**, 27 (1988)].
16. N. N. Kiselev, N. Kh. Minikulov, and G. P. Chernova, Astrofizika **34**, 333 (1991).
17. V. Piirola, Observ. Astrophys. Labor. Univ. Helsinki Rept. No. 6, 151 (1984).
18. A. N. Rostopchina, V. P. Grinin, and D. N. Shakhovskoĭ, Pis'ma Astron. Zh. **25**, 291 (1999) [Astron. Lett. **25**, 243 (1999)].
19. N. V. Voshchinnikov and V. P. Grinin, Astrofizika **34**, 181 (1991).

20. A. N. Rostopchina, V. P. Grinin, A. Okazaki *et al.*, Astron. Astrophys. **327**, 145 (1997).
21. V. P. Grinin, E. A. Kolotilov, and A. N. Rostopchina, Astron. Astrophys., Suppl. Ser. **112**, 457 (1995).
22. V. P. Grinin, in *The Nature and Evolutionary Status of Herbig Ae/Be Stars*, ASP Conf. Ser. **62**, Ed. by P. S. Thé, M. R. Pérez, and E. P. J. van den Heuvel (Astronomical Society of the Pacific, San Francisco, 1994), p. 63.
23. R. D. Oudmaijer, J. Palacios, C. Eiroa, *et al.*, Astron. Astrophys. **379**, 564 (2001).
24. M. G. Hutchinson, J. S. Albinson, P. Barrett, *et al.*, Astron. Astrophys. **285**, 883 (1994).
25. V. P. Grinin, D. N. Shakhovskoĭ, V. I. Shenavrin, *et al.*, Astron. Zh. **79**, 715 (2002) [Astron. Rep. **46**, 646 (2002)].
26. V. S. Safronov, *Evolution of Protoplanetary Cloud and Forming of Earth and Planets* [in Russian] (Nauka, Moscow, 1969).
27. J. B. Pollack, O. Hubickyj, P. Bodenheimer, *et al.*, Astrophys. J. **421**, 615 (1994).
28. P. Artymowicz and S. H. Lubow, Astrophys. J. **467**, L77 (1996).
29. R. D. Mathieu, A. M. Ghez, E. L. N. Jensen, and M. Simon, in *Protostars and Planets IV*, Ed. by V. Mannings, A. P. Boss, and S. S. Russel (Univ. of Arizona Press, Tucson, 2000), p. 703.

*Translated by N. Samus'*

*Astronomy Reports, Vol. 47, No. 7, 2003, pp. 587–599. Translated from Astronomicheskiĭ Zhurnal, Vol. 80, No. 7, 2003, pp. 638–651.*


# Magnetic Fields of White Dwarfs

**G. G. Valyavin, T. E. Burlakova, S. N. Fabrika, and D. N. Monin**

*Special Astrophysical Observatory, Nizhniĭ Arkhyz, Russia*

Received October 5, 2002; in final form, November 27, 2002

**Abstract**—We present results of Zeeman CCD measurements of DA white dwarfs carried out with the 6-m telescope of the Special Astrophysical Observatory in 1995–2000. The accuracy of the measurements ranges from 0.5 to 15 kG. Magnetic fields were detected in three of the 26 observed white dwarfs. We have confirmed the existence of magnetic fields on WD 1953–011 ($B_e = 28 \pm 6$ kG) and 40 Eri B ($B_e(\min) = -2.8$ kG, $B_e(\max) = 1.8$ kG). The data are discussed in the context of a statistical study of the occurrence of magnetic white dwarfs. © *2003 MAIK "Nauka/Interperiodica"*.

## 1. INTRODUCTION

Magnetic-field measurements for single white dwarfs obtained with the 6-m telescope of the Special Astrophysical Observatory (SAO) have been aimed at studying the surface magnetic fields of these stars, determining their rotational periods, and investigating the relationship between their magnetic fields and rotations. Knowledge of these quantities and relations would make it possible to restrict assumptions in theories of the evolution of intermediate-mass stars. For instance, the rotational periods and surface magnetic fields of white dwarfs could be used to find the fraction of angular momentum and magnetic flux that is lost by a giant during the formation of the degenerate core and associated mass loss. The distribution of white-dwarf magnetic-field strengths could yield information about whether magnetic white dwarfs represent an independent class with strong surface fields or whether their magnetic fields are fossils of the magnetic fields of their progenitors (i.e., magnetic white dwarfs are those objects with the strongest fields in a continuous distribution of field strengths).

The accumulation of observational data on the magnetism of white dwarfs and statistical analyses of such data are also important for investigations of the evolution of stellar magnetic fields. While the theory of stellar magnetism has been developing quite successfully [1–2], investigations of the magnetic fields of white dwarfs based on observations were virtually absent until recently. This problem was discussed well before the mid-1990s by Liebert and Sion [3], who concluded that magnetic white dwarfs may become more abundant with decreasing effective temperature. This could be due to either observational selection effects or evolution of the surface magnetic fields of white dwarfs. Later studies [4] raised doubts about the existence of this effect, but the observational data were too few to resolve the question. This problem was not discussed further until our recent studies [5, 6].

There is hope that addressing this observational deficiency by increasing the number of white-dwarf magnetic-field measurements will enable us to resolve the problem of the origin and evolution of the magnetic fields of these stars. The main difficulty is that existing observational data on the magnetic fields of degenerate stars remain insufficient for reliable statistical analyses. With this in mind, we are continuing our observational program, and we present here new results of magnetic-field observations of white dwarfs carried out in 1995–2000.

Before 1995, observations were carried out with a hydrogen-line magnetometer equipped with a photoelectric detector [7–11]. Observations of DA white dwarfs were obtained simultaneously in the wings of the H$\beta$ and H$\gamma$ lines. The techniques used for the observations are described in [12] and [9]. The methods used to estimate the accuracy of the measurements, monitor the operation of the equipment during the observations, and estimate the background are described in detail in [8]. These observations, as well as those of [13], have shown that white dwarfs with magnetic fields of $B \geq 10$ kG are not numerous. Starting from 1995, our white-dwarf magnetic-field measurements were acquired using a CCD detector and applying the standard methods of Zeeman spectroscopy.

In the statistical studies [5] and [6], it was found that the fraction of magnetic white dwarfs with $B >$ 1 MG is about 2% among hot (young) objects and about 20% among cool (old) stars. The $B$ distribution for white dwarfs can be represented as a power law with an index close to 1.5. We introduced this

1063-7729/03/4707-0587$24.00 

**Table 1.** Magnetic-field measurements obtained with the MSS

| Object | JD 2450000+ | Exposure, min | $B_e$, kG | $\sigma$, kG | Sp | $V$ |
|---|---|---|---|---|---|---|
| WD 0148+467 | 9973.511 | 10 | 15.3 | 9.6 | DA3.5 | 12.4 |
| – | 9974.444 | 20 | 14.1 | 5.9 | – | – |
| WD 0227+050 | 9975.506 | 60 | −2.6 | 3.3 | DA3 | 12.7 |
| 40 Eri B | 9973.559 | 19 | −1.9 | 1.9 | DA3-4 | 9.5 |
| – | 9975.570 | 81 | 0.5 | 0.37 | – | – |
| – | 10061.334 | 204 | −0.06 | 0.48 | – | – |
| WD 0713+584 | 10062.301 | 113 | 0.07 | 1.02 | DA4 | 12.0 |
| WD 2032+248 | 9943.443 | 60 | −2.7 | 3.1 | DA3 | 11.5 |
| WD 2341+322 | 10062.153 | 30 | 13.4 | 9.0 | DA4 | 12.9 |

white-dwarf "magnetic-field function" earlier (see, e.g., [11]); it essentially represents the probability density for the occurrence of white dwarfs as a function of magnetic-field strength. The normalization properties of the magnetic-field function can be used to estimate the incidence of magnetic white dwarfs with weak fields. We found [5, 6] that the minimum surface magnetic fields of hot ($T > 10\,000$ K) dwarfs are confined to 1–10 kG, while the minimum surface magnetic fields of cool ($T < 10\,000$ K) dwarfs can range from 10 to 50 kG. These data suggest that the time scales for, and possibly the direction of, the evolution of the magnetic fields of white dwarfs disagrees with many theoretical predictions. In particular, Wendell *et al.* [1] have claimed that the observations are not able to detect the evolution of white-dwarf magnetic fields since the time scale for this evolution is very long.

The results above illustrate the effectiveness of statistical approaches to studies of the evolution of white-dwarf magnetic fields. They also show that new observational data are needed, especially for stars with weak fields (1–10 kG). In the current paper, we generalize our approach and present a complete list of all data obtained in 1995–2000. Some of the data obtained before 1998 have already been published (see, e.g., [14, 15]).

## 2. OBSERVATIONS WITH THE MAIN STELLAR SPECTROGRAPH

The highest accuracy of white-dwarf magnetic-field measurements obtained using hydrogen-line magnetometers was $\approx 1$ kG. In particular, the accuracy attainable for the brightest member of the class, 40 Eri B, was 1.1 kG [11]. Further observational advances have required increases in the accuracy of these measurements. Subsequent observations [15] were carried out using the Main Stellar Spectrograph (MSS) mounted on the 6-m telescope of the SAO with a circular-polarization analyzer [16]. A 1000 × 1000-pixel CCD detector was used. The observations were obtained using Camera II of the MSS [17] in the vicinity of H$\alpha$ with a dispersion of 0.24 Å/pixel and a spectral resolution of about 0.6 Å.

A typical feature of H$\alpha$ lines in the spectra of DA white dwarfs ($8000\ \mathrm{K} < T_{\mathrm{eff}} < 25\,000$ K) is the presence of a narrow non-LTE absorption profile with half-width $\leq 1$ Å in the core of the line [18]. Spectropolarimetric observations of this feature can ensure high accuracy of the magnetic-field measurements. We chose the brightest (to $13^m$) DA white dwarfs with sharp Balmer lines from the catalog of McCook and Sion [19] for our observations. Based on broadband photometry, we further selected stars with effective temperatures between 8000 and 22 000 K. We used the central part of the H$\alpha$ profile for the measurements.

The standard mode for Zeeman measurements with the MSS and circular-polarization analyzer [12] is based on measuring the positional shift of the observed line in the left- and right-circularly polarized spectra, correcting this shift for instrumental errors using observations of standard stars. In this mode, we obtain only the longitudinal component of the magnetic field integrated over the stellar disk, $B_e$—the effective magnetic field [20]. The integrated magnetic-field vector can be reconstructed using additional observations of the linear polarization of the Zeeman components of the spectral lines. For initial

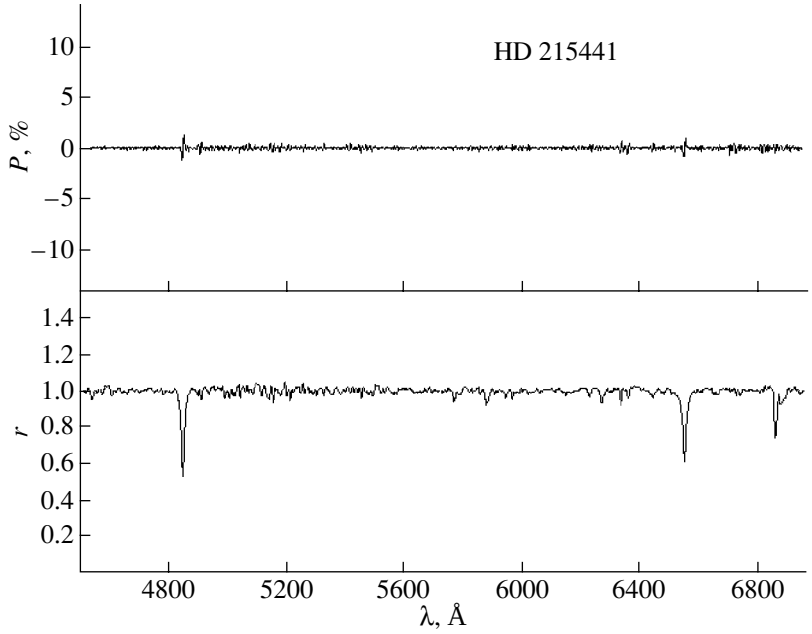


**Fig. 1.** Spectrum (lower panel) and circular polarization (upper panel) of HD 215441.

studies, observations of the effective field alone are quite sufficient.

Let us discuss briefly the accuracy of Zeeman measurements based on observations of the H$\alpha$ line in the spectra of bright DA white dwarfs. This accuracy can be estimated via modeling. The typical residual H$\alpha$ intensities for the DA white dwarfs studied are $r = 0.5$–$0.6$. The results of our analysis in [14] show that, for such residual intensities and spectra with signal-to-noise ratios S/N $\approx$ 100, the accuracy with which the line splitting can be determined is about 0.015–0.020 Å. Near the H$\alpha$ line, this corresponds to uncertainties in the effective fields of 400–500 G (see also [21]). Higher accuracies can be achieved by accumulating spectral data. The accuracy of the Zeeman observations of white dwarfs quoted above is currently the best achieved (see [13] and Section 4 below).

Table 1 lists the results of the Zeeman observations of the target stars. The columns give the (1) object names, (2) Julian dates of the middle of the exposure time, (3) exposure times, (4) measured effective fields $B_e$ and (5) their errors, (6) spectral classification according to McCook and Sion [19], and (7) apparent $V$ magnitudes of the stars. The accuracy of the magnetic-field measurements ranges from several hundred Gauss to several kiloGauss. For 40 Eri B and WD 0713+584, the data in the table are the result of analyzing several series of short (3- and 5-min for 40 Eri B and 5- and 10-min for WD 0713+584) exposures. Each estimate of the effective field is an average over one series, with correction for the systematic (instrumental) shift of the lines. The error estimates are based on analysis of the internal consistency of these series. For a series obtained under very good visibility conditions ($\approx 0.6''$–$0.8''$, JD 2449975.570), the summed spectrum has S/N $\approx$ 80. For such a summed spectrum, using the model data [14], we obtain an estimated magnetic-field accuracy based on a single line of about 400 G ($r \approx 0.6$). Agreement between the real (based on internal consistency of the series) and model error estimates confirms the correctness of the model analysis.

## 3. OBSERVATIONS WITH THE SP-124 SPECTROGRAPH

Polarimetric observations of optically weak white dwarfs with the MSS are not efficient. For this reason, beginning in 1997, our observations were carried out with the moderate-resolution SP-124 spectrograph, which is equipped with a 1024 × 1024-pixel. Photometrics CCD detector with a maximum quantum efficiency of 75% at $\lambda$ 6000 Å and a polarimetric analyzer [23]. Its spectral dispersion of 2.3 Å/pixel, which provides a spectral resolution of about 6 Å, is not sufficient to study the central non-LTE profile of the H$\alpha$ line. However, due to the considerable gain in the photon-flux detection rate compared to the MSS, we were able to study the polarization in the central parts of the H$\alpha$ and H$\beta$ profiles in more detail. The technique used to conduct the magnetic-field measurements is almost the same as that used with the MSS. For spectra with signal-to-noise ratios higher

**Table 2.** Results of magnetic field measurements

| Object | JD 2450000+ | $N$ | $B_e$, G | $\sigma$, G | Sp | $V$ |
|---|---|---|---|---|---|---|
| WD 0009+501 | 1423.5 | 21 | −10 000(max) | 7000 | DA8 | 14.4 |
| – | – | – | −74 000(min) | 6000 | – | – |
| WD 0034−211 | 1884.2 | 4 | 35 000 | 13 000 | DA7 | 14.5 |
| WD 0101+048 | 1887.3 | 4 | 500 | 2200 | DA4 | 14.0 |
| WD 0148+467 | 684.4 | 2 | −400 | 4500 | DA3.5 | 12.4 |
| WD 0235+064 | 1888.4 | 5 | −1700 | 5000 | DA8 | 15.1 |
| WD 0509+168 | 188(4−8) | 28 | 6200 | 2100 | DA8 | 13.6 |
| WD 0532+414 | 1887.4 | 3 | 2500 | 5000 | DA7 | 14.8 |
| WD 0627+299 | 1885.4 | 10 | 15 900 | 13 000 | DA | 14.8 |
| WD 0727+482 | 1886.4 | 4 | No lines | – | DC9 | 14.6 |
| WD 0939+071 | 1887.5 | 6 | −3200 | 4500 | DA7 | 14.9 |
| WD 1019+637 | 1888.45 | 3 | 8200 | 7500 | DA7 | 14.7 |
| WD 1126+185 | 950.8 | 2 | −3200 | 10 500 | DC8 | 13.8 |
| WD 1756+827 | 1888.5 | 3 | 4200 | 4500 | DA7 | 14.3 |
| WD 1953−011 | 1357.5 | 6 | −28 000 | 6000 | DA6 | 13.7 |
| WD 2032+248 | 684.3 | 2 | 800 | 4200 | DA3 | 11.5 |
| WD 2326+049 | 684.4 | 3 | 150 | 2400 | DAv4 | 13.1 |
| WD 2341+322 | 1421.5 | 18 | −1400 | 12 000 | DA4 | 12.9 |

than 150, the typical accuracy of the measurements ranges from 2 kG (for stars brighter than $14^m$) to 10 kG and can reach 700 G for bright objects. This can be illustrated using test measurements for magnetic Ap/Bp stars.

Figure 1 shows the polarization spectrum of the magnetic star HD 215441, obtained at the rotational phase when the effective magnetic field was 10 kG. The analysis of the polarization in the H$\alpha$ line yielded the effective magnetic field $B_e = 10\,500 \pm 700$ G. The effective field derived from the H$\beta$ line was $B_e = 9800 \pm 1100$ G. Thus, the lowest magnetic fields detectable with the SP−124 spectrograph using spectra with signal-to-noise ratios $\approx 100$ are about 1 kG.

Table 2 presents our magnetic-field measurements obtained in this observing mode. The columns contain the same data as in Table 1, except for column 2, which lists the number of exposures instead of the exposure time. The typical exposure time was 10–20 min. It is obvious that the typical measurement accuracy is comparable to the accuracy of measurements carried out with higher spectral resolution and is slightly lower only for the brightest objects (brighter than $12–13^m$). Thus, the SP-124 observations enabled us to enlarge the sample of white dwarfs to objects even weaker than $15^m$ and to study the magnetic properties of low-temperature white dwarfs (see Section 5).

## 4. RESULTS

Our white-dwarf magnetic-field measurements are summarized in Table 3. Magnetic-field estimates obtained using the hydrogen-line magnetometer and photoelectric detector [11] are labeled "HM" in the third column. The remaining observations were spectroscopic (SP). This table is complete except for results for several objects with uncertain magnetic-field estimates that require additional measurements.

Figure 2 shows the distribution of errors in our data compared with the data of Schmidt and Smith [13],

derived from similar observations. The histogram indicates the number of objects with magnetic-field measurements having a given standard observational error $\sigma$, normalized to the total number of stars in each sample. The data of [13] represent the most complete list of magnetic-field observations of white dwarfs with sub-megagauss precision, and these observations are also the most homogeneous. The error distribution for our sample has two maxima. The first is at 3–5 kG and is produced mainly by the MSS and SP-124 observations. The second maximum is at 13–15 kG and is due to our earlier observations with the hydrogen-line magnetometer. The observations of Schmidt and Smith [13] display only one maximum, at 7–9 kG. The white dwarfs of both samples cover the same range of magnitudes. We conclude that our spectroscopic-mode data are the most accurate, and represent fundamentally new observational material. Let us discuss some of the white dwarfs listed in Table 3 in more detail.

### *WD 0413–077 (40 Eri B)*

Searches for the magnetic field of this very bright white dwarf have been carried out in a number of studies [4, 13, 24]. No fields were detected at the level of several kiloGauss. Our later, more accurate observations [14] suggested the presence of an effective magnetic field that varies with time. Subsequent observations have confirmed this result [25]. The time variability of the field and the magnetic curve of this object will be discussed in detail in a separate paper. Here, we will discuss some key estimates of the field strengths obtained with the MSS.

In the MSS observations of 40 Eri B (SP in Table 3), we used a circular-polarization analyzer with nonrotating optical elements. Observations with such an analyzer require additional observations of zero-field standards for removal of systematic errors. We took spectra of standard stars in the course of the observations for this purpose, in the same observational mode, just before and after observations of 40 Eri B.

Usually, bright stars are used as standards, as a rule, cool K giants. The instrumental line shifts in the standard spectra of the opposite polarizations are measured for all spectral lines in the observed wave band. Depending on the complexity of the profiles, the positions of lines in the standard spectra are measured using cross-correlation or Gaussian-analysis methods; the latter are used when the spectral resolution is worse than the intrinsic widths of the spectral lines [14]. The line shifts obtained in this way are linearly interpolated to the times of the program-star exposures.

We selected the best spectra, for which the H$\alpha$ cores were not distorted by cosmic rays, for our measurements. (The traces of cosmic rays in the line cores catastrophically distort the measurements and, regretfully, cannot be removed using mathematical procedures). We analyzed only the central non-LTE part of the H$\alpha$ profiles. The field-strength estimates (Table 1) were obtained by averaging a series of 65 images with exposure times of 3 min. This is the longest (3.5 h) series of continuous observations that has been made. During this time, the magnetic field of

**Table 3.** Estimated white-dwarf magnetic fields

| Object | Method | $B_e$, kG | $\sigma$, kG |
|---|---|---|---|
| WD 0009+501 | SP | −10(max) | 7 |
| – | – | −74(min) | 6 |
| WD 0034–211 | SP | 35 | 13 |
| WD 0101+048 | SP | 0.49 | 2.2 |
| WD 0148+467 | SP | −0.39 | 4.5 |
| WD 0227+050 | SP | −2.6 | 3.3 |
| WD 0232+525 | HM | −11.4 | 16.0 |
| WD 0235+064 | SP | −1.7 | 5 |
| 40 Eri B | SP | 1.8(max) | 0.7 |
| – | SP | −2.8(min) | 0.7 |
| WD 0509+168 | SP | 6.2 | 2.1 |
| WD 0532+414 | SP | 2.5 | 5.0 |
| WD 0627+299 | SP | 15.9 | 13.0 |
| WD 0713+584 | SP | 0.07 | 1.02 |
| WD 0727+482 | SP | No lines | – |
| WD 0939+071 | SP | −3.2 | 4.5 |
| WD 0943+441 | HM | 26.1 | 19.3 |
| WD 1019+637 | SP | 8.2 | 7.5 |
| WD 1026+002 | HM | 5.8 | 15.2 |
| WD 1126+185 | SP | −3.2 | 10.5 |
| WD 1134+300 | HM | −2.8 | 3.9 |
| WD 1247+553 | HM | 9.5 | 15.4 |
| WD 1647+591 | HM | 10.9 | 5.7 |
| WD 1756+827 | SP | 4.2 | 4.5 |
| WD 1953–011 | SP | −28 | 6 |
| WD 2032+248 | SP | −2.7 | 3.1 |
| WD 2326+049 | SP | 0.15 | 2.4 |
| WD 2341+322 | SP | 13.4 | 9.0 |

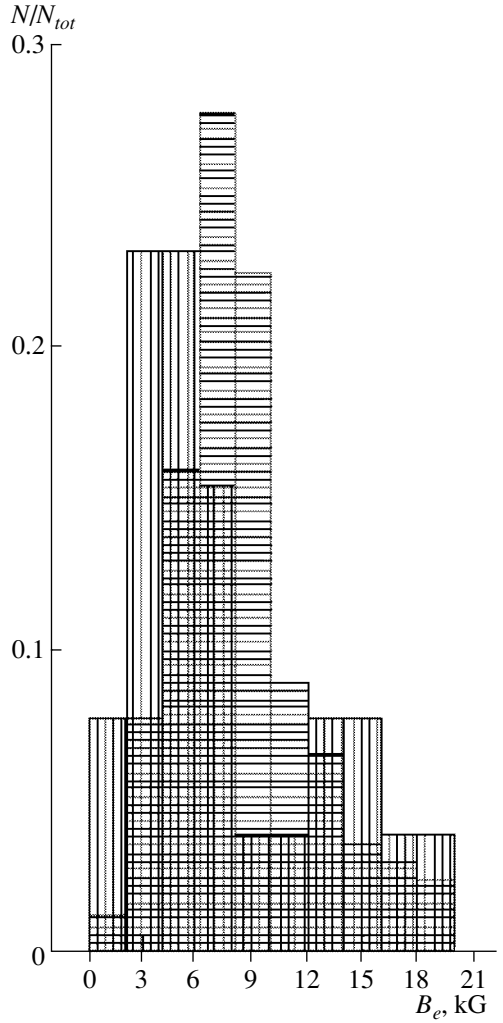


**Fig. 2.** Distributions of standard errors for our sample (vertical shading) and the sample of [13] (horizontal shading).

40 Eri B showed significant variations [14, 15], which can be approximated by a sinusoidal curve with a period of about 4 hours. Confirmation of this periodicity requires long series of additional observations. For this reason, we list in Table 3 only the extreme field strengths that are obtained from the time analysis of this series. Figure 3 shows the behavior of the circular polarization of 40 Eri B when the magnetic field passed through zero and when it was maximum. The circular polarization forms a characteristic profile in the core of the H$\alpha$ line at the magnetic-field maximum (the parameter $V$), whose amplitude we estimate to be $7.5 \pm 2\%$, which corresponds to an effective field strength of approximately 3–4 kG. The difference between this estimate and the estimate given in Table 3 is due to the difference in the methods used to estimate the field. The data in Table 3 are more trustworthy, since they were derived from a statistical analysis of the entire series of observations. The magnetic-field estimates for this object obtained later with the SP-124 spectrograph [25] lie within the limits given in the table and suggest that 40 Eri B is a magnetic white dwarf with a surface field of several kG. We shall discuss the magnetic behavior of 40 Eri B in a separate paper.

### *WD 1953–011*

Schmidt and Smith [13] estimate the effective magnetic field of this star to be $B_e = 15.1 \pm 6.6$ kG, i.e., not appreciable. However, this result identified WD 1953–011 as a candidate magnetic white dwarf. The presence of a strong magnetic field in WD 1953–011 was also suspected by Koester *et al.* [26] in their study of the rotation of white dwarfs based on high-resolution spectroscopy in the vicinity of H$\alpha$. The rotational velocities of normal white dwarfs are small—typical upper limits for $v \sin i$ do not exceed 15 km/s—while the formal rotational velocity of WD 1953–011 is $173 \pm 10$ km/s. The broadening of the non-LTE H$\alpha$ core could be due to Zeeman splitting. Koester *et al.* [26] suspected the presence of Zeeman components. Their estimate of the integrated surface magnetic field $B_s$ based on the broadening of a narrow H$\alpha$ absorption feature is approximately 90 kG. The data in [26] were obtained without a polarization analysis. Such studies can provide estimates of the integrated fields if the Zeeman components can be resolved spectroscopically. However, polarimetric studies are required to reliably establish that an object has a magnetic nature.

Our observations detected the effective magnetic field of WD 1953–011 quite reliably: $B_e = 28 \pm 6$ kG. Figure 4 shows the spectrum of this object and its circular polarization. The parameter $V$ is clearly visible in both the H$\alpha$ and H$\beta$ lines. Thus, we have directly confirmed the magnetic nature of WD 1953–011.

Koester *et al.* [26] have discussed the possibility that there is a considerable systematic difference in the magnetic-field estimates derived from the observed broadening of the non-LTE H$\alpha$ core and from Zeeman polarimetry. The longitudinal (effective) magnetic field varies with the rotational phase within a wide range, depending on the orientation of the dipole angles. The surface magnetic field (absolute value of the integrated-field vector) also varies but within much narrower limits [20]. In the model with a dipolar magnetic field with a random orientation for the dipole axis, the magnitudes of the surface and effective magnetic fields are linked by the statistical relationship $B_s = 3B_e$. In particular, our estimate of $B_e = 28$ kG and the estimate $B_s \sim 90$ kG of Koester *et al.* [26] are consistent with this statistical relation. This provides indirect evidence for the existence of a

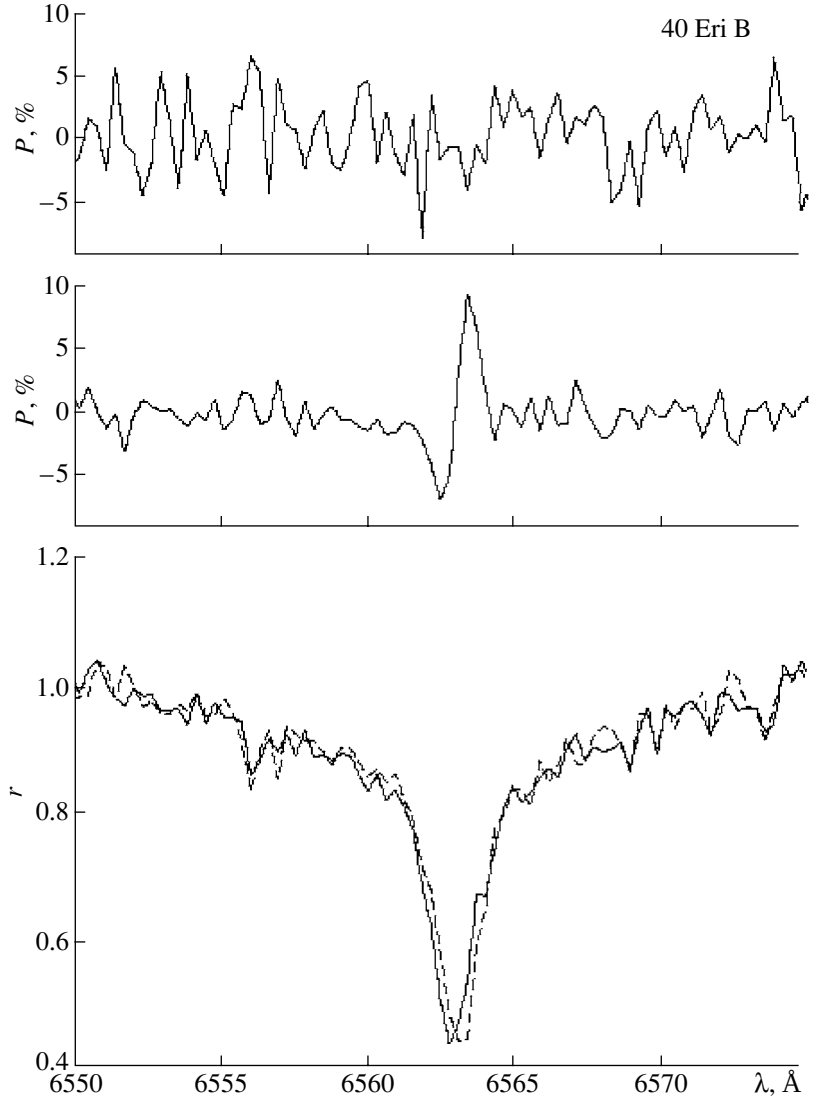


**Fig. 3.** Circular polarization and spectrum of 40 Eri B at the center of the H$\alpha$ profile. The panels show from top to bottom the circular polarization when the magnetic field passed through zero, the circular polarization at the magnetic-field maximum, and the left- and right-circularly polarized spectra at the magnetic-field maximum.

magnetic field with a dominant dipolar component in WD 1953−011, which was directly confirmed in [27].

### *WD 0009+501*

Spectroscopic observations of WD 0009+501 were carried out on September 1–2, 1999, in the spectropolarimetry mode with short exposure times. WD 0009+501 was discovered to be a magnetic white dwarf by Schmidt and Smith [13], who found variations of the magnetic field in the range $B_e = 9$ to $-100$ kG, with an error of $\sigma(B_e) \approx 6$ kG, in 12 observations over 4 nights. It is obvious that the origin of the magnetic-field variations is the star's rotation. Schmidt and Smith [13] constrained the probable rotational period of the dwarf to be between 2 and 20 h.

Our observations of WD 0009+501 consist of 21 consecutive Zeeman spectra. The first 10 spectra were taken with 10-min exposures, and the last 11, with 5-min exposures. The results confirm the presence of a periodically varying magnetic field, with the variation limits given in Table 3. A comparison of our data with the data of Schmidt and Smith [13] yielded a period for the field variations of 1.83 h [25]. A detailed periodogram analysis of the data for this star will be published elsewhere. Figure 5 shows the summed spectrum of WD 0009+501 and the circularly polarized spectrum obtained from the eight spec-

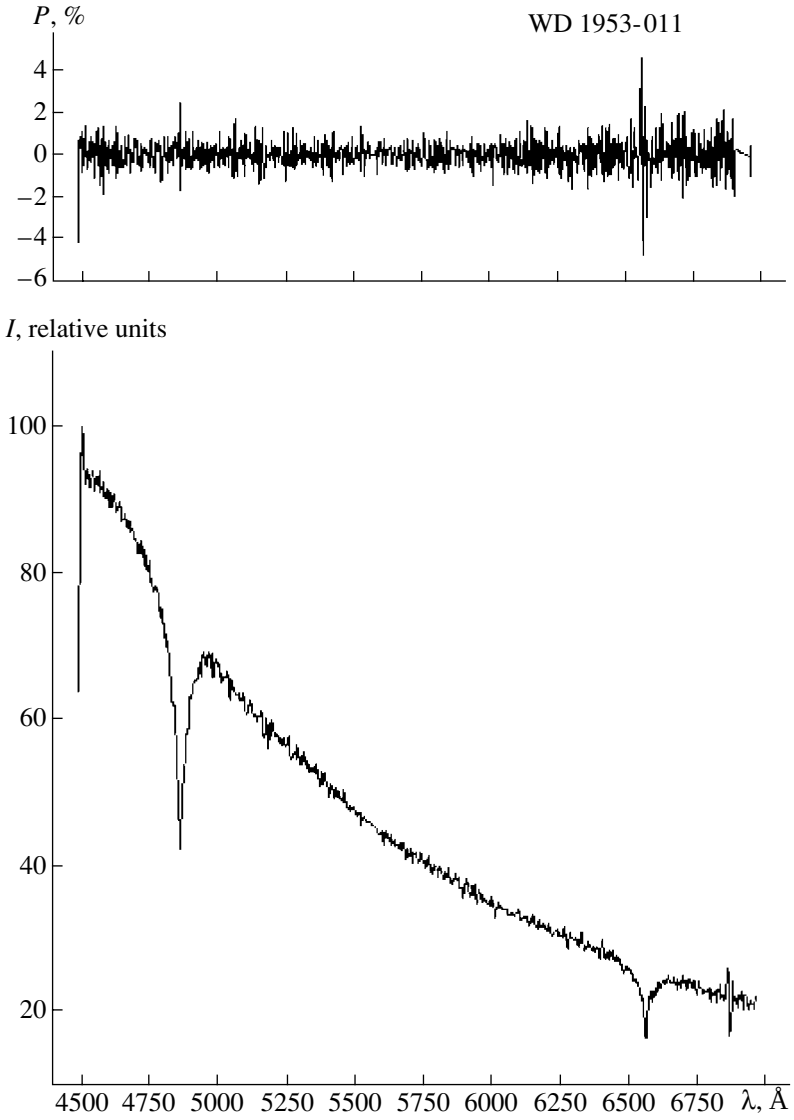


**Fig. 4.** Spectrum (lower panel) and circular polarization (top panel) of the magnetic white dwarf WD 1953-011.

tra corresponding to the maximum magnetic field. Polarization is clearly visible in both H$\alpha$ and H$\beta$.

### *WD 0509+168*

WD 0509+168 is listed in the catalog of McCook and Sion [19] as a cool DA8 white dwarf. Our measurements yield a magnetic field of $6.2 \pm 2.1$ kG. However, a preliminary analysis of its spectrum shows that WD 0509+168 may not be a white dwarf. The spectrum in Fig. 6 is typical of late main-sequence A stars of luminosity class. It is possible that we are dealing with the case of a strongly magnetic star, which is in itself an important fact. We shall continue our studies of this star.

### *WD 0727+482*

As part of our program of studies of the magnetism of cool white dwarfs, we attempted to observe cool DC dwarfs. The presence of weak Balmer lines in the spectra of some of these provides the possibility of measuring the circular polarization either in these lines or in the continuum. Our attempt to obtain such measurements for WD 0727+482 did not yield any significant results. Our program is primarily aimed at measurements of the circular polarization in spectral lines. The spectrum of WD 0727+482 (Fig. 7) shows neither hydrogen lines nor any other spectral features. Since the accuracy of our continuum polarization measurements is low, we are only able to detect fields of the order of 1 MG [4]. Therefore, we are not able at present to place any useful limits on the magnetic field of this white dwarf. However, because of the

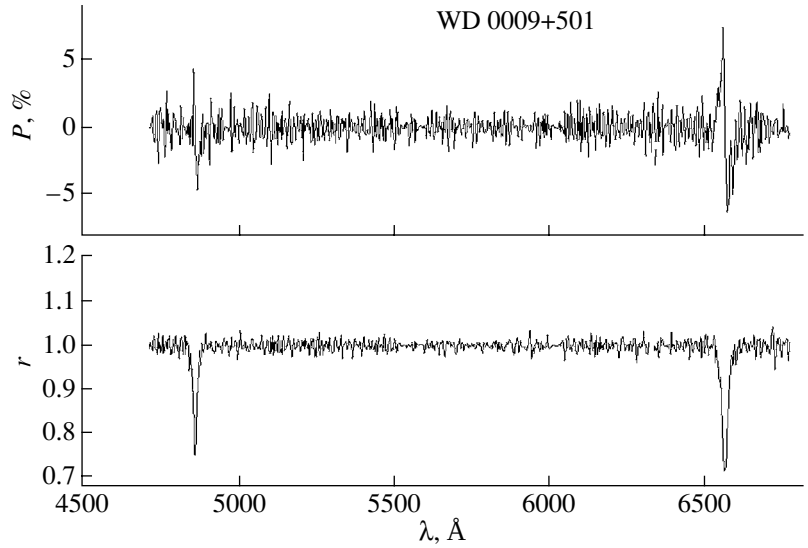


**Fig. 5.** Spectrum (lower panel) and circular polarization (top panel) of the magnetic white dwarf WD 0009+501.

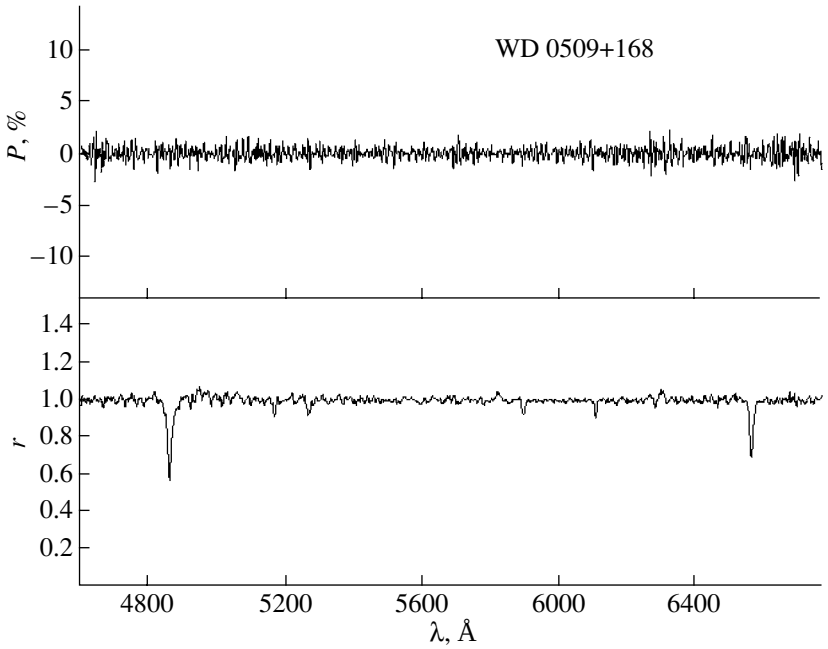


**Fig. 6.** Spectrum (lower panel) and circular polarization (top panel) of WD 0509+168.

importance of studies of the magnetic properties of cool white dwarfs, we intend to carry out additional studies of this particular white dwarf and other objects of the same class.

### *Other Stars*

The magnetic-field estimates for the other stars did not yield any significant results. Figure 8 presents examples of the most typical spectra and circular polarizations of white dwarfs showing non-detections of their fields.

## 5. DISCUSSION

Table 3 shows that, for most objects, the accuracy of our measurements is several kG. However, despite this low detection limit, the existence of regular magnetic fields at a statistically significant level could be established for only a few stars.

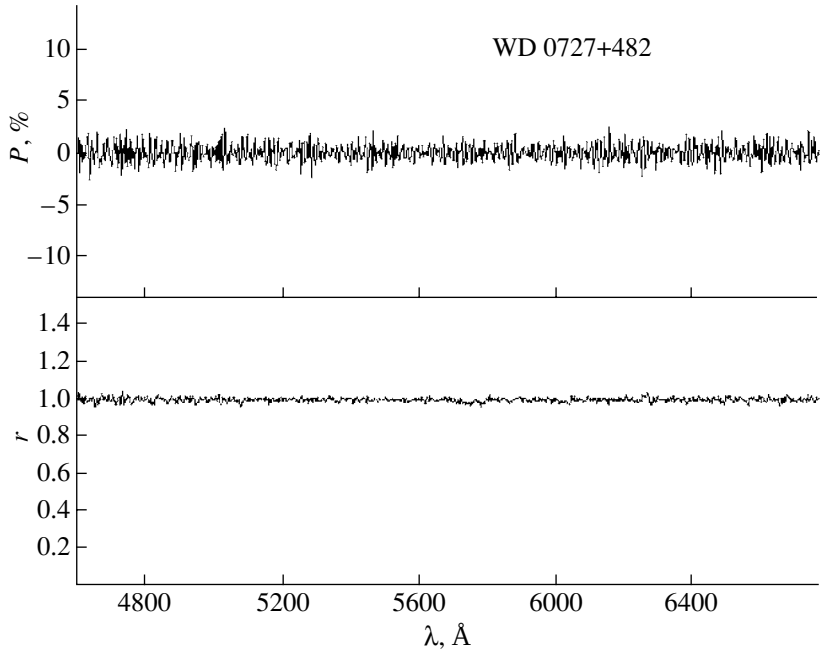


**Fig. 7.** Spectrum (lower panel) and circular polarization (top panel) of the DC white dwarf WD 0727+482.

Together with other observations, these data can be used for statistical estimates of properties such as the magnetic field function [5]. The estimated effective fields $B_e$ correspond to the projections of the integrated surface magnetic-field vectors $B_s$ onto the line of sight. Conclusions concerning the physics of stellar magnetism could be more definite if framed in terms of these surface magnetic fields. The large-scale magnetic-field geometries of white dwarfs are probably dipolar or close to dipolar. Even in a relatively crude approximation, the effective magnetic fields can be related to the surface fields by the expression $B_s \approx 3B_e$ [4]. This expression is not appropriate for any individual star, but its application in statistical studies is quite justified.

Let us discuss the possible increase in the field strengths of white dwarfs with their age (cooling) found earlier [5, 6]. Table 4 presents probable values of the surface magnetic fields derived from our observations, obtained by multiplying the effective field by three (for white dwarfs with detected fields) or six ($2\sigma$) if we have only an upper limit for the field strength. We determined these upper limits by doubling the standard error of the effective field. We also list the effective temperatures for these stars from [28].

The sample of stars discussed here is biased by observational selection effects. The stars were observed under different conditions (individual estimates are mixed with the results of monitoring), they differ in brightness, and the sample itself is incomplete. Nevertheless, our results are consistent with the results of statistical studies of the dependence of the magnetic-field strengths of dwarfs on their temperature. Table 4 shows that white dwarfs with surface fields stronger than 10 kG are found only among cool stars, with temperatures below 10 000 K, although these stars are less numerous and are all relatively weak. No star with a field stronger than 10 kG is found among the hot ($T_{\rm eff} > 10\,000$ K) objects. The fact that the brightest white dwarf, 40 Eri B, has a field of only several kG also provides indirect evidence that the magnetic fields of hot white dwarfs are almost an order of magnitude weaker than those of cool dwarfs [5, 6]. In addition, our observations of 40 Eri B had a deeper detection limit.

The observations of Schmidt and Smith [13] represent a more complete and homogeneous sample of stars. Since cool white dwarfs are several magnitudes fainter than hot white dwarfs, the sample of cool dwarfs available for observations is much smaller than the sample of hot dwarfs. Let us assume that the spatial distributions of white dwarfs with different magnetic and other properties are the same and homogeneous, and limit the sample to white dwarfs with apparent magnitudes no fainter than $15^m$. It then follows from the catalog of McCook and Sion [19] that the number of hydrogen white dwarfs with $T_{\rm eff} \leq 8000$ K (spectral class close to DA6) and $V \leq 15^m$ will be nearly a factor of ten lower than the number of hot dwarfs. The percentage of cool stars in the list of [13] is approximately the same, which provides indirect evidence for the relative homogeneity of their

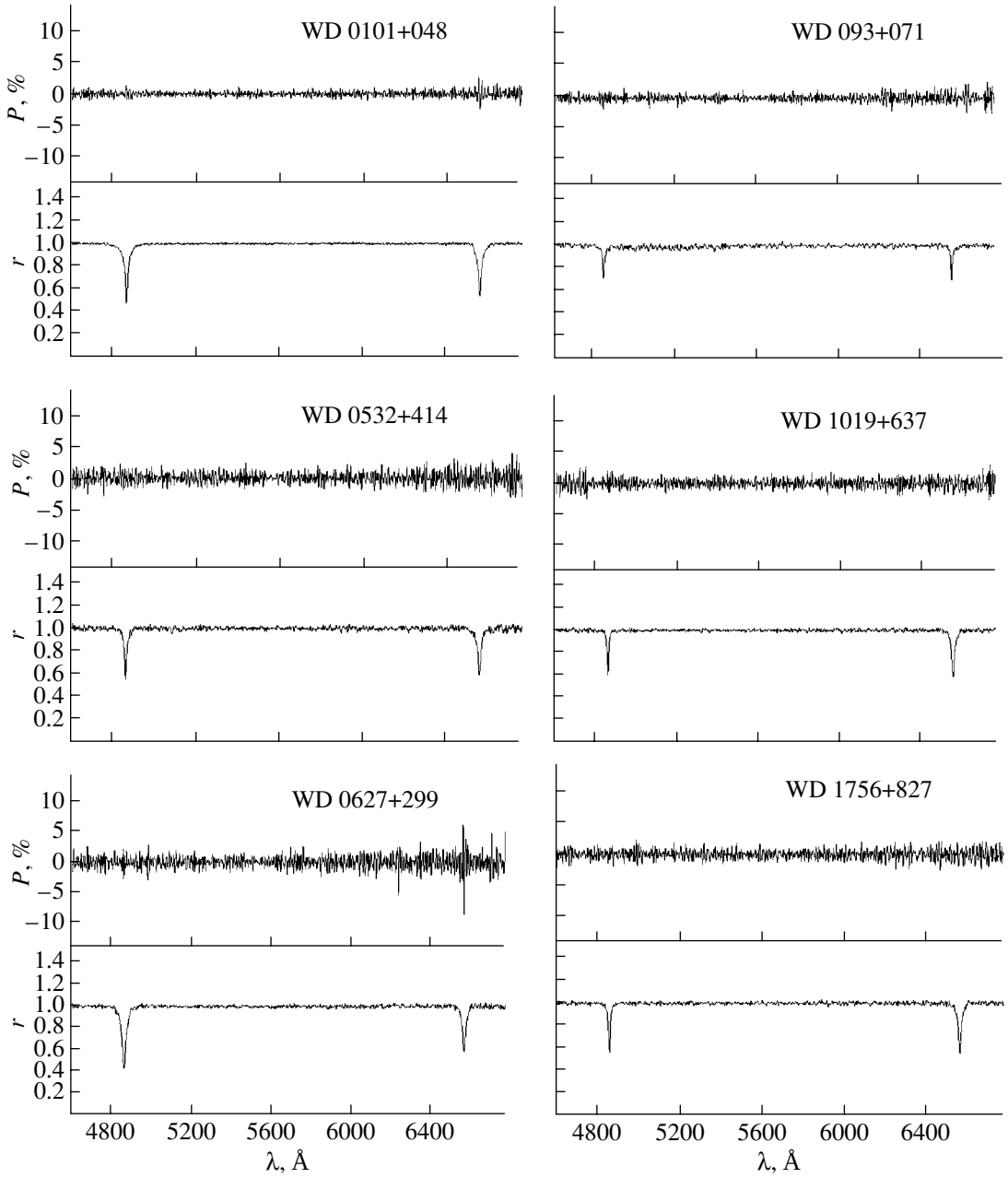


**Fig. 8.** Examples of spectra and circular polarizations of zero-field white dwarfs.

sample. In spite of the fact that most of the stars in the list of [13] have $T_{\rm eff} > 10\,000$ K (and these stars are more easily observed), the relative number of cool magnetic white dwarfs in this list is an order of magnitude higher than the relative number of hot magnetic dwarfs.

In 2002, we initiated a series of observations of white dwarfs using a special new polarimeter [29], in order to confirm the inferred evolution of the white-dwarf magnetic fields and investigate this evolution statistically. The new polarimeter is expected to decrease the magnetic-field detection limit by a factor of three for bright stars ($V \leq 13^m$) and by a factor of six for weak stars ($V \leq 16^m$), which will be very important for observations of cool dwarfs. We hope that this will enable us to detect magnetic fields in most of the stars considered in the present paper.

In addition, we plan to begin linear-polarization measurements of Zeeman components, which will enable us to undertake systematic studies of the magnetic-field geometries of our program stars. Knowledge of the large-scale magnetic-field geometries of white dwarfs with different temperatures will

**Table 4.** Surface magnetic fields and temperatures

| Object | $B_s$, kG | SP | $T_{\rm eff}$, K |
|---|---|---|---|
| WD 0009+501 | ∼200 | DA8 | 6600 |
| WD 0034−211 | <80 | DA7 | 7100 |
| WD 0101+048 | <13 | DA6 | 7800(?) |
| WD 0148+467 | <30 | DA3.5 | 15 200 |
| WD 0227+050 | <20 | DA3 | 20 300 |
| WD 0232+525 | <100 | DAZQO1 | 21 400 |
| WD 0235+064 | <30 | DA8 | 6900 |
| WD 0413-077 | ∼8 | DA3-4 | 17 000 |
| WD 0532+414 | <30 | DA7 | 7100 |
| WD 0627+299 | <80 | DA | >10 000 |
| WD 0713+584 | <6 | DA4 | 16 200 |
| WD 0939+071 | <30 | DA7 | 7200 |
| WD 0943+441 | <120 | DA3 | 15 100 |
| WD 1019+637 | <45 | DA7 | 6900 |
| WD 1026+002 | <90 | DA3 | >10 000 |
| WD 1126+185 | <60 | DC8 | 6000 |
| WD 1134+300 | <23 | DA3 | 21 500 |
| WD 1247+553 | <90 | DA3 | 19 700 |
| WD 1647+591 | <35 | DAv4 | 13 600 |
| WD 1756+827 | <30 | DA7 | 6700 |
| WD 1953−011 | ∼80−90 | DA6 | 7400 |
| WD 2032+248 | <19 | DA3 | 21 100 |
| WD 2326+049 | <14 | DAv4 | 13 800 |
| WD 2341+322 | <50 | DA4 | 13 100 |

make it possible to draw more definite conclusions about the nature of the magnetism of these objects.

## 6. ACKNOWLEDGMENTS

The authors are grateful to E.A. Barsukova for help with the observations. This work was supported by the Russian Foundation for Basic Research (project code 01-02-16808) and the State Science and Technology Program "Astronomy" (section 1102).

## REFERENCES

1. C. E. Wendell, H. M. Van Horn, and D. Sargent, Astrophys. J. **313**, 284 (1987).
2. A. G. Muslimov, H. M. Van Horn, and M. A. Wood, Astrophys. J. **442**, 758 (1995).
3. J. Liebert and E. M. Sion, Astrophys. Lett. **20**, 53 (1979).
4. J. R. P. Angel, E. F. Borra, and J. D. Landstreet, Astrophys. J., Suppl. Ser. **20**, 191 (1981).
5. S. Fabrika and G. Valyavin, in *11th European Workshop on White Dwarfs*, ASP Conf. Ser. **169**, Ed. by J.-E. Solheim and E. G. Meistas (Astronomical Society of the Pacific, San Francisco, 1999), p. 214.
6. G. Valyavin and S. Fabrika, in *11th European Workshop on White Dwarfs*, ASP Conf. Ser. **169**, Ed. by J.-E. Solheim and E. G. Meistas (Astronomical Society of the Pacific, San Francisco, 1999), p. 206.
7. V. G. Shtol', Izv. Spets. Astrofiz. Obs. **33**, 176 (1991).
8. V. G. Shtol', Izv. Spets. Astrofiz. Obs. **35**, 114 (1993).
9. V. D. Bychkov, S. N. Fabrika, and V. G. Shtol', Pis'ma Astron. Zh. **17**, 43 (1991) [Sov. Astron. Lett. **17**, 19 (1991)].
10. V. G. Shtol', G. G. Valyavin, S. N. Fabrika, *et al.*, Pis'ma Astron. Zh. **23**, 53 (1997) [Astron. Lett. **23**, 48 (1997)].
11. S. N. Fabrika, V. G. Shtol', G. G. Valyavin, and V. D. Bychkov, Pis'ma Astron. Zh. **23**, 47 (1997) [Astron. Lett. **23**, 43 (1997)].
12. Yu. V. Glagolevskiĭ, Doctoral Dissertation (Spets. Astrofiz. Obs., Nizhniĭ Arkhyz, 1988).
13. G. D. Schmidt and P. S. Smith, Astrophys. J. **448**, 305 (1995).
14. G. G. Valyavin, D. N. Monin, T. E. Burlakova, S. N. Fabrika, and V. D. Bychkov, in *Stellar magnetic fields*, Ed. by Yu. V. Glagolevskij and I. I. Romanyuk (Nauka, Moscow, 1997), p. 127.
15. S. Fabrika and G. Valyavin, in *11th European Workshop on White Dwarfs*, ASP Conf. Ser. **169**, Ed. by J.-E. Solheim and E. G. Meistas (Astronomical Society of the Pacific, San Francisco 1999), p. 225.
16. I. D. Najdenov and V. E. Panchuk, Bull. Spets. Astrofiz. Obs. **41**, 143 (1996).
17. V. E. Panchuk, SAO Report No. 20 (Spets. Astrofiz. Obs., Nizhniĭ Arkhyz, 1997).
18. C. A. Pilachovski and R. W. Milkey, Publ. Astron. Soc. Pac. **99**, 836 (1987).
19. G. P. McCook and E. M. Sion, Astrophys. J., Suppl. Ser. **121**, 1 (1999).
20. D. W. N. Stibbs, Mon. Not. R. Astron. Soc. **110**, 395 (1950).
21. G. Mathys and S. Hubrig, Astron. Astrophys. **124**, 475 (1997).
22. D. N. Monin, SAO Report No. 31 (Spets. Astrofiz. Obs., Nizhniĭ Arkhyz, 1997).
23. V. D. Bychkov, S. N. Fabrika, D. N. Monin, and G. G. Valyavin, *Magnetic Fields of Chemically Peculiar and Related Stars*, Ed. by Yu. V. Glagolevskij and I. I. Romanyuk (Moscow, 2000), p. 258.
24. L. J. R. P. Angel and J. D. Landstreet, Astrophys. J. **160**, L147 (1970).

25. S. N. Fabrika, G. G. Valyavin, T. E. Burlakova, *et al.*, *Magnetic Fields of Chemically Peculiar and Related Stars*, Ed. by Yu. V. Glagolevskij and I. I. Romanyuk (Moscow, 2000), p. 218.
26. D. Koester, S. Dreizler, V. Weidemann, and N. F. Allard, Astron. Astrophys. **338**, 612 (1998).
27. P. F. L. Maxted, L. Ferrario, T. R. Marsh, and D. T. Wickramasinghe, Mon. Not. R. Astron. Soc. **315L**, 41 (2000).
28. G. G. Valyavin and S. N. Fabrika, Bull. Spets. Astrofiz. Obs. **45**, 69 (1998).
29. I. D. Naydenov, G. G. Valyavin, S. N. Fabrika, *et al.*, Bull. Spets. Astrofiz. Obs. **53**, 124 (2002).

*Translated by L. Yungel'son*

*Astronomy Reports, Vol. 47, No. 7, 2003, pp. 600–612. Translated from Astronomicheskiĭ Zhurnal, Vol. 80, No. 7, 2003, pp. 652–664.*


# The Formation of Millisecond Radio Pulsars in Close Binary Systems

**A. V. Tutukov and A. V. Fedorova**

*Institute of Astronomy, Russian Academy of Sciences, ul. Pyatnitskaya 48, Moscow, 109017 Russia*

Received October 17, 2002; in final form, January 10, 2003

**Abstract**—An analysis of the basic parameters of a sample of radio and X-ray pulsars that are members of close binary systems is used to separate them into several families according to the nature of the pulsar companions and the previous evolution of the systems. To quantitatively describe the main parameters of close binaries containing neutron stars, we have performed numerical modeling of their evolution. The main driving forces of the evolution of these systems are the nuclear evolution of the donor, the magnetically coupled and radiation-induced stellar winds of the donor, and gravitational-wave radiation. We have considered donors that are low-mass stars in various stages of their evolution, nondegenerate helium stars, and degenerate stars. The systems studied are either the products of the normal evolution of close binaries with large initial component-mass ratios or result from inelastic collisions of old neutron stars with single and binary low-mass, main-sequence stars in the dense cores of globular clusters. The formation of single millisecond pulsars requires either the dynamical disruption of a low-mass ($\lesssim 0.1 M_\odot$) donor or its complete evaporation under the action of the X-ray radiation of the millisecond pulsar. The observed properties of binary radio pulsars with eccentric orbits combined with the bimodal spatial-velocity distribution of single radio pulsars suggest that it may be possible to explain the observed rotational and spatial motions of all radio pulsars as a result of their formation in close binaries. In this case, neutron stars formed from massive single stars or the components of massive wide binaries probably cannot acquire the high spatial velocities or rapid rotation rates that are required for the birth of a radio pulsar.


## 1. INTRODUCTION

The rapid rotation of single radio pulsars is usually considered to be a natural result of the collapse of the rapidly rotating core of the supernova precursor. However, two questions remain unanswered in this case. First, conservation of the angular momentum of the core of a typical massive star from the main-sequence (MS) stage to the formation of a neutron star (NS) would result in very short rotational periods for young radio pulsars ($P_\mathrm{p} \leq 10^{-4}$ s), which are not observed. This means that, in order to explain the observed initial rotational periods of radio pulsars, the core of the massive star must lose about 99.9% of its initial angular momentum. Second, current radio-pulsar statistics yield birth rates of $\sim 0.006$/yr [1–3], much lower than the occurrence rate of the supernovae that produce them, $\sim 0.03$/yr. The low birth rate of radio pulsars is underlined by their low incidence in observed supernova remnants: only 10 of 200 remnants contain radio pulsars [4]. This difference (a factor of 20) can be explained partially by the collimation of the pulsar's radiation and, probably, partially by a lower birth rate of pulsars compared to the occurrence rate of supernovae. Evidence for the presence of neutron stars in supernova remnants without radio pulsars is provided by their optical, X-ray, and gamma-ray radiation [5]. It is known from observations that millisecond pulsars and X-ray pulsars [6] are components of close binaries or very probable products of the evolution of such binaries. Hence, in this case, rapid rotation is a result of accretion.

The high spatial velocities of single radio pulsars are usually explained by the "kick" that accompanies the birth of the pulsar [7, 8]. However, when observational selection effects are taken into account, it becomes clear that the velocity distribution of pulsars is bimodal [9, 10]. About half of pulsars form with velocities lower than 100 km/s, while the rest form with velocities of 300–500 km/s. This bimodal distribution can be explained in a natural way by the decay of close binary systems after the second supernova explosion in the system [11]. The absence of pulsars with velocities typical of massive stars (10 km/s) probably means that single stars or the components of wide massive binaries do not produce radio pulsars in SN II explosions. A possible reason for this is that the rotation of the cores of the supernova precursors is too slow due to braking by extended, and hence slowly rotating, envelopes. The collapse of such cores produces neutron stars with rotational periods exceeding $\sim 10$ s, precluding the formation of a radio pulsar.

To summarize, it is possible to explain the high

1063-7729/03/4707-0600$24.00 

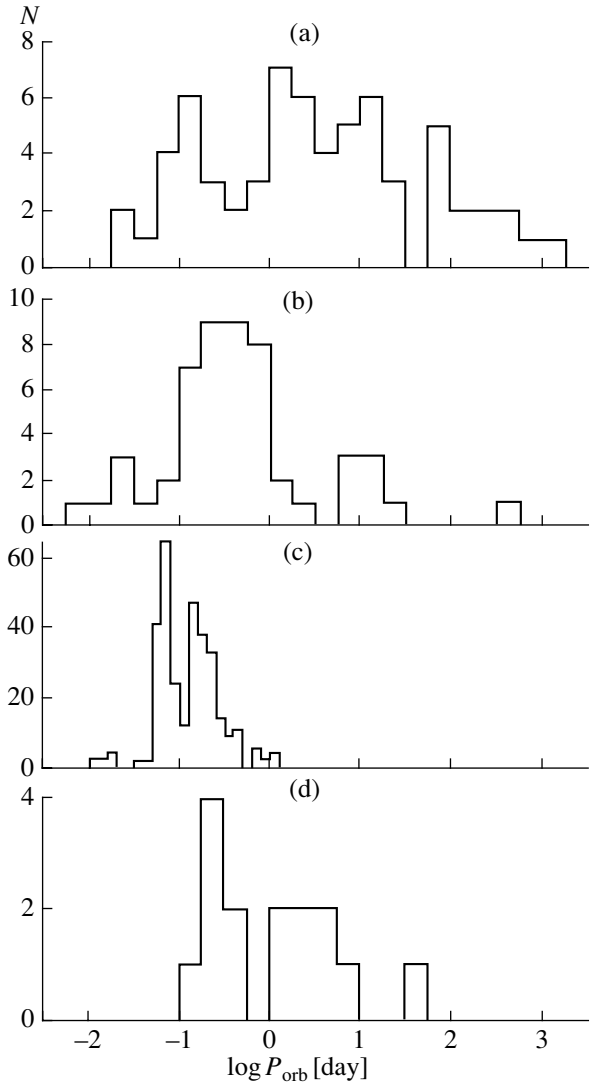


**Fig. 1.** Distribution of orbital periods of radio pulsars in (a) binaries with $e \approx 0$, (b) low-mass X-ray binaries, (c) cataclysmic variables, and (d) black-hole binaries. The data are taken from [8, 15–30].

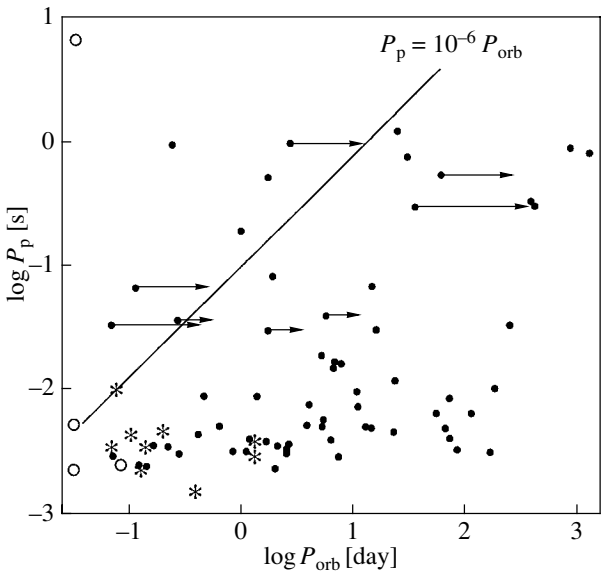


**Fig. 2.** Distribution of binary radio pulsars in the log(orbital period)—log(pulsar rotational period) diagram. Shown are data for binary radio pulsars (circles), eclipsing millisecond pulsars (asterisks), and X-ray binaries (open circles). Systems with nonzero orbital eccentricities are marked by arrows. The line shows the dependence of the initial rotational period of the pulsar on the orbital period of the binary before the formation of a neutron star. The data are taken from [8, 15–30].

spatial and rotational velocities of radio pulsars using models in which these properties are associated with the evolution of close binary stars [9]. It is interesting that, as a rule, due to their high spatial velocities, young radio pulsars leave their parent globular clusters, and a significant fraction even leave their parent galaxies. Neutron stars that are the evolutionary products of single stars or the components of wide binaries have low velocities and remain in their parent clusters. Later, due to double [12] and triple [13] stellar collisions, they may form close pairs, spin up, and become millisecond pulsars. Some fraction of millisecond pulsars in the disk of the Galaxy form from primordial massive close binaries with large initial component-mass ratios ($\gtrsim 10$) [11, 14]. The immediate precursors of millisecond pulsars are X-ray binaries with neutron-star accretors and low-mass donors ($\leq M_\odot$), making possible a long X-ray phase and efficient spin-up of the old neutron star.

Let us consider the basic orbital parameters of observed radio pulsars in close binary systems. Figure 1a shows the distribution of orbital periods $P_{orb}$ of known binary radio pulsars [8, 15–30]. Most of these objects are millisecond pulsars (Fig. 2). Although the statistics remain poor, we can distinguish three groups of objects in Figs. 1a and 2: those with orbital periods of 0.1–1 day, 1–30 days, and 60–1000 days. The basis for this separation can be found in Figs. 3 and 4. The distribution of X-ray binaries with low-mass donors (Fig. 1b) follows the distribution of binary millisecond pulsars with short orbital periods. This seems to be natural for the immediate precursors of the latter objects. The kinship is underlined by the coincidence of the ranges of the observed rotational periods of radio pulsars [1] and of neutron stars in X-ray binaries [31]: 0.002–6 s. The paucity of X-ray binaries with long orbital periods is probably a consequence of the rapid decrease of their lifetimes with increasing orbital period [14].

X-ray binaries with black holes and neutron stars have similar orbital-period distributions. The minimum orbital periods of these systems are $\sim 3$ h. This

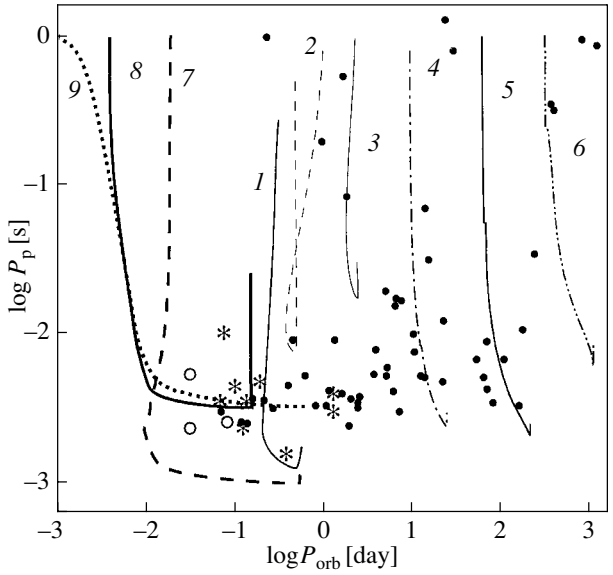


**Fig. 3.** Distribution of binary radio pulsars and theoretical tracks of binaries in the log(orbital period)—log(pulsar rotational period) diagram. Notation is as in Fig. 2. The numbers along the tracks correspond to those in the table. The data are taken from [8, 15–30].

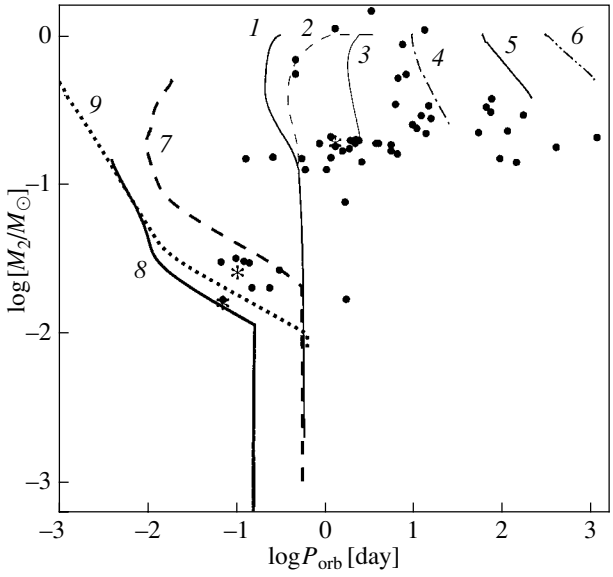


**Fig. 4.** Distribution of binary radio pulsars and theoretical tracks of binaries in the log(orbital period)—log(donor mass) diagram. Notation is as in Fig. 2. The numbers along the tracks correspond to those in the table. The data are taken from [8, 15–30].

is a consequence of the dominant influence of the induced stellar wind and the magnetically coupled stellar wind on their evolution [14, 32]. Cataclysmic variables with orbital periods below 2 h (Fig. 1c) evolve under the influence of gravitational-wave radiation [33]. The reason for the paucity of cataclysmic

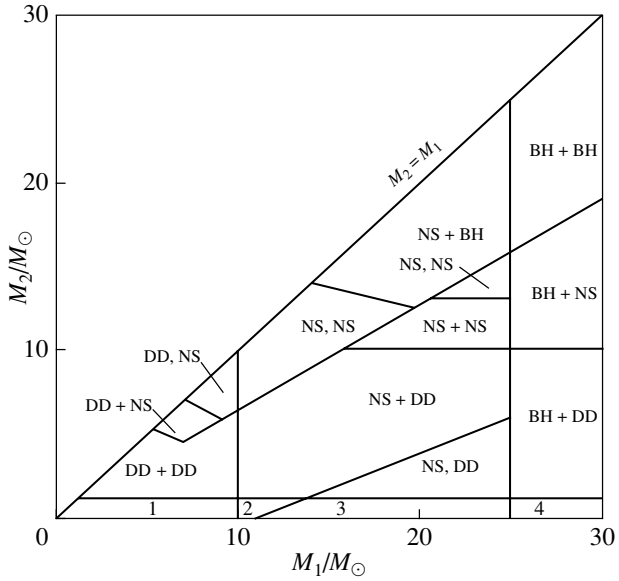


**Fig. 5.** Regions populated by different final products of the evolution of close binary stars with different initial masses in the (initial primary mass)—(initial secondary mass) diagram. The binary components include main-sequence stars (MS), neutron stars (NS), degenerate dwarfs (DD), and black holes (BH). The regions marked by the numbers 1, 2, 3, and 4 correspond to DD + MS, NS + MS, (NS, MS), and BH + MS systems.

variables with orbital periods longer than one day is evident: it is due to the rareness of degenerate dwarfs with masses higher than 1.2 $M_\odot$, which is a necessary condition for stable mass exchange in semidetached systems with subgiant donors of the minimum possible mass $\sim 0.9 M_\odot$. Comparison of the orbital-period distributions of close binary systems of various types provides additional information for the analysis of the driving forces of the evolution of systems with different orbital periods.

In the present study, we attempt to explain the observed rotational and spatial velocities of radio pulsars as consequences of their formation during the evolution of close binaries of various types. Then, high spatial velocities arise only if massive close binaries are disrupted when their components explode as supernovae. The rotation of single pulsars is probably the result of the synchronization of the axial rotation of the supernova precursor with the orbital motion in close binaries. The rapid rotation of millisecond pulsars results from a long ($\sim 10^7$ yr) stage of accretion from a close, low-mass companion. As we shall show below, a considerable fraction of millisecond pulsars are single because their main-sequence companions with masses $\leq 0.1 M_\odot$ or degenerate companions with masses $\leq 0.02 M_\odot$ are tidally disrupted or evaporated by the radiation of the neutron star.

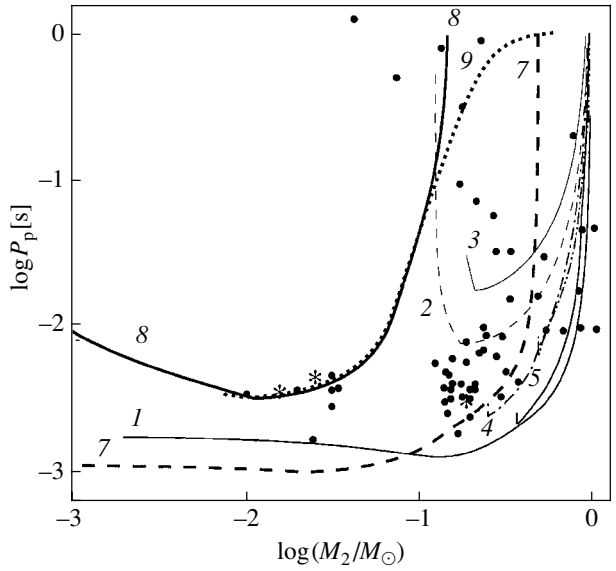


**Fig. 6.** Distribution of binary radio pulsars and theoretical tracks of binaries in the log(donor mass)—log(rotational period) diagram. Notation is as in Fig. 2. The numbers along the tracks correspond to those in the table. The data are taken from [8, 15–30].

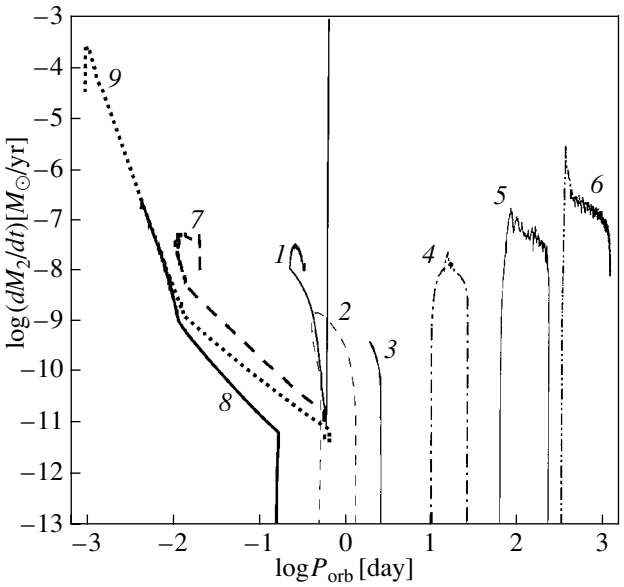


**Fig. 7.** Theoretical tracks of binary systems in the log(orbital period)—log(donor mass-loss rate) diagram. The numbers along the tracks correspond to those in the table.

## 2. ANALYSIS OF THE EVOLUTION OF CLOSE BINARIES WITH NEUTRON-STAR COMPONENTS

After the exhaustion of the nuclear fuel in the interiors of stars, their evolution ends in the formation of a degenerate dwarf (if the initial mass is $M_0 < 10M_\odot$), neutron star (if $10M_\odot < M_0 < 25M_\odot$), or black hole (if $M_0 > 25M_\odot$) [34]. To determine the final states of close binaries, we must specify the dependence of the mass of the remnant of a component on its initial mass. This dependence is $M_d = 0.6(M_0/M_\odot)^{0.4}$ for degenerate dwarfs, $1.4M_\odot$ for neutron stars, and $0.05(M_0/M_\odot)^{1.4}$ for black holes [34]. The condition for disruption of a binary with a circular orbit by a supernova explosion is

$$\delta M > M_R + M_2, \qquad (1)$$

where $\delta M$ is the amount of mass lost in the explosion of a helium supernova with mass $0.1(M_0/M_\odot)^{1.4}$ [35], $M_R$ is the mass of the remnant (neutron star or black hole), and $M_2$ is the mass of the companion to the supernova.

It is still poorly known to what extent mass exchange between the components of close binaries is nonconservative. Therefore, for our estimates of the nature of the final products of the evolution of close binaries, we shall assume for the sake of definitiveness that the initial critical component-mass ratio in the first stage of mass exchange is $q_0 = M_2/M_1 = 0.64$. We will consider systems with larger initial $q$ values to be conservative, while systems with lower initial $q$ values are nonconservative; i.e., $M_2 = \text{const}$ in the first mass exchange. These assumptions enable us to define the nature of the final products of the evolution of close binaries with various initial masses (Fig. 5). A neutron star can be a component of several types of final close binary: DD + NS, NS + DD, NS + NS, BH + NS, NS + BH, and NS + MS (The notation used here is explained in the caption to Fig. 5). The Galactic birth rate of these systems is $\sim 10^{-3}$/yr, while the total birth rate of neutron stars is $\sim 0.03$/yr [36]. Let us consider the evolution of these systems numerically.

We estimate the rotational velocity of an old neutron star with a weak magnetic field using the equation

$$dP_p/dt = \alpha 10^{-16} P_p^{1.6} - 10^{-12} P_p^2 \dot{M}_{-8}, \qquad (2)$$

where $P_p$ is the rotational period of the neutron star and $\dot{M}_{-8}$ is the accretion rate in $10^{-8}M_\odot$/yr. The first term is an analytic expression for the observed correlation of the rate of change of the spindown rotational velocities of radio pulsars with the magnitudes of these velocities [1, 8]. The parameter $\alpha$ is introduced because of the considerable dispersion of this correlation. The second term describes the acceleration of the rotation of a rigidly rotating neutron star that is accreting at its equator.

Practically all radio pulsars spin down with time, while neutron stars in X-ray binaries spin up. To

interpret the results of the computations, we will assume that decelerating neutron stars are radio pulsars, while accelerating neutron stars are X-ray pulsars. Due to the weak magnetic fields of old neutron stars, the detection of periodic pulsations of their X-ray emission is difficult and millisecond X-ray pulsars are rare. The boundary between X-ray and radio pulsars corresponds to $\dot{M}_{-8} = \alpha 10^{-4} P_{\rm p}^{-0.4}$ [see (2)]. Because the observed values are $P_{\rm p} \approx 0.002$–$6$ s, the limiting $\dot{M} \sim 10^{-12} - 10^{-11} M_\odot$/yr. Thus, some fraction of radio pulsars in binaries can be accreting objects. One such pulsar is known: SAXJ 1808.4-3658, with $P_{\rm p} = 0.0025$ s and $P_{\rm orb} \sim 2$ h [37]. In particular, this means that the companions of radio pulsars can be extended and can even fill their Roche lobes if the rate of mass exchange is sufficiently low. Therefore, a substantial fraction of millisecond pulsars with short orbital periods (Fig. 2) are eclipsing [21, 24, 25].

Let us now consider the formation of radio pulsars, using modern scenarios for the evolution of close binaries and numerical models. This analysis is conveniently done in terms of $P_{\rm p}$, $P_{\rm orb}$, $M_2$, and $\dot{M}$ (Figs. 2–4, 6, 7). A special family in Fig. 2 is formed by radio pulsars in close binaries with high orbital eccentricities. It is evident that the observed pulsars are produced in the last (in the case of NS + NS or BH + NS systems; Fig. 5) or only (in the case of DD + NS systems) supernova explosion in the close binary systems. The orbital eccentricity is a measure of the mass lost in the supernova explosion: $e = \delta M/(M_R + M_2)$ [see (1)]. Three systems in Fig. 2 have low orbital eccentricities, $e = 0.21$–$0.27$, in contrast to the remaining systems, with $e = 0.6$–$0.8$. These low eccentricities are due to either a small mass loss ($\sim 0.7 M_\odot$ for the pulsar B1534+12 [38]), or to the combination of a large mass (3–10 $M_\odot$) for the companion to the radio pulsar and a typical mass (1.1–3 $M_\odot$) for the envelope of the supernova exploding in the close binary [39]. High companion masses provide evidence for the presence of black holes in these systems [34], whose Galactic birth rate is $\sim 5 \times 10^{-4}$/yr [36]. In the latter case, additional arguments are required to prove this hypothesis, such as studies of the evolution of the orbital periods. The very low mass of the envelope of the supernova that produced pulsar B1534+12 argues in favor of reducing the minimum initial mass for the supernova precursors from the commonly accepted value $10 M_\odot$ to $8.5 M_\odot$. Judging from their high birth rate of $1.2 \times 10^{-3}$/yr [36], systems with high orbital eccentricities probably belong mainly to the DD + NS family; however, they may also be encountered among NS + NS systems, as is suggested by the binary neutron star PSR 1916+16, whose components have masses of 1.44 $M_\odot$ and 1.39 $M_\odot$ [40].

Let us continue our analysis of binary pulsars with nonzero orbital eccentricities. If we assume that the axial rotation and the orbital motion of a compact helium supernova precursor are synchronized, we can estimate the rotational periods of young pulsars [11, Fig. 9]. Let us assume on the basis of computations of the evolution of massive stars that a neutron star is the product of the collapse of the degenerate core of a supernova precursor with a radius of $\sim 10^9$ cm [35]. The conservation of angular momentum during the collapse implies the relation $P_{\rm p} = 10^{-6} P_{\rm orb}$, shown in Fig. 2. It is important that the orbital period in this relation is the period of the system prior to the supernova explosion, and the orbital eccentricity enables us to recover this value, as is shown in Fig. 2. The agreement of the rotational periods of pulsars predicted by this relation with the observed periods is evident.

Let us estimate the limiting values for the semimajor orbital axes and, hence, of the orbital periods of close binaries with neutron-star components. It is clear that DD + NS binaries are the widest among systems with eccentric orbits (Fig. 5). Assuming that the mass of the neutron-star precursor at the moment of Roche-lobe overflow is $10 M_\odot$ ($M_R = 2.5 M_\odot$), the mass of the degenerate dwarf is $1.4 M_\odot$, and the maximum semimajor orbital axis for close binaries is $\sim 2500 R_\odot$, we estimate that the orbital period of the system after the common-envelope stage is close to 56 days (Fig. 2). The closest DD + NS and NS + NS systems form from helium stars with radii $R_{\rm He} = 0.2 (M_{\rm He}/M_\odot)^{0.6}$ [35]. Because the minimum masses of the exploding helium stars are close to $\sim 2.5 M_\odot$ and the masses of their companions are $\sim 1 M_\odot$, the minimum orbital periods of such systems prior to the supernova explosion are close to 1 h, as indicated in Fig. 2. Note that all currently known radio pulsars with eccentric orbits indeed have orbital periods in the range from 1 h to 60 days.

Most massive binary stars are disrupted by the second supernova explosion in the system. Therefore, the limits for the rotational periods of neutron stars formed in close binaries remain valid for single pulsars. Note that the range of allowed rotational periods of neutron stars formed in close binaries, 0.005–4 s (Fig. 2), agrees with the range of observed periods of single radio pulsars [1, 8], in support of the proposed scenario. Since the range of initial semimajor axes of close-binary orbits covers about 40% of the total range of the semimajor axes of binary orbits, the birth rate of radio pulsars in the Galaxy is close to 0.03/yr [36]. This estimate is comfortably higher than the observational estimate of $\sim 0.006$/yr based on the statistics of young pulsars [1], leaving room for the collimation of the emission of radio pulsars. This

provides hope that these estimates can eventually be brought into agreement.

Figure 2 shows that, in the scenario considered, the shortest possible period of a young radio pulsar is $\sim 0.005$ s. It is interesting that a pulsar with such a short period has a rotational energy of $\sim 10^{51}$ erg. In the presence of a sufficiently strong magnetic field, an appreciable fraction of this energy can be transferred to the envelope, producing a supernova [41]. That is, the magnetorotational mechanism can probably be responsible only for explosions of helium stars (SN Ib,c) in the closest systems. The requirement of very short final orbital periods enables us to estimate the occurrence rate of such events in the Galaxy. If the rotational energy is $10^{50}$–$10^{51}$ erg, the orbital periods should range from 1–3 h (this corresponds to the range of semimajor orbital axes $d\log A \sim 0.3$, with the total range of $A$ for binaries being $d\log A \sim 5$ [42]). It is clear that only a few percent of all supernovae can be produced by magnetorotational explosions. The young neutron stars produced by these explosions should be found among the shortest-period radio pulsars ($P_\mathrm{p} \lesssim 0.03$ s).

Note that the possibility of forming Kerr black holes rotating at the limit of dynamical stability is also related to the collapse of the cores of helium Wolf–Rayet stars in close binaries that are at the lower end of the range of possible component separations. The formation of Kerr black holes is necessary to explain gamma bursters [43]. Two additional circumstances are helpful in forming black holes rotating at the limiting (or shorter) periods: the low ($\sim 10^4$ g/cm$^3$ [35]) density of the matter in the cores of massive supernova precursors and the fact that the radii of black holes are smaller than those of neutron stars. The object GBR 021004 has shown signs of the presence of an expanding gaseous envelope in its vicinity; the velocity of the expansion is 3000 km/s and the mass-loss rate is $\sim 6\times 10^{-5} M_\odot$/yr [44]. Such winds are typical of massive ($\sim 35 M_\odot$) Wolf–Rayet stars, providing observational support for the hypothesis that Kerr black holes are the sources of the gamma-ray outbursts.

Again using Fig. 2, we can now estimate the initial rotational velocity of an old neutron star that has passed through a common-envelope stage in scenarios that result in the formation of (NS, NS), NS + NS, NS + DD, and NS + BH systems. The duration of the common-envelope stage is close to the thermal time scale of the donor, which is about $3\times 10^5 (R/R_\odot)$ yr for massive stars with $L \sim M^2$. If the accretion rate of a neutron star in the common-envelope stage is limited to the Eddington rate, $\sim 10^{-8} M_\odot$/yr, the mass of the accreted matter is $\sim 0.003 R/R_\odot$ and the rotational period of the neutron star is $\sim 0.03 R/R_\odot$ s. The radii of massive hydrogen–helium stars are confined to $3$–$1000 R_\odot$, resulting in $P_\mathrm{p} = 0.1$–$30$ s. Thus, some of the radio pulsars currently observed to be single are probably rejuvenated. Because they formed in disrupted close binaries, they can acquire high (200–1000 km/s) spatial velocities [1, 7, 8, 10], explaining the origin of fast [9, 10] radio pulsars. The products of the last supernova explosion in massive close binary systems become slow pulsars.

If the mass of the secondary is less than $\sim 10 M_\odot$, it becomes a degenerate dwarf. The thermal time scales of such stars are $\sim 3\times 10^7 R_\odot/R(M/M_\odot)^2$ yr, and the rotational periods of the rejuvenated pulsars in these systems are $\sim 0.0004 R/R_\odot (M/M_\odot)^2$ s. For $M = 2M_\odot$ and $R = 10$–$100 R_\odot$, the rotational periods are $P_\mathrm{p} \sim 0.01$–$0.1$ s; such $P_\mathrm{p}$ values are usual for "young" radio pulsars. It is natural that the orbits of NS + DD systems are circular (Figs. 2, 3). To derive more reliable estimates of the orbital and rotational periods of radio pulsars, we must take into account the influence of the neutron star's magnetic field [45] and ensure that the numerical modeling of the evolution of the binaries in common-envelope stages is adequate.

## 3. NUMERICAL MODELING OF THE EVOLUTION OF CLOSE BINARY SYSTEMS CONTAINING OLD NEUTRON STARS AND LOW-MASS ($\lesssim 1 M_\odot$) DONORS

### *3.1. Brief Description of the Method Used to Compute the Evolution of Close Binary Systems*

The method used to compute the evolution of close binary systems taking into account the induced stellar wind (ISW) of the donor and our evolutionary code are described in detail in [14, 32]. We give here only a brief outline.

The ISW arises due to the irradiation of the donor by hard radiation generated during accretion onto the neutron star [14] or the braking of its rotation. Computations have shown that this irradiation leads to evolutionarily significant mass loss by the donor in the form of a stellar wind [14, 32]. As we noted in the previous section, we use the simple numerical model for the evolution of the rotational period of an old neutron star (2). In this model, a neutron star is spun down when the accretion rate is low and spun up when the accretion rate is high. It is important that, in the presence of an ISW, mass exchange becomes possible also for detached systems, when the donor does not fill its Roche lobe. In our computations, we took the main parameter of the model with an ISW—the ratio of the stellar-wind velocity and the escape velocity—to be unity. We have studied the

Parameters of the calculated tracks of close binary systems

| Track number | $(M_2)_0$, $M_\odot$ | $D$ | $(P_{\rm orb})_0$, days | $(P_{\rm orb})_{\rm min}$, days | $(P_{\rm p})_{\rm min}$, ms | $M_{\rm acc}$, $M_\odot$ | $(M_2)_f$, $M_\odot$ | $(M_{\rm He})_f$ | $(P_{\rm orb})_f$, days | $(P_{\rm p})_f$, ms | $t_f$, $10^9$ yr |
|---|---|---|---|---|---|---|---|---|---|---|---|
| 1 | 1.0 | 1.0 | 0.32 | 0.21 | 1.2 | 0.20 | 0.002 | 0.00 | 0.58 | 1.7 | 5.6 |
| 2 | 1.0 | 0.3 | 1.92 | 0.38 | 7.4 | 0.04 | 0.13 | 0.00 | 0.48 | 1121 | 15 |
| 3 | 1.0 | 0.2 | 3.53 | 1.83 | 17.1 | 0.02 | 0.19 | 0.53 | 2.44 | 29.8 | 15 |
| 4 | 1.0 | 0.1 | 9.99 | 9.61 | 2.3 | 0.11 | 0.25 | 0.96 | 25.4 | 2.9 | 15 |
| 5 | 1.0 | 0.03 | 61.2 | 61.2 | 2.1 | 0.12 | 0.37 | 0.99 | 222 | 2.5 | 15 |
| 6 | 1.0 | 0.01 | 316 | 316 | 5.8 | 0.04 | 0.49 | 0.99 | 1137 | 8.6 | 15 |
| 7 | 0.5 | 1.0 | 0.02 | 0.009 | 1.0 | 0.25 | 0.0009 | 1.0 | 0.56 | 1.1 | 2.8 |
| 8 | 0.15 | 1.0 | 0.004 | 0.004 | 3.1 | 0.08 | 0.0004 | 1.0 | 0.15 | 25.2 | 15 |
| 9 | 0.6 | 1.0 | 0.001 | 0.001 | 3.2 | 0.08 | 0.008 | – | 0.63 | 3.3 | 1.0 |

$(M_2)_0$ is the initial donor mass; $D$, the initial ratio of the donor radius and the average radius of the Roche lobe (after the birth of the neutron star); $(P_{\rm orb})_0$, the initial orbital period of the system; $(P_{\rm orb})_{\rm min}$, the minimum orbital period of the system; $(P_{\rm p})_{\rm min}$, the minimum rotational period of the neutron star in the course of the evolution; $M_{\rm acc}$, the mass accreted by the neutron star in the course of the evolution; $(M_2)_f$, the mass of the donor at the end of the track; $(M_{\rm He})_f$, the relative mass of the helium core of the donor at the end of the track; $(P_{\rm orb})_f$, the orbital period of the system at the end of the track; $(P_{\rm p})_f$, the rotational period of the neutron star at the end of the track; and $t_f$, the age of the system at the end of the track. The donor is initially a main-sequence star in tracks 1–6, a nondegenerate helium star in track 7, a degenerate helium dwarf in track 8, and a degenerate carbon–oxygen dwarf in track 9.

dependence of the computation results on the basic parameters in our previous papers [14, 32].

In all the computed tracks, the initial mass of the neutron star was assumed to be $1.4M_\odot$. The computations of a particular track were terminated when the donor was disrupted or evaporated, or when the time elapsed since the formation of the neutron star reached 15 Gyr. The initial rotational period of the neutron star was taken to be $\sim$1 s. The main parameters of the computed tracks are listed in the table. When considering systems with main-sequence donors with masses $\sim 1M_\odot$, we assumed that the donor can fill its Roche lobe to a different extent at the moment of formation of the neutron star, specified by $D$, the initial ratio of the donor radius to the average Roche-lobe radius.

### *3.2. Results of Numerical Modeling of Systems with Main-sequence Donors*

Let us first consider the evolution of systems with low-mass ($\sim 1M_\odot$) donors with solar composition and various $D$ values. The evolution of the system in the space of its four main observed parameters—$P_{\rm orb}$, $P_{\rm p}$, $M_2$, and $\dot{M}_2$—is shown in Figs. 3, 4, 6, and 7. Systems with $D \gtrsim 0.1$ are similar to ordinary cataclysmic binaries, which evolve mainly under the influence of the magnetic stellar wind of the donor. However, in the presence of the neutron star, the ISW becomes a more influential factor and leads to an increase of the semimajor axis of the orbit. As a result, the minimum orbital period of these systems becomes $\sim$5 h, and the mass of the donor at the minimum period is close to $0.4M_\odot$ (Fig. 3). The rotational period of the pulsar decreases to the minimum value when $P_{\rm orb} \sim 12$ h and $M_2 \sim 0.1M_\odot$ (Figs. 3, 4).

Under our assumption that the accretion is terminated after the spin-down of the neutron star to the minimum period, the further evolution of the systems proceeds with an almost constant orbital period and, for $D = 1$, ends in the dynamical disruption of the donor (Fig. 7). The possibility of such disruption can be demonstrated analytically. Let us consider the case in which a donor with mass $M_2$ loses mass via its stellar wind. A fraction $\beta$ of this wind is captured by an accretor with mass $M_1$, while the remaining matter leaves the system, carrying away specific angular momentum of the donor. Let us define the average radius of the donor Roche lobe to be $R_R = 0.46(M_2/(M_1 + M_2))^{1/3}$. We now obtain for the logarithmic derivative of the Roche-lobe radius with respect to the donor mass [14]

$$\frac{d\ln R_R}{d\ln M_2} = \frac{1/3 + q(4/3\beta - 1) + 2\beta(q^2 - 1)}{1 + q}. \quad (3)$$

If a donor filling its Roche lobe is a degenerate dwarf or fully convective main-sequence star ($M \lesssim 0.3M_\odot$), $d\ln R_2/d\ln M_2 = -1/3$. Therefore, stable mass exchange requires that $d\ln R_R/d\ln M_2 < -1/3$. It is clear that, when $\beta \lesssim 1/3$, a donor filling its Roche

lobe becomes unstable to an irreversible dynamical expansion, which leads to its disruption on the time scale of the orbital motion and its possible transformation into a disk around the neutron star. The outcome of this type of evolution is the formation of a millisecond pulsar. Indeed, about half of millisecond pulsars are single.

When $0.2 \lesssim D < 1$, the evolution of a binary system can, in principle, also end in the dynamical disruption of the donor, but this does not happen within 15 Gyr, our adopted maximum duration of the computed evolution. Note that the final parts of the tracks of the systems considered fall in the region with $M_2/M_\odot \approx 0.02$–$0.1M_\odot$ in Fig. 4, where no systems are observed. One possible explanation for this is that the donor evaporates completely on time scales that are shorter than cosmological time scales (we shall discuss this problem below). The existence of binary millisecond pulsars with low-mass ($\sim 0.02M_\odot$) donors and short orbital periods can be explained by another scenario (see below).

Let us consider the spin-up of the neutron star in the course of the accretion of matter from the donor. Above, based on the analysis of (2), we showed that, when $\dot{M}_{\rm acc} \gtrsim 10^{-11}$–$10^{-12}M_\odot$/yr, the accretion speeds up the rotation of the neutron star. The conservation of angular momentum implies that, in the case of equatorial accretion, the rotational period of the neutron star is determined only by the mass of the accreted matter, $\Delta M$: $P_{\rm p} \approx 10^{-4}M_\odot/\Delta M$. It is evident that the observed rotational periods of millisecond pulsars, $\sim 10^{-3}$ s, can be attained by accreting $\sim 0.1M_\odot$, while the typical initial mass of the donor is $\sim 1M_\odot$. Hence, only about 10% of the initial donor mass is accreted by the neutron star during the X-ray stage of the evolution of the close binary. Most of the donor mass is probably lost via the ISW of the donor, as is supported by our computations (see the table). The assumption of a low accretion efficiency makes it possible to explain the observed integrated X-ray luminosities of Galactic low-mass X-ray systems ($2 \times 10^{39}$ erg/s [46]) based on their theoretical birth rate $4 \times 10^{-5}$/yr [36]. It is important that this is also the birth rate of Galactic millisecond pulsars. If the lifetimes of such pulsars are $3 \times 10^9$ yr [1, 3, 4], the number of millisecond pulsars in the Galaxy is $\sim 10^5$. For a birth rate of 0.006/yr and lifetimes of $10^7$ yr [1–3], the number of radio pulsars is $\sim 10^5$.

### *3.3. Results of Numerical Modeling of Systems with Evolved Donors*

When $D \lesssim 0.1$, the ISW of the donor does not seriously influence the initial stage of evolution of the system, since it does not significantly decrease the mass of the donor before this star overfills its Roche lobe. The presence of a degenerate helium core fundamentally changes the nature of the donor remnant after the end of the X-ray stage. The rotation of the radio pulsar is increased to the observed periods of several milliseconds (Figs. 3, 4). The hydrogen envelope of the donor is almost completely lost via its ISW. After the end of the X-ray stage, the companion of the millisecond pulsar is a helium dwarf with a mass of $0.13$–$0.3M_\odot$. The correlation of the final $P_{\rm orb}$ and the mass of the remnant is obvious (Fig. 4), as is the correlation of the final $P_{\rm orb}$ and $P_{\rm p}$ values (Fig. 3). Both these correlations are also reflected in the parameters of observed millisecond pulsars in Figs. 3 and 4.

Figure 3 also shows that the $P_{\rm orb}$ values of binary millisecond pulsars are limited to $\sim 280$ days, while Fig. 4 shows that the masses of degenerate helium dwarfs are limited to $\sim 0.3M_\odot$. The reason for these limits is clear. When the masses of the degenerate helium cores of the donors become $\sim 0.3M_\odot$, the rate of mass exchange between the components exceeds the Eddington limit for accretion onto a neutron star (Fig. 7). This reduces the efficiency of the accretion and shortens the duration of the X-ray phase, increasing the final $P_{\rm p}$ values of binary radio pulsars with $P_{\rm orb} \gtrsim 200$ days to $P_{\rm p} \gtrsim 0.1$ s (Fig. 3). The results of our evolutionary computations given in the table reproduce the observed upper limit of the orbital periods of binary millisecond pulsars fairly well. Note that stability of the mass exchange requires that the initial masses of the donors in wide ($D < 0.1$) systems be confined to the very narrow range of 0.85–0.93 $M_\odot$ [14]. Donors with masses below the lower limit have evolutionary lifetimes that are shorter than the Hubble time, and donors with masses above the upper limit are dynamically disrupted upon contact with the Roche lobe.

The orbital-period distribution of millisecond pulsars has one more interesting feature, noted earlier in [8]. Systems with $23 \lesssim P_{\rm orb}({\rm day}) \lesssim 56$ are rare (Fig. 3). Of course, the statistics implying this property are poor. However, an important circumstance indicating that we should consider systems with these periods arises in the analysis of the evolution of the main precursors of millisecond pulsars, binaries with initial masses $10M_\odot + 1M_\odot$. The primary components of such systems evolve into neutron stars with masses of $\sim 1.4M_\odot$. With the component-mass ratios of these systems, the secondary masses remain virtually unchanged in the inevitable common-envelope stage. The estimated maximum orbital period after the common-envelope stage, which drives the components closer together, is $\sim 20$ days [7]. This value coincides with the period at the left border of the period "gap." As a result, there arises the problem

of explaining the origin of binary millisecond pulsars with $P_{\rm orb} \approx 100$ days.

One possible explanation is that the initial component masses of these systems were $9M_\odot + 1M_\odot$. Then, the primary ends its evolution as a massive ($\sim(1.2{-}1.3)M_\odot$) oxygen–neon degenerate dwarf. In such a system, Roche-lobe overflow by the low-mass donor results in the formation of a supersoft X-ray source that is fed by mass exchange at a rate of $\dot{M} \approx 10^{-7}M_\odot$/yr (Fig. 7) and in stationary hydrogen burning at the surface of the accretor. The source RXJ 0513.9-6951 [47], with an orbital period of 83.3 days, may provide an example of such a system. If the mass exchange in the semidetached stage of evolution is conservative, the orbital period of the system can increase considerably up until the accretion-induced collapse of the oxygen–neon core of the dwarf into a neutron star. However, numerical estimation of the final orbital period of the system and of the occurrence rate of this scenario is complicated by the presence of several uncertain parameters.

Another possibility for the formation of long-period ($P_{\rm orb} \approx 100$ days) systems with millisecond pulsars is associated with collisions of single neutron stars and main-sequence binaries in globular clusters [48]. The probability of forming a binary with a neutron star in a collision increases with the semimajor axis of the system's orbit [48]. This can explain, still qualitatively, the concentration of these systems near $P_{\rm orb} \approx 100$ days. Recall that systems with orbital periods larger than $\sim 1$ yr (Fig. 3) do not produce millisecond pulsars, probably due to the short duration of the X-ray phase and the limitation of the accretion rate to the Eddington limit.

### *3.4. Results of Numerical Modeling of Systems with Nondegenerate Helium-star and Degenerate-dwarf Donors*

It remains to explain the origin of the closest binary millisecond pulsars with 1 h $\lesssim P_{\rm orb} \lesssim$ 8 h, 0.002 s $\lesssim P_{\rm p} \lesssim$ 0.005 s, and $0.01 \lesssim M_2/M_\odot \lesssim 0.03$ (Figs. 3, 4, and 6). The special characteristics of this group of objects are the very low masses of the companions of the millisecond pulsars and their very short orbital periods. When looking for a scenario to explain their origin, it is natural to consider systems with nondegenerate helium-star and degenerate-dwarf donors [14].

Let us consider the evolution of systems with nondegenerate helium donors. The precursors of nondegenerate helium stars with masses of 0.35–0.75 $M_\odot$ are the components of close binaries with initial masses 2.5–5 $M_\odot$ [7]. According to simple estimates, after two common-envelope stages, the helium subdwarf may become a component of a very close system with an orbital period shorter than $\sim 1$ day. This is supported by observations of binary sdB stars [49]. The evolution of a system with a helium star and neutron star is determined primarily by the radiation of gravitational waves. As the components become closer, the ISW does not affect the evolution of the system to any appreciable extent. In the semidetached stage of the evolution, the orbital period of the system continues to decrease to $\sim 15$ min (Fig. 3, 4). X-ray binaries with such short orbital periods are in fact known (for instance, 4U 1820-30 [50]). The mass of the donor corresponding to the minimum period is $\sim 0.2M_\odot$. Further evolution leads to an increase of $P_{\rm orb}$, until the mass-loss rate of the donor decreases to $M_{cr} \sim 10^{-11}M_\odot$/yr (Fig. 7). Further, the neutron star is probably transformed from an X-ray pulsar into a radio pulsar and, according to our assumptions, the donor begins to lose mass in a Jeans regime, with the orbital period remaining nearly constant. Note that, in Figs. 3 and 4, the shortest orbital periods, close to the $P_{\rm orb}$ values of X-ray binaries, are possessed by the millisecond pulsars of this group, supporting the possibility that pulsars may make a transition from an X-ray phase to a radio phase at orbital periods of several hours. This group is probably limited from the long-period side, at periods of $\sim 1$ day, by the evaporation or tidal disruption of the donor [14]. The donor must disappear on time scales shorter than $\sim 10^9$ yr, since no companions with masses lower than $\sim 0.01M_\odot$ are known, despite the fact that the sensitivity of the pulsar "clock" is sufficient to discover planets with masses several orders of magnitude lower than this [51, 52]. The possibility that the donors of this group are completely evaporated by their radio-pulsar companions is underlined by the fact that about half of radio pulsars display eclipses (Fig. 3), which last a considerable fraction of $P_{\rm orb}$ in some systems. In this case, the radio pulsar is probably eclipsed by the stellar wind of the evaporating donor.

Finally, let us discuss the possible role of degenerate donors in the formation of millisecond pulsars in short-period systems. Since the initial mass of the carbon–oxygen dwarf is higher than $\sim 0.6M_\odot$, the initial mass-exchange rate after contact with the Roche lobe exceeds $\sim 10^{-4}M_\odot$/yr [14], and the formation of a common envelope or disruption of the donor seems inevitable. The final product of the evolution after the probable evaporation of the bulk of the disk material will be a single millisecond pulsar, possibly surrounded by a planetary system.

The situation is more complicated for low-mass ($\sim 0.15M_\odot$) degenerate helium donors. In this case, the relatively low initial mass-exchange rate (Fig. 7) probably makes it possible to avoid the formation of a common envelope or disruption of the donor, enabling the spin-up of the neutron star to millisecond

periods. Note the appreciable influence of the initial temperature (age) of the dwarf on the evolution of the system (Fig. 4). To achieve agreement with the observations, we must again assume that the donor is evaporated or disrupted when its mass decreases to $\sim 0.01 M_\odot$ (Fig. 4). The complete evaporation of the donors currently seems the preferred hypothesis for both helium and hydrogen–helium donors with masses $\lesssim 0.1 M_\odot$, since the dynamical disruption of the donors may result in the formation of circumstellar disks around millisecond pulsars, which can then develop into planetary systems. However, the latter are rare: only two of several dozen known millisecond pulsars possess planetary systems. Moreover, the absence of detectable infrared emission from dust near millisecond pulsars corresponding to disks with masses of $\sim 10^{-6} M_\odot$ [53, 54] also testifies to the, as a rule, complete evaporation of the donor at the end of the evolution.

It is interesting that a wide range of $P_\mathrm{p}$ values are observed among single radio pulsars in globular clusters that have obviously passed through a stage of spin-up via accretion in close binary systems: from 0.002 to 0.3 s. This means that their rotation slows with time. However, there do not appear to be such "spun-down" objects among pulsars with $M_2 \approx 0.02 M_\odot$ (Fig. 4). This may provide an additional argument that they are young and their donor evaporate relatively rapidly, on time scales shorter than the time scale of the spin-down ($\sim 10^9$ yr). Note that the tracks of systems with helium nondegenerate and degenerate donors in Figs. 3, 4, 6, and 7 are fairly similar, but some of the millisecond pulsars with $M_2 \approx 0.02 M_\odot$ are found in globular clusters, where the formation of nondegenerate helium stars in the last $\sim 10^{10}$ yr was impossible. Therefore, systems with low-mass ($\sim 0.15 M_\odot$) degenerate helium dwarfs are required to explain the presence of this group of binary millisecond pulsars in globular clusters.

We are not able to fully resolve the question of the total evaporation of the donor stars using computations based on the ISW model we have adopted. However, let us give some simple estimates of the donor mass that could be evaporated by a millisecond pulsar, based on the conservation of energy for the case when the donor fills its Roche lobe. Equating the gravitational binding energy of the star to the rotational energy of a neutron star with $P_\mathrm{p}$, we find for the mass that can be evaporated

$$\frac{M_2}{M_\odot} = 10^{-2} \frac{\gamma^{3/4}}{P_\mathrm{p}^{3/2}} \left( \frac{R}{R_\odot} \right)^{3/4}, \qquad (4)$$

where $\gamma$ is the fraction of the neutron star's energy that goes into the evaporation. Equation 4 shows that, for similar $\gamma$ and $P_\mathrm{p}$ values, the transition from a hydrogen–helium donor with a radius of $\sim 0.1 R_\odot$ to a nondegenerate helium star with a radius of $\sim 0.01 R_\odot$ results in an almost sixfold reduction of the amount of evaporated material. Figures 4 and 6 indeed show an almost sixfold difference in the masses of the companions of binary radio pulsars with the shortest orbital periods (less than $\sim 1$ day) and comparable rotational periods. This supports the hypothesis that the donors in these systems are evaporated. Further evidence for the evaporation of low-mass, main-sequence companions is provided by the high incidence of eclipsing millisecond pulsars in the cluster 47 Tuc: five of fifteen binary radio pulsars discovered in this cluster are eclipsing [55]. The stellar wind from the evaporated donor is effective at shielding the radio emission of millisecond pulsars.

## 4. CONCLUSIONS

The current paper is a continuation of our earlier study of the conditions for the formation of the distribution of spatial velocities of radio pulsars [7] and of the evolution of low-mass close binary systems with accreting neutron-star components, which evolve under the influence of the induced and magnetic stellar winds of the donor, gravitational-wave radiation, and mass exchange between the components [14]. One result of [14] was the model separation of neutron stars into several families with differing spatial velocities. The most rapid neutron stars appeared to be the remnants of the primary components of massive close binaries ($v \approx 100$–$600$ km/s) and products of the evolution of secondary components ($v \approx 50$–$150$ km/s). The observational data of [9, 10] confirm the existence of two families of radio pulsars with differing spatial velocities. The apparent absence of radio pulsars with velocities typical of their progenitors, O and B stars, can be explained by supposing that a modest kick provides them with velocities up to $\sim 100$ km/s, or that supernova explosions of the components of wide binaries and single stars result in the formation of slowly rotating neutron stars without appreciable radio emission. In the present paper, we adopt the latter hypothesis.

Our earlier analysis of the rotational velocities of neutron stars in close binaries with nonzero orbital eccentricities [11, Fig. 9], which is extended in the present paper, led to two conclusions (Fig. 2). The first is that the rotational velocities of the radio pulsars in these systems can be explained by their accumulation of the angular momentum of the axial rotation of the cores of the supernova precursors, which were synchronized with their orbital motion. The second conclusion is that the range of rotational velocities of pulsars allowed by the assumption that all radio pulsars form in close binary systems with synchronized

rotational and orbital motions (0.01–4 s) nearly coincides with the range of rotational velocities of single radio pulsars. This suggests that both the high spatial velocities and rapid rotation rates of radio pulsars are due to their formation in binary systems. The fact that some radio pulsars are single is then a consequence of the fact that most binaries are disrupted by the second supernova explosion in the system. Numerical analysis of this scenario, aimed at estimating the fraction of binary pulsars of various types, is complicated by observational selection effects and uncertainties in the theory of the evolution of neutron stars in close binary systems.

It has long been clear that millisecond radio and X-ray pulsars are neutron stars that have been spun up during a long stage of accretion from a low-mass companion. The induced stellar wind then plays a role in explaining the observed rotational velocities of millisecond pulsars. If we take the stellar-wind velocity to be $v_{ISW} = \alpha_{ISW}(2GM_2/R_2)^{1/2}$, where $G$ is the gravitational constant and $R_2$ the donor radius, and we take the capture radius of the neutron star to be $2GM_{\rm NS}/v_{ISW}^2$, where $M_{\rm NS}$ is the mass of the neutron star, the final rotational period of the neutron star will be

$$P_{\rm p} = 0.005\ \alpha_{ISW}^4 \left(\frac{M_2}{M_{\rm NS}}\right)^{4/3}. \qquad (5)$$

We assume here that the donor fills its Roche lobe, but, even in this case, the efficiency of accreting the matter it loses is $\sim$10% [7]. When deriving (5), we also assumed that the matter captured by a neutron star with a mass of $\sim 1.4M_\odot$ and a radius of 10 km is accreted at its Keplerian velocity along the equator and that the neutron star itself rotates as a rigid body. When $M_2 \approx 0.9M_\odot$, $M_{\rm NS} = 1.4M_\odot$, and $\alpha_{ISW} = 1$, Eq. (5) yields rotational velocities that are typical of radio pulsars. This is supported by the results of our evolutionary computations presented here. However, it is obvious that this includes a strong dependence on a poorly constrained parameter describing the velocity of the stellar wind. In the context of this uncertainty, we can apply (5) to estimate $\alpha_{ISW}$ from the observed rotational velocities of millisecond pulsars. In the formalism we have adopted, we can explain the observed $P_{\rm p}$ if this parameter is not very different from unity. Further work on the physics of the ISW is necessary if we wish to decrease the uncertainties in this fundamental problem.

Analysis of the evolutionary status of radio pulsars in close binary systems has made it possible to separate them into several groups with differing previous evolutions. The starting point of the evolution is the formation of a neutron star in a pair with a solar-mass main-sequence star, degenerate dwarf, or nondegenerate $0.3M_\odot$–$1M_\odot$ helium star. Such systems can be produced by an initial system with a large ($\sim$10) initial component-mass ratio or by a collision of an old neutron star with a low-mass close binary in the core of a globular cluster. The role of collisions in the dense cores of the globular clusters is underlined by the large number (35–90) [55] of millisecond pulsars in the core of the ordinary globular cluster 47 Tuc. Supposing that this cluster's mass is $\sim 10^{-6}$ of the mass of the Galaxy, the "expected" number of millisecond pulsars in the Galaxy is $\sim 5 \times 10^7$. This is about a factor of 500 higher than our estimate of the number of observable millisecond pulsars derived above from the rate of formation of low-mass X-ray binaries. It is clear that the overwhelming majority of millisecond pulsars in globular clusters are produced in collisions.

Systems with $0.3 \lesssim P_{\rm orb}({\rm day}) \lesssim 20$ are the descendants of massive binaries with $10 \lesssim M_{10}/M_\odot \lesssim 25$ and $M_{20}/M_\odot \lesssim 1.5$. In the common-envelope stage, which is inevitable in this case, the orbital period of the system decreases to less than $\sim$ 20 days. The magnetically coupled stellar wind becomes the driving force of the evolution of the closest systems. The final outcome of the evolution of such systems is a single millisecond pulsar (after the evaporation of the donor, with a mass of $\lesssim 0.1M_\odot$). In wider systems of this class, the donor has a degenerate helium core at the time of Roche-lobe overflow. After the expansion of the hydrogen envelope of the donor and its partial accretion by the neutron star, this core becomes a close ($P_{\rm orb} \lesssim 20$ days, $M_2 \approx 0.1M_\odot$) companion to the millisecond pulsar.

Two possibilities are open to systems with $P_{\rm orb} > 60$ days. In the first, the initial system has components with $9M_\odot$ and $1M_\odot$. The more massive component produces a degenerate oxygen–neon dwarf with a mass of $\sim 1M_\odot$. The expansion of the secondary results in the formation of a semidetached system. Accretion by the degenerate dwarf, which is accompanied by an increase in the orbital period, increases the mass of the accretor to the Chandrasekhar limit, leading to the collapse of the dwarf into a rapidly rotating neutron star. The second possibility is the formation of wide systems in the dense cores of globular clusters via collisions of neutron stars with wide binaries.

Finally, the closest binary radio pulsars with $P_{\rm orb} \lesssim 8$ h (Figs. 2–4) result from the evolution of systems with helium donors. Nondegenerate and degenerate donors with initial masses $(0.4$–$1)M_\odot$ and $\sim 0.15M_\odot$, respectively, decrease their masses to $\sim 0.02M_\odot$ via their ISW and mass exchange, after which they are evaporated. The final products of this evolution are single millisecond pulsars. The fate

of systems with carbon–oxygen degenerate donors remains unclear. Roche-lobe overflow by such donors probably results in their disruption and the formation of massive disks or extended envelopes (Thorne–Żytkow objects). The formation of a millisecond pulsar accompanied by the evaporation of the disk is also possible in this case. Hence, some bright stellar X-ray sources may be single. The fate of such objects must be studied numerically.

The final conclusion of this paper is that the high spatial and rotational velocities of radio pulsars are most likely the result of their previous evolution in various types of close binary systems.

## 5. ACKNOWLEDGMENTS

This work was supported by a Presidential Grant (no. 00-15-96722), the State Science and Technology Program "Astronomy," the Russian Foundation for Basic Research (project code 02-02-17524) and a Russian Scientific Schools Grant (no. 00-15-96553). The authors thank R. Manchester for useful discussions of the problem of empirical estimation of the birth rate of radio pulsars in the Galaxy.

## REFERENCES

1. O. H. Gusejnov, G. Yazgan, S. Ozgan, *et al.*, astro-ph/0205540 (2002).
2. G. L. Fan, K. S. Cheng, and R. N. Manchester, Astrophys. J. **557**, 297 (2001).
3. R. N. Manchester, J. F. Bell, F. Camilo, *et al.*, astro-ph/0112166 (2001).
4. F. Camilo, astro-ph/0210620 (2002).
5. G. G. Pavlov, D. Sanval, and G. P. Carmire, astro-ph/0112322 (2001).
6. M. Muno, F. Ozel, and D. Chakrabarty, astro-ph/0204501 (2002).
7. I. Iben, Jr. and A. V. Tutukov, Astrophys. J. **456**, 738 (1996).
8. J. H. Taylor, R. N. Manchester, and A. G. Lyne, Astrophys. J., Suppl. Ser. **88**, 529 (1993).
9. A. V. Tutukov, N. N. Chugaĭ, and L. R. Yungel'son, Pis'ma Astron. Zh. **10**, 586 (1984) [Sov. Astron. Lett. **10**, 244 (1984)].
10. Z. Azzoumanian, D. F. Chernoff, and J. M. Cordes, Astrophys. J. **568**, 289 (2002).
11. I. Iben, Jr., A. V. Tutukov, and L. R. Yungelson, Astrophys. J., Suppl. Ser. **100**, 233 (1995).
12. A. C. Fabian, J. E. Pringle, and M. J. Rees, Mon. Not. R. Astron. Soc. **172**, 15 (1975).
13. G. W. Clark, Astrophys. J. **199**, L143 (1975).
14. I. Iben, Jr., A. V. Tutukov, and A. V. Fedorova, Astrophys. J. **486**, 955 (1997).
15. R. Taam, A. King, and H. Ritter, Astrophys. J. **541**, 329 (2000).
16. S. E. Thorsett and D. Chakrabarty, Astrophys. J. **512**, 288 (1999).
17. R. T. Edwards and M. Bailes, Astrophys. J. **553**, 801 (2001).
18. F. Camilo, D. R. Lorimer, P. Freire, *et al.*, Astrophys. J. **535**, 975 (2000).
19. N. D'Amico, A. G. Lyne, R. N. Manchester, *et al.*, Astrophys. J. **548**, L171 (2001).
20. F. Camilo, A. G. Lyne, R. N. Manchester, *et al.*, Astrophys. J. **548**, L187 (2001).
21. D. Nice, Z. Azzoumanian, and S. Thorsett, astro-ph/9911211 (1999).
22. B. W. Stappers, M. H. van Kerkwijk, J. F. Bell, *et al.*, Astrophys. J. **548**, L183 (2001).
23. R. T. Edwards and M. Bailes, Astrophys. J. **553**, 801 (2001).
24. N. D'Amico, A. Possenti, R. N. Manchester, *et al.*, Astrophys. J. **561**, L89 (2001).
25. F. R. Ferraro, A. Possenti, N. D'Amico, *et al.*, Astrophys. J. **561**, L93 (2001).
26. D. Galloway, D. Chakrabarty, E. Morgan, *et al.*, astro-ph/0206493 (2002).
27. C. B. Markwardt, J. H. Swank, T. E. Strohmayer, *et al.*, Astrophys. J. **575**, L21 (2002).
28. J. Poutanen and M. Gierlinski, astro-ph/0206149 (2002).
29. L. Hommer, S. Anderson, S. Wachter, *et al.*, astro-ph/0205332 (2002).
30. X.-D. Li, Astrophys. J. **564**, 930 (2002).
31. D. Z. Liu, J. van Paradijs, and E. van den Heuvel, Astron. Astrophys. **368**, 1021 (2001).
32. A. V. Tutukov and A. V. Fedorova, Astron. Zh. **79**, 847 (2002) [Astron. Rep. **46**, 765 (2002)].
33. R. Downes, R. F. Webbink, and M. M. Shara, Publ. Astron. Soc. Pacif. **109**, 345 (1997).
34. A. V. Tutukov and A. M. Cherepashchuk, Astron. Zh. (2002, in press).
35. A. V. Tutukov and L. R. Yungel'son, Nauchn. Inform. Astrosoveta Akad. Nauk SSSR **27**, 3 (1973).
36. A. V. Tutukov and L. R. Yungel'son, Astron. Zh. **79**, 738 (2002) [Astron. Rep. **46**, 667 (2002)].
37. L. Bildstein and D. Chakrabarty, Astrophys. J. **557**, 292 (2001).
38. I. Stairs, S. E. Thorsett, J. H. Taylor, *et al.*, astro-ph/0208357 (2002).
39. A. V. Tutukov and L. R. Yungel'son, Nauchn. Inform. Astrosoveta Akad. Nauk SSSR **27**, 70 (1973).
40. J. Weisber and J. Taylor, astro-ph/0211217 (2002).
41. G. S. Bisnovatyĭ-Kogan, Astron. Zh. **47**, 813 (1970) [Sov. Astron. **14**, 652 (1970)].
42. A. G. Masevich and A. V. Tutukov, *Stellar Evolution: Theory and Observations* [in Russian] (Nauka, Moscow, 1988).
43. A. Heger and S. Woosley, astro-ph/0206005 (2002).
44. B. E. Schaefer, C. L. Gerardy, and P. Hoflich, astro-ph/0211189 (2002).
45. V. M. Lipunov, *Astrophysics of Neutron Stars* [in Russian] (Nauka, Moscow, 1987).
46. H. Grimm, M. Gilfanov, and R. Sunyaev, astro-ph/0109239 (2001).
47. A. P. Cowley, P. C. Schmidtke, D. Crampton, *et al.*, Astron. J. **124**, 2233 (2002).

48. J. G. Hills, Mon. Not. R. Astron. Soc. **175**, 1 (1976).
49. R. Morales-Pueda, P. Maxted, T. Marsh, and R. North, astro-ph/0209472 (2002).
50. J. van Paradijs, in *X-ray Binaries*, Ed. by W. H. G. Lewin, J. van Paradijs, and E. P. J. van den Heuvel (Cambridge Univ. Press, Cambridge, 1995), p. 265.
51. A. Wolszczan, Science **264**, 538 (1994).
52. T. Shabanova, Astrophys. J. **453**, 779 (1995).
53. T. Lazio, J. Fisher, and R. Foster, astro-ph/0109473 (2001).
54. J. S. Greaves and W. S. Holland, Mon. Not. R. Astron. Soc. **316**, L21 (2000).
55. D. R. Lorimer, F. Camilo, P. Freire, *et al.*, astro-ph/0210460 (2002).

*Translated by L. Yungel'son*

*Astronomy Reports, Vol. 47, No. 7, 2003, pp. 613–620. Translated from Astronomicheskiĭ Zhurnal, Vol. 80, No. 7, 2003, pp. 665–672.*


# The Electric Fields of Radio Pulsars with Asymmetric Nondipolar Magnetic Fields

**E. M. Kantor and A. I. Tsygan**

*Ioffe Physicotechnical Institute, Russian Academy of Sciences, Politekhnicheskaya ul. 26, St. Petersburg, 194021 Russia*

Received July 11, 2002; in final form, November 27, 2002

**Abstract**—The effect of the curvature of open magnetic field lines on the generation of electric fields in radio pulsars is considered in the framework of a Goldreich–Julian model, for both a regime with a free outflow of electrons from the neutron-star surface and the case of a small thermoemission current. An expression for the electron thermoemission current in a strong magnetic field is derived. The electric field associated with the curvature of the magnetic flux tubes is comparable to the field generated by the relativistic dragging of the inertial frames. © *2003 MAIK "Nauka/Interperiodica"*.

## 1. INTRODUCTION

The electric fields of rotating neutron stars possessing magnetic fields (i.e., radio pulsars) due to the free outflow of charge are determined in Goldreich–Julian models by the general relativistic effect of dragging of the inertial frames. This fact was proved for the case of dipolar magnetic fields by Muslimov and Tsygan [1, 2] and Beskin [3], and for an arbitrary axially symmetric magnetic field by Tsygan [4].

The aim of the present work is to study the more general case when tubes of open, nondipolar magnetic-field lines are curved. We carry out calculations for a Goldreich–Julian model and the case of thin tubes of open field lines and an arbitrary magnitude of the electron thermoemission current. In order for this type of model to be applicable, the electron–positron plasma must be produced at heights considerably greater than the characteristic thickness of the tubes of open field lines.

If the magnetic field has a dipolar structure, there is no outflow of electrons and general relativistic effects can be ignored, so that our results then reduce to those obtained by Ruderman and Sutherland [5].

We derive an expression for the thermoemission current of degenerate electrons from the surface layer of a neutron star in a strong magnetic field. The accelerating potential difference along the tube depends appreciably on the thermoemission electron current.

## 2. CURVATURE OF NONDIPOLAR MAGNETIC-FIELD LINES OF A NEUTRON STAR

According to modern theoretical concepts, electron–positron pairs must be formed in order for a pulsar to generate radio emission. These pairs are born from gamma-rays interacting with the magnetic-field component perpendicular to the photon momentum. The shorter the radius of curvature of the field lines, the greater the efficiency of the pair production. The radius of curvature of a dipolar field in the region of open field lines near the stellar surface is $10^8$ cm for a pulsar period of $P = 1$ s, but this radius can become a factor of several tens smaller in the case of a nondipolar field.

To allow for a nondipolar field, we use the following model, put forward in [6]. Let a star of radius $a$ possess a magnetic moment $\mathbf{m}$, so that the field intensity at its magnetic pole is $B_0 = 2m/a^3$. An additional magnetic dipole with moment $\mathbf{m}_1 \perp \mathbf{m}$ is located at a depth of $a \times \Delta$ (where $\Delta \approx 0.1$) near the neutron star's pole, so that its field intensity is $B_1 = m_1/a^3\Delta^3$ (see Fig. 2 below). We will assume that our choice of the parameter $\Delta = 0.1$, which corresponds to the thickness of the crust, will not lead to the rapid decay of the additional dipole moment $\mathbf{m}_1$.

As was already noted in [6], this proposed configuration of magnetic moments is not artificial. The entire stellar surface can be covered by magnetic anomalies. Nevertheless, their presence in the region of closed magnetic-field lines should not affect the pulsar electrodynamics described by the Goldreich–Julian model.

The equation for the magnetic-field lines for the total field $\mathbf{B} = \mathbf{B}_0 + \mathbf{B}_1$ in a small-angle approximation in the $\mathbf{m}$, $\mathbf{m}_1$ plane in the spherical coordinates $(\eta = r/a, \theta, \varphi)$ with the $z$ axis $//\,\mathbf{m}$ is

$$\frac{d\eta}{B_r} = \frac{\eta d\theta}{B_\theta}, \quad B_r = \frac{B_0}{\eta^3}, \tag{1}$$

1063-7729/03/4707-0613$24.00 

$$B_\theta = \frac{B_0}{2\eta^3}\left[\theta + 2\nu\left(\frac{\Delta\eta}{\eta - 1 + \Delta}\right)^3\right],$$

where $\nu = B_1/B_0$. It can easily be shown that the radius of curvature of the field lines $\mathbf{B}$ can be expressed in terms of the function $f = \dfrac{B_r}{B_\theta}$ as

$$R = r\frac{(1+f^2)^{3/2}}{1 + f^2 - \dfrac{df}{d\theta}}. \quad (2)$$

In the case of a dipolar field, we obtain

$$R_{\rm dip} = \frac{4}{3}\frac{r}{\theta}, \quad k_{\rm dip} = \frac{3}{4}\frac{\theta}{r}. \quad (3)$$

On the other hand, the curvature of the nondipolar field specified above is

$$k = k_{\rm dip}\left[1 + \frac{2\nu}{\theta}\left(\frac{\Delta\eta}{\eta - 1 + \Delta}\right)^3\right]. \quad (4)$$

If we adopt the values $\nu = 1$ and $\Delta = 0.1$, then, with $\eta = 1$ and $\theta = 0.1$, the curvature will increase by a factor of 20.

## 3. THE ELECTRIC FIELDS OF RADIO PULSARS IN THE REGION OF OPEN ASYMMETRIC MAGNETIC-FIELD LINES

Let us determine the behavior of the electrostatic potential in a thin, curved tube of open magnetic-field lines in a coordinate system corotating with the star. The radio-pulsar magnetosphere is described by the Goldreich–Julian model, in which the walls and base of the tube are equipotential surfaces.

The equation for the electrostatic potential $\Phi$, taking into account the general relativistic dragging of the inertial frames, has the form [7]

$$\nabla\left(\frac{1}{\alpha}\nabla\Phi\right) = -4\pi(\rho + \rho_{\rm eff}), \quad (5)$$

$$\rho_{\rm eff} = \frac{1}{4\pi c}\nabla\left\{\frac{1}{\alpha}[1 - \kappa(a/r)^3][(\mathbf{\Omega}\times\mathbf{r})\times\mathbf{B}]\right\}.$$

Here, $\rho$ is the electric charge density in the coordinate system corotating with the star, $\alpha = (1 - r_g/r)^{1/2}$, $r_g = (2GM)/c^2$ is the gravitational radius of a star with mass $M$, $\kappa = (r_g/a)(I/Ma^2)$, $I$ is the moment of inertia of the star, and $a$ is its radius. The operator $\nabla$ is taken in the spatial part of the Schwarzschild metric. The parameter $\kappa$ describes the effect of the inertial-frame dragging; its characteristic value is 0.15.

Further, we shall assume that $\alpha = 1$ and calculate the operator $\nabla$ in a flat, three-dimensional space. In the case of a thin magnetic tube, we obtain

$$\rho_{\rm eff} \cong \frac{1}{2\pi c}[1 - \kappa(a/r)^3]\mathbf{\Omega}\mathbf{B}, \quad (6)$$

where $r$ is the distance from the center of the star.

Let us introduce the cylindrical coordinate system $(z, u, \varphi)$, whose $z$ axis is directed along the tube. The direction of the $z$ axis for a curved tube depends on the distance from the star. The coordinate $u$ is the cylindrical radius, and $\varphi$ is the polar angle.

Let us consider regions at heights above the radius of the polar spot formed by the intersection of a magnetic tube with the stellar surface. The corresponding electric field varies across the tube over considerably smaller scales than along the tube. Therefore, the condition $|\partial\Phi/\partial z| \ll |\partial\Phi/\partial u|$ is satisfied.

Next, let us assume that the cross section of the tube is circular (the exact shape of the cross section deviates slightly from circularity and was studied in [8] for the case of a dipolar field). In addition, the potential depends only weakly on the angle $\varphi$ for a thin tube. Therefore, we obtain the one-dimensional equation

$$\frac{1}{\xi}\frac{d}{d\xi}\left(\xi\frac{d\Phi}{d\xi}\right) = -4\pi u_0^2\left\{[1 - \kappa(a/r)^3]\frac{\mathbf{\Omega}\mathbf{B}}{2\pi c} + \rho\right\}, \quad (7)$$

where $\xi = u/u_0$ and $u_0$ is the tube radius at a specified distance from the star.

Let us find the charge density $\rho$ assuming that the particles move along the field lines with velocities close to the velocity of light. We use the equation of continuity, which can be written as $\mathbf{B}\nabla(\rho/B) = 0$, taking into account the condition $\mathrm{div}\mathbf{B} = 0$. Since $\mathbf{B}//z$, $\rho/B$ should depend only on $\xi$. It is convenient to rewrite the charge density in the form

$$\rho = \frac{\Omega B}{2\pi c}A(\xi)\cos\chi_s, \quad (8)$$

where $\chi_s$ is the angle between the angular velocity and magnetic field near the stellar surface.

Let us study a regime with a free outflow of charged particles from the neutron-star surface. In this case, the electric field at the surface is zero. In addition, according to the well-known solutions for a dipolar field, $\rho \cong \rho_{\rm eff}$ above the stellar surface, up to a height that is comparable to the size of the polar spot. As a result, we obtain $A(\xi) = \kappa - 1$.

The final equation for the electrostatic potential $\Phi$ takes the form

$$\frac{1}{\xi}\frac{d}{d\xi}\left(\xi\frac{d\Phi}{d\xi}\right) \quad (9)$$

$$= -\frac{2\Omega F}{\pi c}\{[1-\kappa(a/r)^3]\cos\chi + (\kappa-1)\cos\chi_s\},$$

where $F = \pi u_0^2 B$ is the magnetic flux through the tube (which is conserved along its entire length) and $\chi$ is the angle between the local magnetic field in the tube and the angular velocity of the star (which obviously depends on the distance from the star's center $r$). Using the appropriate boundary condition (namely, the potential at the tube walls is equal to zero), we obtain

$$\Phi = \frac{\Omega F}{2\pi c}(1-\xi^2) \tag{10}$$
$$\times \{[1-\kappa(a/r)^3]\cos\chi + (\kappa-1)\cos\chi_s\}.$$

This solution gives the correct value of the potential at the neutron-star surface ($\Phi = 0$), but it cannot be used at distances from the surface smaller than the radius of the magnetic tube.

The magnetic flux in a nondipolar tube was found in [9]. Since the flux is conserved along the entire tube, we shall calculate this flux at large distances from the star, where only the dipolar component survives. Therefore, the flux will be determined by the magnetic moment of the star $m$ (the moment $m_1$ is small). The flux can easily be calculated on a hemisphere with the "light radius" $r_L = c/\Omega$: $F = \int_{(2\pi)} \mathbf{B}(r_L)\times\mathbf{n}dS = 2\pi m\Omega/c$.

Let us analyze the behavior of the potential in various tubes. We consider first a dipolar tube:

$$\Phi_{\rm dip} = \frac{\Omega F}{2\pi c}(1-\xi^2)\kappa[1-(a/r)^3]\cos\chi. \tag{11}$$

In this case, $\cos\chi$ is constant along the tube, and the dependence of the potential on the distance is specified by the factor $\kappa[1-(a/r)^3]$. Figure 1 presents a plot of the potential at the tube axis ($\xi = 0$) in units of $\dfrac{\Omega F}{2\pi c}$ for the case of a coaxial rotator. The maximum difference of the potentials is $0.15\dfrac{F\Omega}{2\pi c}$.

For a nondipolar field in the configuration considered above, there are two ways in which a tube can be bent (depending on the direction of the dipole located near the stellar surface), as shown in Fig. 2.

Let us calculate the behavior of the potential in the tube. The cosines of the angle between the magnetic field and the angular velocity for the first and second types of tube bending are

$$\cos\chi = \cos\chi_0\sqrt{\frac{f^2}{1+f^2}} + \sin\chi_0\sqrt{\frac{1}{1+f^2}}, \tag{12}$$

$$\cos\chi = \cos\chi_0\sqrt{\frac{f^2}{1+f^2}} - \sin\chi_0\sqrt{\frac{1}{1+f^2}},$$

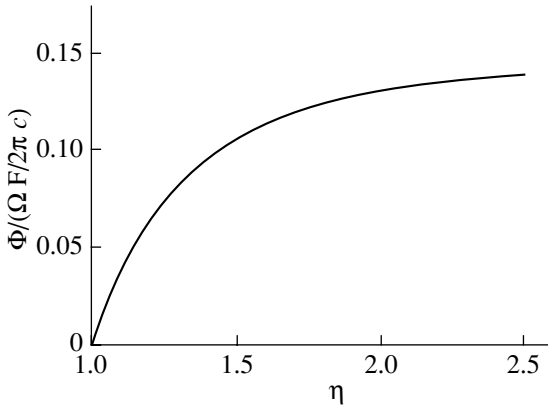


**Fig. 1.** Behavior of the potential in a regime with a free outflow of electrons in a dipolar tube of a coaxial rotator.

where $f = \dfrac{B_r}{B_\theta} = \dfrac{1}{\nu}\left(\dfrac{\eta-1+\Delta}{\Delta\eta}\right)^3$ and $\chi_0$ is the angle between the angular velocity and magnetic field at large $r$ (where only the dipolar field survives). Let us analyze the potential for various $\chi_0$ (assuming that $\nu = 1$). For the second type of tube bending, we find for the case of a coaxial rotator that the potential of a nondipolar tube at large distances is a factor of 2.7 greater than the potential of a dipolar tube. The difference in the potentials becomes even larger if the rotator is not coaxial (see Fig. 3).

Even an orthogonal rotator possesses a considerable potential difference, $0.6(\Omega F/2\pi c)$, whereas the potential in a similar dipolar tube has only a component associated with the variation of the angle between the angular velocity and magnetic field in the tube cross section [10]. This effect is small and, therefore, was ignored.

The largest potential difference is reached when $\chi_0 = 56^\circ$ and is equal to $0.72(\Omega F/2\pi c)$, i.e., a factor of 4.8 greater than the potential difference for a dipolar coaxial rotator.

Let us now consider the first type of tube bending (Fig. 4). The potential of a coaxial rotator will have the same appearance as in the previous case. The behavior of the potential will change significantly as the angle $\chi_0$ increases. Namely, positive particles will be accelerated along the open field lines if this angle is not very small ($\cos\chi_0 \le 0.8$). When $\cos\chi_0 \approx 0.9$, the behavior of the potential is nonmonotonic. We can assume that the electron–positron plasma generated in the region $\eta = 1$–$2$ will smooth the potential. As a result, a layer of stationary charged particles can be formed. This situation must be considered separately.

We now turn to the case of a cold stellar surface, when there is no thermoelectron emission. Then, $\rho =$

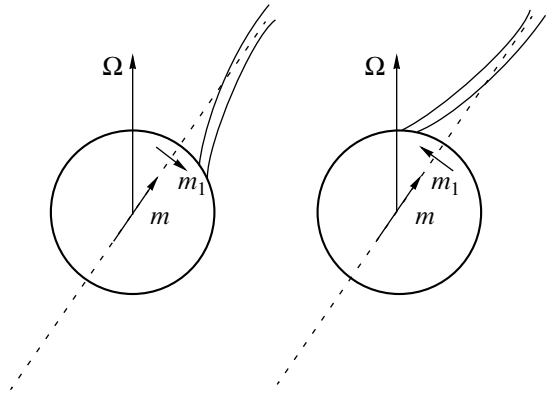


**Fig. 2.** Two cases of bending of a tube of open field lines, depending on the direction of the additional dipole located near the stellar surface.

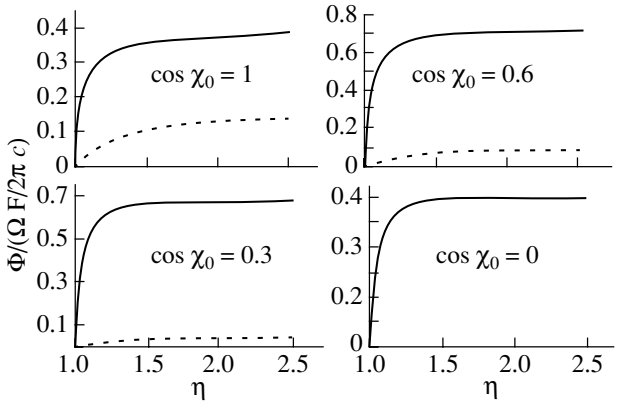


**Fig. 3.** Behavior of the potential in a regime with a free outflow of electrons for the second type of tube bending. Plots are presented for various angles between the magnetic moment and the angular velocity of the star (the solid and dotted curves correspond to nondipolar and dipolar fields, respectively).

0, and the potential has the form

$$\Phi = \frac{\Omega F}{2\pi c}(1-\xi^2)[1-\kappa(a/r)^3]\cos\chi. \qquad (13)$$

At large distances from the star, the potential tends toward that for the corresponding dipolar tube. The difference is appreciable only near the stellar surface.

If there is no outflow of charged particles, a region of strong electric field is formed over the surface on a scale of the order of the tube diameter. The potential arising in this region in the case of a dipolar magnetic field is $\Omega F/2\pi c$ [5]. We shall assume that this same value remains appropriate for the nondipolar magnetic field. The potential above this region can be described by (13). At $r = a$, expression (13) gives the potential just over the region of strong field. The difference of a factor of $(1-\kappa)$ is due to the effect of

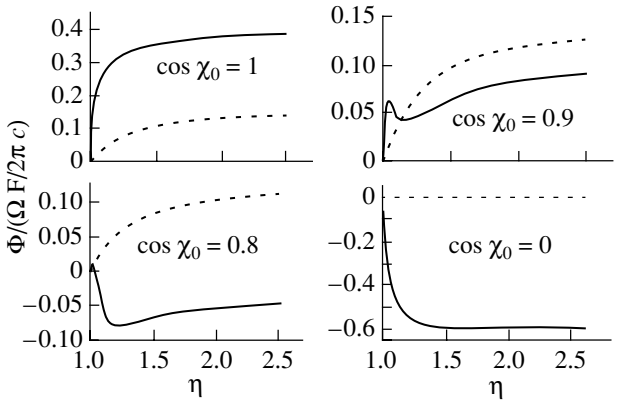


**Fig. 4.** Behavior of the potential in a regime with a free outflow of charged particles for the first type of tube bending. Plots are presented for various angles between the magnetic moment and the angular velocity of the star (the solid and dotted curves correspond to nondipolar and dipolar fields, respectively).

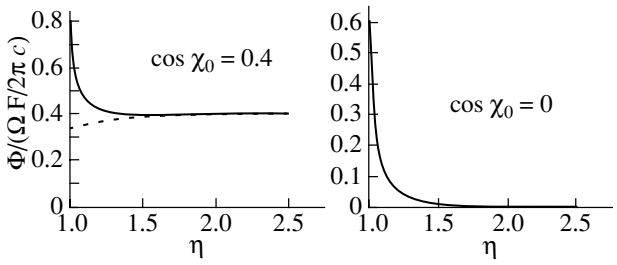


**Fig. 5.** Behavior of the potential for the first type of tube bending in the absence of a thermoemission current. Plots are presented for various angles between the magnetic moment and the angular velocity of the star (the solid and dotted curves correspond to nondipolar and dipolar fields, respectively).

inertial-frame dragging, which is taken into account in our treatment.

The behavior of the potential for the first type of tube bending is shown in Fig. 5. We can see that the effect of the bending does not contribute to the electrostatic potential at infinity. The maximum potential is observed over nearly the entire range of angles near the surface. (As before, the potential is zero at the stellar surface.) As the avalanche develops, the functional dependence of the potential should evolve toward a monotonic function due to the accumulation of negative charge in the region of the maximum. Therefore, the tube bending in fact does not affect the final electric field in this case.

Figure 6 shows the behavior of the potential for the second type of tube bending. The observed minima of the potential will gradually be filled with positive charge, reducing the potential to a monotonic function. Therefore, if there is no outflow of charge from

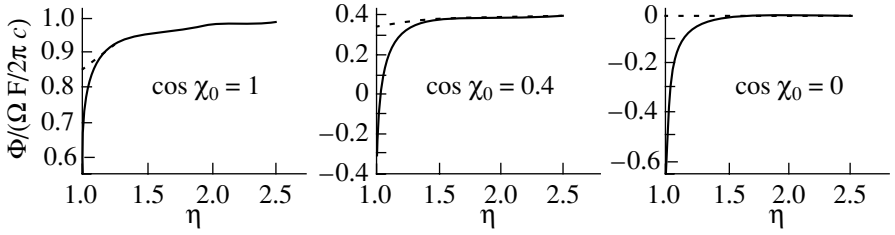


**Fig. 6.** Behavior of the potential for the second type of tube bending in the absence of a thermoemission current. Plots are presented for various angles between the magnetic moment and the angular velocity of the star (the solid and dotted curves correspond to nondipolar and dipolar fields, respectively).

the stellar surface, the behavior of the potential in a curved tube nearly coincides with the behavior in a dipolar tube.

In the general case of an arbitrary thermoelectron emission current, the potential can be written in the form

$$\Phi = \frac{\Omega F}{2\pi c}(1-\xi^2) \times \{[1-\kappa(a/r)^3]\cos\chi + \beta\cos\chi_{\rm surf}(\kappa-1)\}, \quad (14)$$

where $\beta$ is the ratio of the thermoemission current to the Goldreich–Julian current $\mathbf{j} = (\mathbf{B}/B)(\mathbf{\Omega B}/2\pi)$.

## 4. THERMOELECTRON EMISSION FROM THE NEUTRON-STAR SURFACE

We shall consider only pulsars whose polar regions emit electrons. The electric field accelerating the particles along the open magnetic-field lines depends on the boundary condition at the stellar surface. If the surface temperature is not sufficiently high, the thermoemission current is considerably lower than the limiting Goldreich–Julian current $\mathbf{j} = (\mathbf{B}/B)(\mathbf{\Omega B}/2\pi)$ and our solution will be similar to that of Ruderman and Sutherland [5]. On the other hand, when the temperature is high enough to give rise to a free outflow of electrons, the electric field at the surface will equal zero and we obtain the solution derived by Muslimov and Tsygan [1, 2] and Beskin [3]. The Ruderman–Sutherland potential is more efficient at accelerating the particles. Nevertheless, some seed electrons are needed in order for the avalanche to develop, and a sufficient number of positrons must return to the surface if the avalanche is to be supported. This is not always possible. Therefore, it is interesting to consider the case when the primary particles are supplied from the stellar surface by thermoemission. (For the Ruderman–Sutherland solution to be applicable, the thermocurrent must be fairly small, for example, 10% of the limiting current.) Such a regime is feasible only within a narrow temperature range. The relation between the thermoemission current and the surface temperature is given by the Richardson–Dushman formula [11]:

$$j = \frac{4\pi em}{(2\pi\hbar)^3}(kT)^2\exp(-b_0/kT). \quad (15)$$

Here, $m$ and $e$ are the electron mass and charge, $\hbar$ is Planck's constant, $T$ is the surface temperature, $k$ is Boltzmann's constant, and $b_0$ is the work required for an electron to leave the metal. This formula must be revised for the case of the strong magnetic field at the neutron-star surface.

We shall use a model with an ideal electron gas described by Fermi–Dirac statistics. The number of electrons per unit volume and per element of momentum space $d^3p$ is given by the expression

$$dn = \frac{2}{(2\pi\hbar)^3}\frac{1}{\exp\left(\dfrac{E-E_F}{kT}\right)+1}d^3p, \quad (16)$$

where $E$ is the electron energy and $E_F$ is the Fermi energy. We will call the work required to extract an electron from the Fermi level of the metal in the magnetic field the work function, $b(B)$. This work depends on the magnetic-field intensity. Only electrons with energies $E > E_F + b(B)$ can leave the metal. In order for the lattice to be stable, the number of such electrons must be small. This is satisfied when $b(B) \gg kT$. Using this inequality, we can rewrite (16) for electrons whose energy is sufficient to leave the metal:

$$dn = \frac{2}{(2\pi\hbar)^3}\exp\left(\frac{E_F}{kT}\right)\exp\left(-\frac{E}{kT}\right)d^3p. \quad (17)$$

The energy of an electron in a magnetic field $E$ is

$$E = \hbar\omega_c(\nu + 1/2 + \sigma) + \frac{p_z^2}{2m}. \quad (18)$$

Here, the $z$ axis is directed along the magnetic field; $\nu = 0,\ 1,\ \ldots$; $\sigma = 1/2$ describes the interaction of the electron spin with the magnetic field; and $\omega_c$ is the electron cyclotron frequency. Let us calculate the

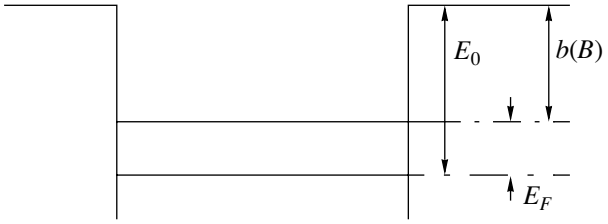


**Fig. 7.** The work function $b(B)$ is the work required to extract an electron from the Fermi level of the metal. The Fermi energy $E_F$ is measured from the minimum energy $E_0$ of an electron in the crystal.

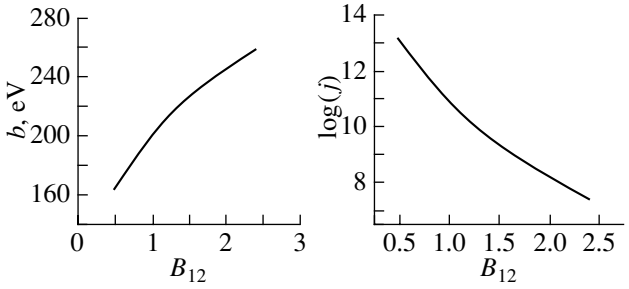


**Fig. 8.** Dependence of the electron work function and the thermoemission current on the magnetic field.

number of electrons $dn_z$ whose $z$ momentum is between $p_z$ and $p_z + dp_z$:

$$dn_z = \sum_\nu \sum_\sigma \frac{2}{h^3} \exp\left(\frac{E_F}{kT}\right) \times \exp\left(-\frac{p_z^2/2m + \hbar\omega_c(\nu + 1/2 + \sigma)}{kT}\right) dp_z 2\pi m\hbar\omega_c. \quad (19)$$

Here, $d^3p$ is presented in cylindrical coordinates and the integration in azimuth has been carried out:

$$d^2p = dp_z 2\pi p_\perp dp_\perp = dp_z 2\pi m dE_\perp = dp_z 2\pi m\hbar\omega_c. \quad (20)$$

If $\dfrac{\hbar\omega_c}{kT} \gg 1$ (for example, this ratio is about $10^3$ for a field of $10^{12}$ G and a temperature of $10^5$ K), only the term with $\nu = 0$ and $\sigma = -1/2$ contributes significantly to the sum. As follows from (19),

$$dn_z = \frac{4\pi m}{(2\pi\hbar)^3}\hbar\omega_c \exp\left(\frac{E_F - p_z^2/2m}{kT}\right) dp_z. \quad (21)$$

The current is calculated by integrating over all electrons for which $p_z > \sqrt{2m[E_F + b(B)]}$:

$$j = \frac{e}{m} \int_{\sqrt{2m[E_F+b(B)]}}^{\infty} p_z dn_z = \frac{4\pi me}{(2\pi\hbar)^3} kT\hbar\omega_c \exp\left[-\frac{b(B)}{kT}\right]. \quad (22)$$

Let us consider the dependence of the current (22) on the magnetic field. The factor in front of the exponent is proportional to the field. Let us determine the dependence of the work function on the field. As is noted above, the work function $b(B)$ is the work required to extract an electron from the Fermi level of the metal. The Fermi energy is measured from the minimum energy $E_0$ of an electron in the crystal; i.e., $b(B) = E_0 - E_F$, as is shown in Fig. 7.

The dependence of the Fermi energy on the magnetic field is well known (see, for example, [12]):

$$E_F = \frac{1}{2m}\left(\frac{2\pi^2\hbar^2 cn_e}{eB}\right)^2, \quad (23)$$

where $n_e$ is the electron density. The dependence of $E_0$ on the field can be estimated as follows. Let us first consider an ordinary crystal (not subject to a magnetic field). The crystal can be represented as a periodic sequence of potential wells (ions at the lattice sites). These wells have a characteristic width $d1$ (about 1 Å), and the characteristic distance between the lattice sites is $d2$. When $d2$ is large, we have free atoms, which are not bound by the lattice. The energy $E_0$ in this case is just the ionization energy of a free atom. As $d2$ decreases (i.e., the lattice becomes denser), $E_0$ also decreases. The characteristic ratio $d1/d2$ is equal to 0.5. The energy $E_0$ in a crystal decreases with respect to that for a free atom by approximately a factor of 1.5. For example, in the case of iron, $E_0$ for an atom is 5.15 eV, while $E_0$ in a crystal is 8.2 eV [13].

The characteristic sizes of atoms decrease substantially in magnetic fields typical of radio pulsars (of the order of $10^{12}$ G). For example, the hydrogen atom contracts by approximately a factor of 20 across the field and a factor of 4 along the field. Therefore, the lattice of atoms becomes denser. Assuming the ratio $d1/d2$ remains approximately the same, we conclude that the $E_0$ values in the crystal and for an atom differ by a factor of 1.5, as before. Therefore, the dependence of $E_0$ on $B$ is determined completely by the variation of the ionization energy of a free atom $E_{\rm ion}$ with the magnetic field. Although the stellar crust is composed of iron, we shall use the results derived for the hydrogen atom [14] to determine the ionization energy for the outer electrons:

$$E_{\rm ion}/{\rm Ryd} = \ln\{e + p_1[\ln(1 + p_2\sqrt{\gamma})]^2\} + p_3[\ln(1 + p_4\gamma^{p_5})]^2. \quad (24)$$

Here, Ryd = 13.6 eV, $\gamma = B/2.35 \times 10^9$ G, $p_1 = 15.55$, $p_2 = 0.378$, $p_3 = 2.727$, $p_4 = 0.3034$, and $p_5 =$

0.438. If the field intensity is $10^{12}$ G, the ionization energy will be 160 eV, i.e., the binding energy in the crystal will be 24 eV.

Let us determine the dependence of the Fermi energy on the magnetic field. First, we must find the electron density. This can be expressed in terms of the density of matter at the stellar surface:

$$n_e = \frac{2\rho_{\rm Fe}}{56 m_p}. \quad (25)$$

We have assumed in the formula above that only two outer electrons become common (free).

The matter density is inversely proportional to the size of the atoms, which is given by the following asymptotic formulas (we also use here the results derived for the hydrogen atom [14]):

$$l_x = l_y \approx a_B\sqrt{1/\gamma}, \quad (26)$$
$$l_z \approx (1/\sqrt{2} + 1/\ln\gamma)(\mathrm{Ryd}/E_{\rm ion})^{1/2} a_B,$$

where $l_x$ and $l_y$ are the dimensions across the magnetic field and $l_z$ is the dimension along the field. Therefore, the matter density will be

$$\rho_{\rm Fe} = \frac{a_{\rm B}^3}{l_x l_y l_z} 7.8\ \mathrm{g/cm^3}. \quad (27)$$

For example, a field of $10^{12}$ G should lead to a density of $1.3 \times 10^4$ g/cm$^3$ and a Fermi energy of 30 eV. We now have all the data required to determine the dependence of the electron work function (and, consequently, the thermoemission current) on the magnetic field. These dependences are presented in Fig. 8 (the current was calculated for a temperature of $0.55 \times 10^5$ K). Thus, the thermoemission current decreases with increasing $B$.

The surface temperature that produces a thermoemission current that is 1–10% of the Goldreich–Julian current for a rotational period of 1 s and a field intensity of $10^{12}$ G can be estimated to be $0.55 \times 10^5$ K (the corresponding work function is 210 eV).

## 5. GENERATION OF ELECTRON–POSITRON PAIRS IN THE REGION OF CLOSED FIELD LINES

The model of a radio-pulsar magnetosphere considered above inevitably results in the generation of electron–positron pairs by gamma-rays beyond the magnetic tubes. Such pairs born in the region of closed field lines will travel through the entire magnetosphere and arrive at the opposite magnetic pole, heating a spot near the opposite pole. The characteristic size of this hot spot should be comparable to the size of a magnetic tube. Therefore, the poles will heat each other. The beams of electron–positron plasma should penetrate the stationary plasma of the Goldreich–Julian magnetosphere. In our case, this plasma is composed of electrons and is characterized by $\rho_{\rm eff}$. Finally, plasma oscillations will be excited both in the moving electron–positron plasma and in the stationary plasma, resulting in the generation of radio emission. This radiation should consist of the following components: a narrow directed beam and an isotropic component. The isotropic radio emission will have a lower characteristic frequency.

## 6. CONCLUSIONS

(1) We have calculated the electrostatic potential in a thin tube of nondipolar magnetic field. The accelerating potential can be increased by a factor of a few due to the curvature of the magnetic-field lines. We have calculated the behavior of the potential for a particular configuration of the magnetic field.

(2) We have estimated the magnetic-field dependence of the electron work function and the thermoelectron emission current from the surface layer of a neutron star.

(3) A mutual heating of the polar regions of radio pulsars is possible in the case of a nondipolar magnetic field. As a result, both directed and isotropic radio emission can be generated in the region of closed magnetic-field lines.

The results obtained should enable us in the future to derive new "switch-off lines" for radio pulsars that are shifted toward longer periods, yielding a better agreement with observations.

## ACKNOWLEDGMENTS

This work was supported by the Russian Foundation for Basic Research (project code 01-02-17811) and the State Science and Technology Program "Astronomy."

## REFERENCES

1. A. G. Muslimov and A. I. Tsygan, Astron. Zh. **67**, 263 (1990) [Sov. Astron. **34**, 133 (1990)].
2. A. G. Muslimov and A. I. Tsygan, Mon. Not. R. Astron. Soc. **255**, 61 (1992).
3. V. S. Beskin, Pis'ma Astron. Zh. **16**, 665 (1990) [Sov. Astron. Lett. **16**, 286 (1990)].
4. A. I. Tsygan, in *Pulsar Astronomy—2000 and Beyond,* ASP Conf. Ser. **202**, Ed. by M. Kramer, N. Wex, and R. Wielebinski (San Francisco, Astronomical Society of the Pacific, 2000), p 473.
5. M. A. Ruderman and P. G. Sutherland, Astrophys. J. **196**, 51 (1975).
6. V. D. Pal'shin and A. I. Tsygan, Preprint No. 1718, Ioffe Physicotechnical Institute (1998).

7. A. G. Muslimov and A. I. Tsygan, Mon. Not. R. Astron. Soc. **255**, 61 (1992).
8. Bing Zhang, A. K. Harding, and A. G. Muslimov, Astrophys. J. **531**, L135 (2000).
9. A. I. Tsygan, in *Pulsar Astronomy—2000 and Beyond,* ASP Conf. Ser. **202**, Ed. by M. Kramer, N. Wex, and R. Wielebinski (San Francisco, Astronomical Society of the Pacific, 2000), p. 473.
10. J. Arons and E. T. Scharlemann, Astrophys. J. **231**, 854 (1979).
11. D. V. Sivuchin, *General Physics*, Vol. 3: *Electricity* [in Russian] (Moscow, 1977).
12. D. G. Yakovlev and A. D. Kaminker, *IAU Colloquium 147: The Equation of State in Astrophysics,* Ed. by G. Chabrier and E. Schatzman (Cambridge University Press, Cambridge, 1994), p. 214.
13. C. Kittel, *Introduction to Solid State Physics* (Wiley, New York, 1953).
14. A. Y. Potekhin, J. Phys. B: At. Mol. Opt. Phys. **31**, 49 (1998).

*Translated by Yu. Dumin*